UNIVERSITAT POLITÈCNICA DE VALÈNCIA

Department of Electronic Engineering
Doctoral Program in Technologies for Health and Well-Being

Computer modeling and experimentation in radiofrequency-based minimally invasive therapies

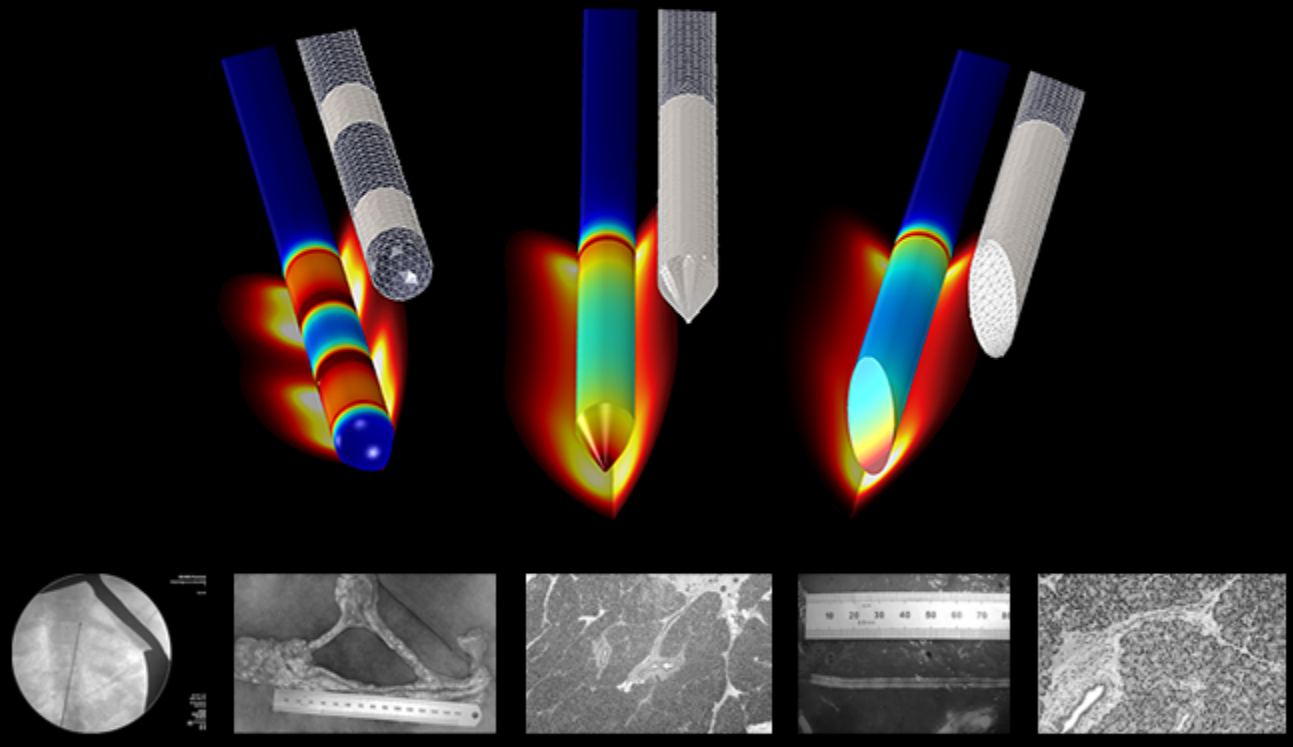

Doctoral Dissertation of:
Elżbieta Ewertowska

Supervisors:
Dr. Enrique Berjano Zanón
Dra. Macarena Trujillo Guillén

November 2019, Valencia

UNIVERSITAT POLITÈCNICA DE VALÈNCIA

Department of Electronic Engineering

Doctoral Program in Technologies for Health and Well-Being

Computer modeling and experimentation in radiofrequency-based minimally invasive therapies

---

Doctoral Dissertation of:

Elżbieta Ewertowska

Supervisors:

Dr. Enrique Berjano Zanón

Dra. Macarena Trujillo Guillén

November 2019, Valencia

He that would enjoy life and act with freedom must have the work of the day continually before his eyes. Not yesterday's work, lest he fall into despair; nor to-morrow's, lest he become a visionary—not that which ends with the day, which is a worldly work; nor yet that only which remains to eternity, for by it he cannot shape his actions.

Happy is the man who can recognize in the work of to-day a connected portion of the work of life and an embodiment of the work of Eternity. The foundations of his confidence are unchangeable, for he has been made a partaker of Infinity. He strenuously works out his daily enterprises because the present is given him for a possession.

Thus ought Man to be an impersonation of the divine process of nature, and to show forth the union of the infinite with the finite, not slighting his temporal existence, remembering that in it only is individual action possible; nor yet shutting out from his view that which is eternal, knowing that Time is a mystery which man cannot endure to contemplate until eternal Truth enlighten it.

– James Clerk Maxwell –

For my family and friends

who have given me constant love and support

Acknowledgements

First of all, I would like to express my sincere gratitude to the supervisors from the Universitat Politècnica de València, Dr. Macarena Trujillo Guillén and Dr. Enrique Berjano Zanón, for their patient guidance, unceasing encouragement and constructive suggestions during the development of this research work. I very much appreciate the dedication and time they have taken, despite of their hectic schedules, to provide me valuable feedback, help handle critical situations and keep my research on the right course while giving me the level of freedom and independence that I needed.

I would also like to acknowledge Dr. Fernando Burdío from Hospital del Mar, Dr. Ana Andaluz from Universitat Autónoma de Barcelona, and their team for their huge contribution to experimental animal studies and clinical trials, without which this work could not have been accomplished.

The completion of this work would have not been possible without the financial support of the Spanish Ministerio de Economía, Industría y Competitividad that provided funding for the development of this research project, my Predoctoral scholarship, and also Travel Grant for the research stay in The Wellman Center for Photomedicine.

I am also extremely thankful to Dr. Antoni Ivorra from Universitat Pompeu Fabra and Dr. Walfre Franco from The Wellman Center for Photomedicine at Massachusetts General Hospital for providing me their time, mentorship and opportunity to work under their direction during each research stay at their centers. Exposure into different international research environments has been a hugely valuable and eye-opening experience for me.

This acknowledgement would be incomplete without mentioning my great family of ten who has supported me throughout these years was there to remind me of the beauty in the everyday course of life. Thank you for being people of faith and the testimony of God's amazing love and grace.

I am especially grateful for all those wonderful people that I have had the privilege to befriend. Their moral support, joy and care were a constant source of inspiration and motivation.

Finally, above all, I am thankful to my Almighty God who deserves all glory, honor and power, and who keeps surprising me with His continuous blessings.

Abstract

Radiofrequency (RF) ablation has become an important ablative technique widely used in the area of minimally invasive therapies of the modern medicine. The advancement in the field of RF-based technologies over the years has led to a growing number of applications in different therapeutic areas such as cardiac arrhythmias, epilepsy, oncology, assisted resection, apnea, pain or aesthetic surgery. There is, however, a constant need for the development of computer and experimental studies, which would enhance the performance and safety of these techniques.

The main focus of this PhD Thesis was on examining the thermal and electrical phenomena behind tissue radiofrequency ablation in order to improve the efficacy and safety of the RF-based therapies and applicators. Two main areas of interest were pain management and oncology, which were organized into three independent studies. The research methodology was based on computer modeling and experimental studies on phantoms, *ex vivo* and *in vivo* models, and clinical trials.

The research on pain management involved the analysis of electrical and thermal effects of the pulsed radiofrequency (PRF) treatment and the related risk of tissue thermal damage. Different pulse protocols used in clinical practice were studied using computer modeling and the study accuracy was validated by means of agar phantom model. Additional computer models for alternative pulse protocols were also proposed, in which thermal effect would be reduced but the electrical effect would remain unchanged. The study also discussed the concept of a mild electroporation from PRF.

In the area of oncology, two different techniques were analyzed. First study focused on examining tissue hydration technique during RF ablation with a novel internally cooled wet (ICW) electrode. The new design involved two expandable perfusion needles built into the catheter. The main aim was to

improve the accuracy of computer model of tumor RF ablation using a realistic geometry of saline distribution in tissue, and to assess the performance of the RF catheter. Different cases of saline-infused tumor were modeled and the simulated results were compared with the clinical data from a trial on 17 hepatic cancer patients. An *in vivo* study on pig liver model was used to obtain a realistic spatial distribution of the infused saline.

The second study focused on the development of a new catheter-based endoluminal sealing technique as more effective alternative for management of the pancreatic stump. The method consisted of the impedance-guided radiofrequency ablation with pullback. Fine-tuning involving RF catheter type and ablation protocol was performed using *ex vivo* porcine models, and posteriorly, sealing effectiveness was assessed on an *in vivo* pig model.

Resumen

La ablación por radiofrecuencia (RF) se ha convertido en una técnica ablativa importante, ampliamente utilizada en el área de las terapias mínimamente invasivas de la medicina moderna. El avance en el campo de las tecnologías basadas en RF a lo largo de los años ha llevado a un número creciente de aplicaciones en diferentes áreas terapéuticas tales como arritmias cardíacas, epilepsia, oncología, resección asistida, apnea, dolor o cirugía estética. Sin embargo, existe una constante necesidad de desarrollar estudios computacionales y experimentales para mejorar el rendimiento de estas técnicas.

El enfoque principal de esta tesis doctoral está centrado en examinar los efectos térmicos y eléctricos de ablación por radiofrecuencia de tejidos para mejorar la eficacia y la seguridad de las terapias y dispositivos basados en energía de radiofrecuencia. Las dos áreas principales de interés han sido el tratamiento del dolor y la cirugía hepática oncológica, que se han organizado en tres estudios independientes. La metodología de los estudios se ha basado en modelos computacionales y estudios experimentales sobre phantom de agar, modelos *ex vivo* e *in vivo* y ensayos clínicos.

El estudio focalizado en el tratamiento del dolor ha incluido el análisis de los efectos eléctricos y térmicos del tratamiento con radiofrecuencia pulsada (PRF) y el riesgo relacionado con el daño térmico al tejido. Se han estudiado diferentes protocolos pulsados empleados en la práctica clínica utilizando modelos computacionales. La exactitud del modelo se ha validado mediante un modelo en phantom de agar. Se han propuesto también modelos computacionales adicionales para los protocolos pulsados alternativos en los cuales se reduciría el efecto térmico sin afectar al efecto eléctrico. En el estudio se ha discutido también el concepto de electroporación leve como el resultado de PRF.

En el área de la cirugía hepática oncológica se han analizado dos técnicas diferentes. El primer estudio se ha centrado en examinar la hidratación del tejido durante la ablación por RF con un nuevo electrodo ICW. El nuevo diseño ha incluido dos agujas de perfusión expandibles integradas en el catéter. El objetivo principal ha sido mejorar la precisión del modelo computacional de ablación por RF de tumor utilizando una geometría realista de la distribución de solución salina en el tejido y evaluar el rendimiento del catéter de RF. Se han modelado diferentes casos de tumor infundido con solución salina y los resultados simulados se han comparado con los datos clínicos de un ensayo en 17 pacientes con cáncer hepático. Con el fin de obtener una distribución espacial realista de la solución salina infundida, se ha empleado un estudio *in vivo* sobre el modelo de hígado de cerdo.

El segundo estudio se ha centrado en el desarrollo de una nueva técnica de sellado endoluminal basada en catéter, como una alternativa más efectiva para el manejo del remanente pancreático. El método ha consistido en una ablación por radiofrecuencia guiada por impedancia con la técnica de pullback. El ajuste del tipo de catéter de RF y del protocolo de ablación se ha realizado mediante modelos porcinos *ex vivo*. Posteriormente, la efectividad del sellado se ha evaluado sobre un modelo de cerdo *in vivo*.

Resum

L'ablació per radiofreqüència (RF) s'ha convertit en una tècnica ablativa important, àmpliament utilitzada en l'àrea de les teràpies mínimament invasives de la medicina moderna. L'avanç en el camp de les tecnologies basades en RF al llarg dels anys ha portat a un número creixent d'aplicacions en diferents àrees terapèutiques com ara arítmies cardíaques, epilèpsia, oncologia, resecció assistida, apnea, dolor o cirurgia estètica. No obstant això, hi ha una constant necessitat de desenvolupar estudis computacionals i experimentals per a millorar el rendiment d'aquestes tècniques.

Aquesta tesi doctoral ha estat centrada en examinar els efectes tèrmics i elèctrics de l'ablació per radiofreqüència de teixits per tal de millorar l'eficàcia i la seguretat de les teràpies i dispositius basats en energia de radiofreqüència. Dos àrees principals són el tractament del dolor i la cirurgia hepàtica. Aquestos han sigut organitzats en tres estudis independents. La metodologia dels estudis ha estat basada en models computacionals i experimentals sobre phantom d'agar, models *ex vivo* i *in vivo* i assajos clínics.

L'estudi enfocat en el tractament del dolor ha inclòs l'anàlisi dels efectes elèctrics i tèrmics del tractament amb radiofreqüència polsada (PRF) i el risc relacionat amb el dany tèrmic al teixit. S'han estudiat diferents protocols polsats emprats en la pràctica clínica utilitzant models computacionals. L'exactitud del model ha estat validada per mitjà d'un model de phantom d'agar. S'han proposat també models computacionals addicionals per a protocols polsats alternatius en els quals es reduiria l'efecte tèrmic sense afectar l'efecte elèctric. En aquest estudi s'ha discutit també el concepte d'electroporació lleu com el resultat de PRF.

A l'àrea de la cirugía hepàtica han sigut analitzades dos tècniques diferents. El primer estudi s'ha centrat en la hidratació del teixit durant l'ablació per RF amb un nou elèctrode ICW. El nou disseny ha inclòs dos

agulles de perfusió expandibles integrades en el catèter. L' objetiu principal ha sigut millorar la precisió del model computacional d' ablació de tumors per RF utilitzant una geometria realista per a la distribució de sèrum salií en el teixit i evaluar el rendiment del catèter de RF. S'han modelat diferents casos de tumor infundit amb sèrum salí i els resultats simulats han sigut comparats amb les dades clíniques d'un assaig dut a terme sobre 17 pacients amb càncer hepàtic. Amb l'objetiu d'obtenir una distribució espacial realista del sèrum salí injectat, s'ha du a terme un estudi *in vivo* basat en un model de fetge de porc.

El segon estudi s'ha centrat en el desenvolupament d'una nova tècnica de tancament endoluminal bassat en catèter, com una alternativa més efectiva per a gestionar el romanent pancreàtic. El mètode ha consistit en una ablació per radiofreqüència guiada per impedància amb la tècnica de *pullback*. L'ajust del tipus de catèter de RF i del protocol d'ablació ha sigut realitzat per mitjà de models porcins *ex vivo*. Posteriorment, l'efectivitat del tancament ha sigut avaluada sobre un model de porc *in vivo*.

Preface

This work is a part of my journey through the world of Biomedical Engineering that started ten years ago in my home country and brought me to Spain in pursuit of new experiences, international expertise and carrier development. This new chapter in my life not only allowed me to acquire the desired knowledge, but also surprised me with great challenges, unexpected opportunities, dear friendships and inspirational role models to follow. It has also given me a chance to assist international conferences and collaborate with various international research institutes, which resulted in an enriching and extraordinary learning and networking experience.

Regarding biomedical research area, it has always been my desire to work in the field of engineering applied in medicine with a particular focus on the research and development of biomedical devices. This has motivated my master studies with specialization in Bioelectronics and Biomedical Instrumentation and given the opportunity to carry on with PhD degree. My PhD research has been influenced by different collaboration opportunities, from which have emerged topics that I have studied throughout the progress of the doctoral program. As a result, they might be mistakenly perceived as unrelated works. Nonetheless, the main motivation behind this dissertation was to contribute to research on radiofrequency ablation (RFA) applied in minimally invasive procedures in order to deepen the understanding of its mechanisms and capacities and improve the performance as therapeutic technique. The general objectives of this work can be defined as: (1) development of computer models to study electrical and thermal effects of RFA for tissue selective destruction applied in tumor focal ablation and surgical resection; and (2) *ex vivo* and *in vivo* experimental validation of computer models for RFA.

Three different studies were developed within the scope of the general objectives that contributed to accomplishment of the main aim of the present dissertation. These involved the study on: (1) the electrical and thermal effects of different pulsed radiofrequency protocols on computer and phantom models; (2) the internally cooled wet radiofrequency electrode performance and tissue hydration on hepatic tissue *ex vivo* and computer models; and (3) the development of catheter-based endoluminal radiofrequency sealing technique.

Structure of the document

This document is arranged into six main chapters. *Chapter 1* is an introduction that integrates the overview of the ablative techniques used in minimally invasive therapies, general principles and applications of RFA, along with its research methodology. *Chapters 2, 3* and *4* contain the three research studies conducted, and which has already been published as separate original articles in *The International Journal of Hyperthermia*, which is the official journal of the Society for Thermal Medicine (N. America), the European Society for Hyperthermic Oncology, and the Japanese Society for Thermal Medicine.

General discussion on the overall results of this work and final conclusions are included in *Chapter 5* and *6*, respectively. Lastly, the last two sections mention all the publications and participation in scientific meetings and conference throughout the duration of my PhD program.

Financial support

My entire PhD training period has been supported by the Spanish Ministerio de Economía, Industría y Competitividad through a Predoctoral scholarship (BES-2015-073285). Moreover, the three developed studies were supported by the Spanish Government, in particular by the Spanish Ministerio de Economía, Industria y Competitividad under “Plan Estatal de Investigación, Desarrollo e Innovación Orientada a los Retos de la Sociedad”

(Grant TEC2014–52383–C3–R) and by the Spanish Ministerio de Ciencia, Innovación y Universidades under “Programa Estatal de I+D+i Orientada a los Retos de la Sociedad" (Grant: RTI2018-094357-B-C21 and –C22). I have been also the recipient of the ASLMS Educational Grant provided by the American Society for Laser Medicine and Surgery, Inc. to support attendance at the 39th ASLMS Annual Conference on Energy-based Medicine & Science held in 2019 in Denver.

Declaration of interest

I declare that I have no conflict of interest or financial ties to disclose for any of the content in the context of this PhD thesis.

Table of contents

List of Tables

List of Figures

Chapter 1
Introduction

This chapter presents an overview of techniques, concepts and principles that are involved in the field of radiofrequency-based minimally invasive therapies, and which were used for the accomplishment of this work. Thus, the following paragraphs include a general outline of the different energy sources and applications in the context of high-temperature ablative techniques along with specific applications and therapies that employ techniques based on radiofrequency (RF) ablation (RFA). Next, a description of RFA physical principles and RF applicators is included. The last section of this chapter describes different methodologies of research utilized in this work, such as computer and experimental modeling, and highlights the key objectives and contributions to the current state of knowledge.

1.1. High-temperature ablative techniques

Over the past few decades medicine has been transformed by a rapid growth of technological advancement. This included also the area of surgical techniques, which was boosted by the modern era pursuit of quality improvement in healthcare. The development of imaging techniques for interventional procedures was fundamental for evolution of image-guided minimally invasive surgery, in particular thermal ablation that has become a vital field of operative medicine.

The term thermal ablation refers to abnormal tissue destruction or removal using elevated or depressed tissue temperatures, which is achieved by using different energy sources such as high intensity focused ultrasound (HIFU), radiofrequency (RF), microwaves, laser energy or cryoablation. These techniques have been evolved and employed in the treatment of local

malignancies as alternatives to open surgery. As minimally invasive strategies, they aim primarily at enhancing patient outcome and system performance in terms of time and cost-effectiveness. They also offer the advantage of treating patients who are not candidates for conventional therapy. These facts have led to the development of effective therapies with demonstrated reduction of pain and surgical trauma and faster patient recovery compared to traditional, open surgery. Subsequently, the reported clinical trials involve hepatic and brain cancer, renal, breast and lung tumors and bony lesions treatments [1-16]. However, there is no clear evidence of the superior effectiveness of these techniques over traditional surgery due to the existing tumor recurrence rate, and often they are proposed in combination with other therapies such as e.g. chemotherapy or radiotherapy [17,18]. This condition, however, challenges research to make progress towards developing new designs in RF techniques and devices that would improve their performance.

The convenience of choosing one or another ablation technique depends on the specificity of the case and patient. In general, thermal ablation typically involve image-guided percutaneous placement of the applicator (i.e. catheter, needle) in order to ensure local energy delivery. Another but more invasive procedure used in minimally invasive surgery is laparoscopic approach. For ablative therapies with heat, the energy deposited in the surrounding tissue is adapted to produce tissue coagulative necrosis. The extent of the lesion will depend on the thermal dose administered, which translates as the final product of high temperature and exposure time, and on local tissue interactions that may result in heat lost [19,20].

Within the area of ablative techniques, RF ablation has proven to be a reliable method for creating thermally induced coagulative necrosis and being so, it has been frequently used in clinical practice for multiple medical applications [21].

1.2. Radiofrequency ablation for minimally invasive surgery

The earliest use of RF energy in surgery dates back to the early 20th century when it was employed for electrocautery and then subsequently applied for treatment of cardiac arrhythmias and desiccation of liver tumors [22-24]. It was in the early 1900s when the first RF generator was produced, which launched the subsequent use of RF energy in medicine. Since then, therapeutic applications of RF ablation has been proposed for the treatment of cardiac arrhythmias and epilepsy, through hepatic malignancies and neoplasms of the kidneys, breast, bone and lungs to assisted resection, apnea, pain and aesthetic surgery [3,11,13,15,23,25-27].

1.2.1. *Cancer treatment*

Despite a broad field of use, the main interest for RF ablation remains cancer treatment presumably due to a reputation for predictable ablation size and volume, short ablation time, relatively low complication and morbidity rates and suitability to be used on nonsurgical patients [19]. In clinical practice, the RF therapy usually consist of a direct and complete tumor ablation with a 0.5-1 cm, tumor free surgical margin in order to avoid cancerous cell seeding induced by RF catheter displacement or microscopic tumor in the surroundings of the primary tumor due to an incomplete of the tumor volume [28]. Ideally, a single RF ablation should provide a satisfactory ablation volume to accomplish the treatment. In reality, it has been observed that tumor sizes greater than 2 cm can be hardly treated with unique RF energy application [29]. As a result, in many cases overlapping ablations had to be performed. Another issue related with RF-based cancer treatment is associated with tumor location and local tissue properties that may affect the final outcome by poor accessibility or additional heat losses during ablation (e.g. blood flow cooling effect).

One of the most common cancer types in the world with low survival rate and high prevalence of metastasis is hepatocellular carcinoma (HCC). Short life expectancy is mainly due to the fact that only 10-20% are candidates for surgical resection or transplantation and hence the necessity of local

treatments such as RFA [28]. Although its efficacy has been seen on small-size tumors (<3 cm), the recurrence rate is highly dependent on tumor size and therefore for tumors over 5 cm in diameter the successful treatment constitutes only 25% of all cases [30]. All those concerns related with cancer treatment have produced a growing number of RF catheter designs, method improvement or combined therapies (see Section *1.4 Techniques and devices for radiofrequency ablation*) in aim to increase ablation volumes and enhance RF-based cancer treatment performance [31].

1.2.2. *Vascular and ductal sealing*

Radiofrequency ablation is also widely used as hemostatic technique for vascular occlusion, as well as endoscopic radiofrequency ablation for the treatment of varicose veins or malignant bile duct obstruction treatment, usually followed by stent placement (Figure 1a) [32,33]. Endoscopic approach requires RF catheters with suitable diameter, flexibility and ability to control the temperature necessary for its satisfactory management inside the duct and desired ablation volume formation. These parameters as well as any complications derived from RF sealing vary depending on the application.

Venous occlusion has so far shown a high treatment efficacy including the long-term studies and is considered a valuable alternative for open surgery. Major adverse events concerning vascular surgery involve thrombosis, nerve damage and skin burns [34]. Regarding bile duct occlusion, most complications can be a result of excessive thermal damage of the surrounding structures and cause leaks, hemorrhage or inflammatory responses [35]. Also, the risk of tissue adhesion to the electrodes should be considered as it may result in tissue disruption while withdrawing the catheter. The bipolar RF catheter is a recommended device to use in order to provide uniform and more controlled tissue coagulation in a zone surrounding the electrode [36].

1.2.3. *Pain treatment*

A relatively new technique that employs radiofrequency energy is pulsed radiofrequency (PRF) whose effectiveness has been reported in studies for

chronic cervical and lumbar radicular pain [37-39]. It is considered a non-destructive, safe method with reduced side effects in comparison to conventional radiofrequency (CRF). Despite of this, some studies demonstrated possible risk of heat bursts in a range of 60ºC, which means it surpasses the commonly accepted 45-50ºC-lethal temperature [40].

Although the mechanism of action for pain relief is debatable, it is believed that electric fields produced by high-voltage bursts of PRF alter the pain signals transmission and possibly also cause electroporation [41]. First proposed by Sluijter in 1998, PRF is currently employed typically using the standard protocol of a train of 20 ms-long pulses controlled by a temperature control unit that limits the maximum tissue temperature up to 42ºC [42,43]. Therefore, the total PRF duration is usually longer than of CRF and takes ~120 s. Energy deposition depends on the electromagnetic field distributed around the PRF cannula, which is stronger at the tip of the applicator, hence the importance of cannula adequate placement to maximize the electrical effect on nerve (Figure 1b) [40].

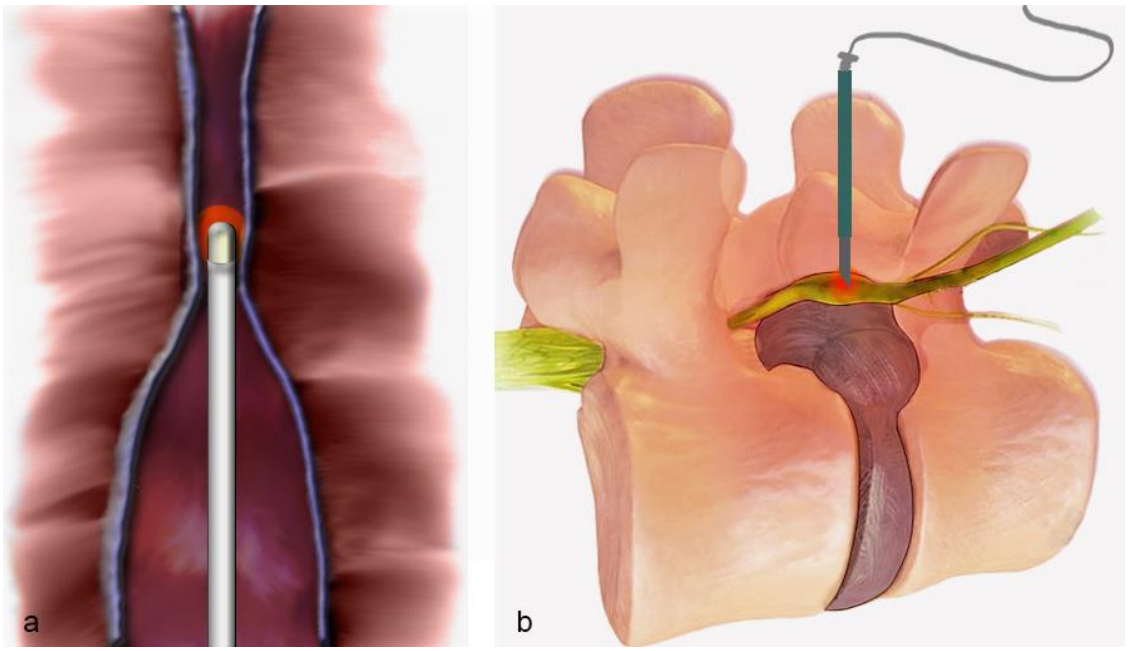

Figure 1. (a) RF catheter for endoscopic treatment of varicose veins, (b) pulsed radiofrequency treatment for pain management.

1.3. Physics of radiofrequency ablation

RF energy is a non-ionizing electromagnetic radiation comprised of electric and magnetic energy waves oscillating in the frequency range between 3 kHz and 300 GHz. For RF ablation of biological tissue, a high-frequency alternating current at ~500 kHz is used, as it is sufficient to produce frictional heating without neuromuscular stimulation and avoid excessive radiation. During RF ablation, the catheter is typically inserted interstitially and the active electrode in monopolar mode (or both electrodes in bipolar mode) is placed in direct contact with ablated tissue. RF current flows through electrically conductive tissue between electrodes (or electrode and grounding pad attached to the body surface). Energy delivery can be regulated either by current (I), voltage (V) or power (P) mode control since they are directly related through Ohm's law, $V=I \cdot Z$, Z being impedance of tissue in the path of current flow (i.e. between electrodes). It is important to note that these electrical variables correspond with RMS (root-mean-square) values of the waveform employed (sinus). Thus, RF performance strongly depends on the properties of the ablated tissue and the surrounding organs, the electrical conductivity being the most relevant for RF ablation.

The electrical properties of tissue vary for different organs and are also affected by water and fat content. Tissue hydration is associated with much higher electrical conductivity while fat, or adipose tissue, acts as thermal and electrical insulator. Among the relatively conductive tissues are the hepatic tissues (e.g. liver, kidney, pancreas) whereas less hydrated skin, lungs, breast or bones pose more challenge for RF ablation. Additionally, during ablation, water evaporation at temperatures near 100°C causes rapid tissue dehydration and loss of electrical conductivity when reached this point.

The mechanism of tissue heating by RF ablation is initially due to Joule heating from the resistive energy loss associated with ionic agitation. Joule heating covers only a short distance from the electrode. Deeper tissue layers are then heated due to thermal conduction, the process that is slower than resistive heating. Final volume of coagulation zone is obtained when the electrode-tissue system reaches energetic steady state. However, when

energy delivery is interrupted before reaching this state, the temperature of previously heated tissue continues increasing for several more degrees, and a subsequent lesion growth occurs [44]. This phenomenon is called “thermal latency”.

Tissue coagulative necrosis is based on irreversible cellular damage by temperatures typically ranging between 60 and 100ºC, although the breakpoint temperature is considered 43ºC [20]. The process can be defined by an exponential function according to Arrhenius plot, and different exposure times are required for each temperature degree in order to provoke irreversible thermal damage. This time-temperature relationship, referred to as “thermal dose”, is defined by temperature, exposure time, and tissue type, and serves to establish temperature thresholds for thermal damage. Tissue coagulation is associated with dehydration at temperatures around 100ºC and further charring. It also means that tissue electrical impedance increases rapidly, current flow is restrained and thermal lesion growth is impeded. This is the main limitation of RF ablation, and to overcome this problem has been the main reason for the development of new techniques and applicators. In addition to that, another common limitation that decreases RFA efficacy is heat sink effect corresponding to energetic loss from the cooling effect of the nearby blood vessels.

1.4. Techniques and devices for radiofrequency ablation

To this date, many RF devices has been studied and developed based upon the principles, limitations and applications of RF energy deposition, as none of them have proven superior to others. Along with the expansion of RF ablation-based treatments into new areas of application followed the development of electrode design. There is a distinction between the basic plain metal electrodes, internally cooled, expandable, wet or bipolar electrodes (Figure 2). Thus, in the context of the electrode, RF device can consist of one, multitined or multiple electrodes combined into a cluster of two (dual), three (triple), four (quadruple) or more electrodes. Multitined electrodes are designed as one expandable electrode inside an insulated

needle from which active tines are deployed once the needle is inserted into the target tissue.

Independently of the number of electrodes the setup can involve working in monopolar or bipolar mode [45]. In the first case, current flows from one or more electrodes of the same polarity toward a grounding pad (also known as dispersive electrode or reference patch). Bipolar mode involves two parallel inserted electrodes or electrode groups, which avoids the need for grounding pads related with the risk of burns. Both systems are currently used in different arrangements for multiple purposes depending on the desired shape and size of the final ablation volume.

Apart from varying the electrode shape and number in order to increase coagulation zone size, internal cooling (also called closed irrigation) inside the RF electrode has been proposed as a method to reduce tissue overheating around the electrode [46]. The cooling perfusate, typically saline, circulates inside the electrode tip through two hollow lumens, one for introducing cooling perfusate and other for the removal of the warmed liquid outside the applicator. It can be used in both monopolar and bipolar modes. The design has demonstrated a limited improvement in ablation lesion size [46].

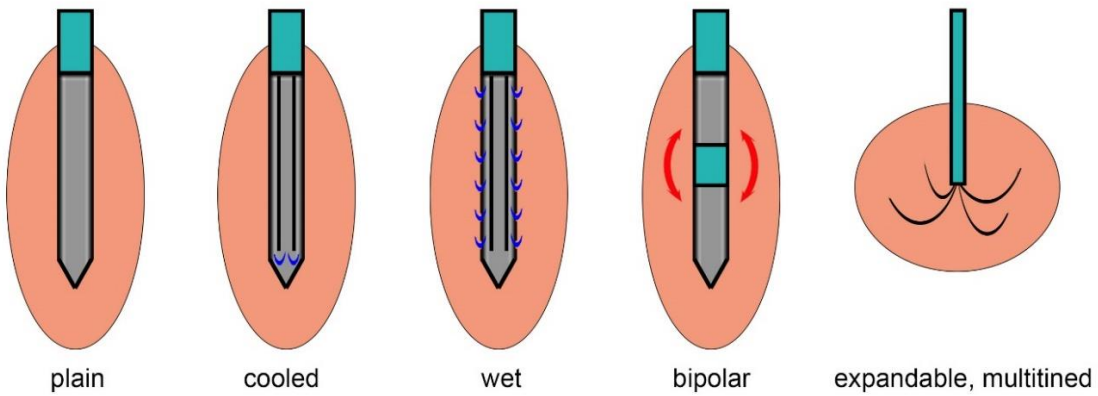

Figure 2. Basic designs of RF electrodes: plain, cooled, wet, bipolar, and expandable-multitined (adapted from [36]). Green zone corresponds with the plastic cover (electrical isolation), brown zone represents the created coagulation zone and blue lines correspond with the perfusate for open or closed-irrigation.

Another approach has taken advantage of saline-enhanced electrical tissue properties for greater current flow that would result in a greater ablation size. For this purpose, a wet electrode (also called open-irrigated electrode) has been proposed by Livraghi et al [47]. The catheter has tiny pores located at the electrode that administer saline to the tissue during ablation. The technique has also shown an enlarged coagulation zone size with respect to the conventional electrode, however, lesion contour is mainly irregular since there is no mechanism to control saline distribution in tissue. One proposal that addressed this limitation was a hybrid expendable-wet electrode that allows increasing ablation size and a roughly spherical shape to be obtained [48].

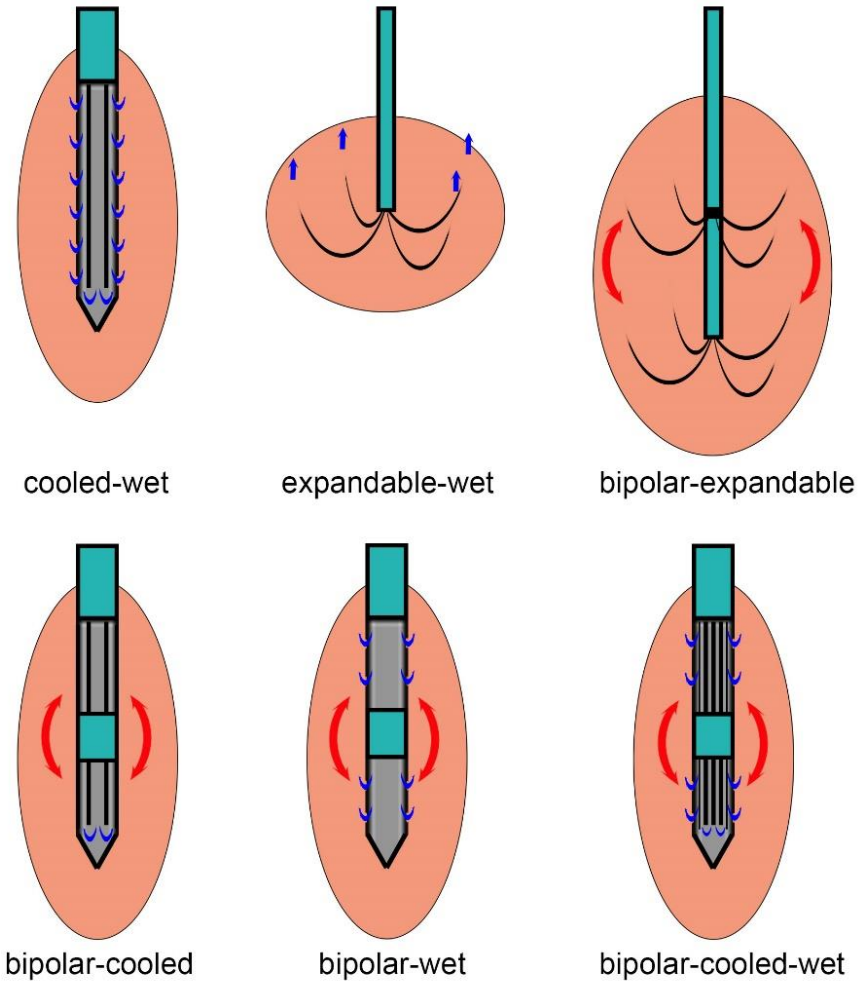

Figure 3. Hybrid RF electrodes: cooled-wet, expandable-wet, bipolar-expandable (upper row from the left) and bipolar-cooled, bipolar-wet, bipolar-cooled-wet (bottom row from the left).

Another study proposed a model for distance saline infusion that aimed at finding the most optimal perfusion distance for the greatest coagulation zone volume [49]. Since then, there have been also developed hybrid electrodes e.g. cooled-wet electrodes and others that would combine and potentiate the effects of both separate applicators (Figure 3) [45,50-52].

1.5. Research methodology and theory

Two main research approaches are being employed in parallel with the same aim of studying and optimizing a large number of techniques related to thermal ablation therapies including numerous RFA methods: computer modeling and experiments. Both are necessary for further advancement in the field of minimally invasive therapies. These methods offer different level of accuracy, viability and complexity as well as time- and cost-effectiveness, and therefore they have become complementary techniques employed in medical research and industry.

1.5.1. *Computer modeling*

Theoretical models have shown the capacity to predict in great detail empirical data that otherwise could be obtained in limited sample size. They are useful tools for optimization, maximization of therapy performance or personalized treatment using patient-specific parameters. The level of model complexity depends on the study requirements and feasibility of simplifying the processes, not affecting the results, in order to reduce computational cost. Model simplification is also necessary for parameters non-existing in literature, poorly described or presenting high variability such as e.g. tissue porosity. These uncertainties are an intrinsic attribute of simulation process. Subsequently, early numerical simulations considered tissue as homogeneous and isotropic, assuming an unchanging blood perfusion rate during tissue heating and lack of tissue structural changes at boiling point [53].

Most frequently used models for RF ablation consider a two- or three-dimensional geometry, which include some type of symmetry. These are multi-physics models solved by Finite Element Method (FEM) on a

macroscopic scale, in which each numerical compartment is represented by different tissue. Mathematical description focuses on electrical and thermal effects involved in current and temperature distributions, heat transfer and cellular death during lesion formation. These phenomena are described by the governing equations including the main governing equation for heat transfer in biological tissues, Pennes bioheat equation:

$$\rho c \frac{\partial T}{\partial t} = \nabla \cdot (k \nabla T) + q - Q_p + Q_m \tag{1}$$

where ρ, c, k are the density, heat capacity and thermal conductivity. T stands for temperature, Q_p and Q_m are the heat loss terms for perfusion heat loss and metabolic heat, respectively, while q is source therm. A detailed expression for heat sink effect from blood flow is as follows:

$$Q_p = \omega_b \cdot c_b \cdot (T - T_b) \tag{2}$$

where ω_b, c_b, T_b state for blood perfusion, specific heat of blood and blood temperature. The term ω_b is usually considered constant during ablation, although some studies consider perfusion cessation for thermally damaged tissue [54,55].

The lesion degree and size can be defined by different models for necrotic coagulation. The simplest one focuses on defining a threshold temperature above which cells become instantaneously dead. This approach is widely used for estimation of *in vivo* lesion size where the discolored necrotic tissue is determined by a 50°C iso-contour. Although it has been employed in computer models, the method lacks in precision since it does not consider the time of cellular exposure to high temperatures [56].

Another method frequently used for modeling is the cumulative damage integral computed using Arrhenius equation proposed by Moritz and Henriques [57]:

$$\Omega(t) = \ln\left(\frac{c(0)}{c(t)}\right) = A\int \exp\left(-\frac{\Delta E}{RT(t)}\right) dt \tag{3}$$

where $\Omega(t)$ is the degree of tissue injury, $c(t)$ is the concentration of living cells, A is a frequency factor for the kinetic expression, ΔE is the activation energy

for irreversible damage reaction, and R is the universal gas constant [55]. According to this expression, tissue thermal necrosis is linear with time but increases exponentially with temperature. Damage integral is considered Ω=1 or Ω=4.6 for 63% and 99% probability of death, respectively. The major complication of this method is the need to establish the value A and ΔE, which is not an easy task.

Another models are thermal dose models, which state the thermal dose in an equivalent time at a fixed temperature of 43ºC:

$$t_{43} = \sum_{t=0}^{t-final} C^{(43-\bar{T})} \Delta t \tag{4}$$

where t_{43} is the thermal dose in equivalent minutes at 43ºC, C is a constant defined as C=0.5 for $\bar{T}$>43ºC and C=0.25 for $\bar{T}$<42ºC, $\bar{T}$ is the average temperature during the time interval Δt [58]. The main consideration is that the final result of cumulative damage is cellular death, and a lethal thermal dose for necrotic tissue the value of t_{43}=240 min is assumed.

Resistive heating is computed from:

$$q = \boldsymbol{J} \cdot \boldsymbol{E} \tag{5}$$

where $\boldsymbol{E}$ is the electrical field obtained from the Laplace equation for conductive media [59]:

$$\nabla \cdot \sigma \nabla \boldsymbol{V} = 0 \tag{6}$$

where V and σ are the voltage and electrical conductivity, respectively; and $\boldsymbol{J}$ is the current density computed from:

$$\boldsymbol{J} = \sigma \cdot \boldsymbol{E} \tag{7}$$

At the frequencies employed, tissue can be considered as purely resistive, and hence $\boldsymbol{J}$ and $\boldsymbol{E}$ are vectors with the same direction. In terms of numerical solving techniques, the accumulation of resistive heating (Joule effect) close to the usually thin electrode tip requires a dense mesh in this location and therefore higher computational cost.

Temperature changes affect the electrical and thermal properties of tissues and they have to be modeled accurately. The ranges of values for material properties such as tissue density, specific heat, electrical and thermal conductivities, water content or blood perfusion are based on numerous experimental studies that characterize their dependency on temperature, location and time. However, it is also often related to model variability, which can be reduced by performing sensitivity analysis [60]. The way the electrical and thermal conductivities are defined and the inclusion of vaporization phenomena may also have a huge impact on modeled thermal lesion size. Several approaches have considered the temperature dependence of electrical and thermal conductivity, however a study showed there was no significant difference between these approaches in how they affected thermal lesion size [61]. The functions for mathematically modeling electrical conductivity always consider a linear or exponential growth until reaching 100ºC when vaporization occurs. Above 100ºC a rapid drop of σ value is assumed, estimated in several orders of magnitude during the subsequent 2-5ºC or until reaching a value close to zero that posteriorly remains constant [62-64]. Regarding thermal conductivity mathematical description assumes a constant value or a linearly increasing function below 100ºC and a constant value for temperatures greater than 100ºC [63,65].

Finally, Abraham's formulation also extends the mathematical description of vaporization by including the enthalpy method accounting for liquid-to-vapor phase change. It assumes a three-part formulation for the pre-phase-change, phase-change and post-phase-change tissue conditions expressed as follows:

$$h_t = \begin{cases} (\rho c)_t^{pre}(T_t - 37^{\circ}\mathrm{C}), & 37 \le T_t \le 99^{\circ}\mathrm{C} \\ h_t(99) + h_{fg} \cdot C_{liq} \cdot \dfrac{(T_t - 99^{\circ}\mathrm{C})}{(100 - 99^{\circ}\mathrm{C})}, & 99 < T_t \le 100^{\circ}\mathrm{C} \\ h_t(100) + (\rho c)_t^{post}(T_t - 100^{\circ}\mathrm{C}), & T_t > 100^{\circ}\mathrm{C} \end{cases} \quad (8)$$

where ρ, c are the density and specific heat, h_{fg} is the latent heat of evaporation, C_{liq} is the concentration of the liquid in the tissue, also called the water content.

1.5.2. *Experimentation models*

Despite the efforts toward increasing efficiency and reducing research time and cost through advancements in theoretical research, experimentation modeling remains an essential part of research in order to provide realistic testing and validation for the performance and safety of new technologies. Numerous studies have therefore been based on phantom and animal models or clinical trials. The most controversial practice concerns animal experimentation, however presently, no other viable option has yet been found to replace testing on animals. Moreover ethical and legal requirements have been posed to standardize experimentation procedures and prevent from animal abuse.

Regarding RFA experimentation, phantom and explanted tissue are basic models for the ablation study (Figure 4). Their major advantages are low cost, availability and also the possibility to produce various ablations using one tissue specimen. Subsequently, other organs from the same animal can be used for a variety of different studies reducing the number of experimental animals.

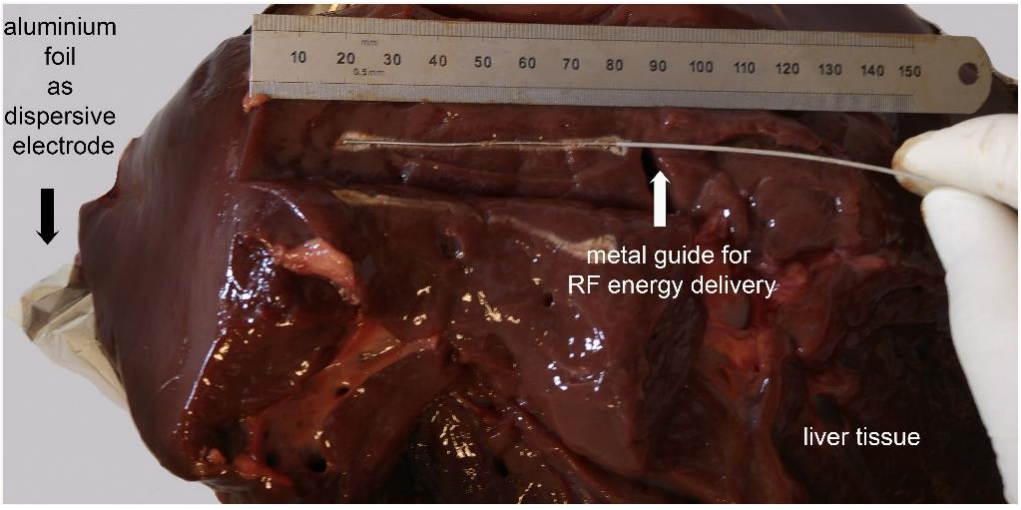

Figure 4. Example of RFA experiment on liver tissue *ex vivo* model.

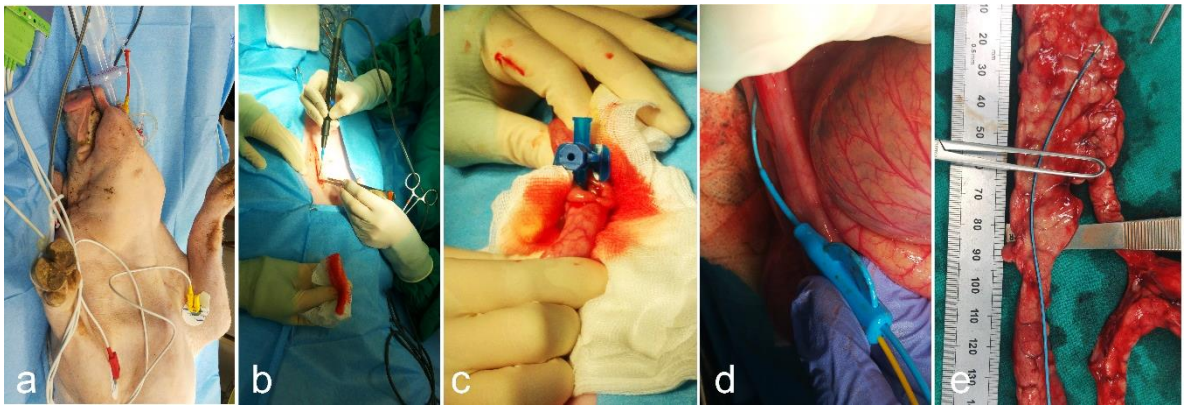

Figure 5. Example of endoluminal RFA ablation of pancreatic duct with bipolar catheter on *in vivo* pig model. (a) animal sedation (b) opening of the abdominal cavity, (c) cannulation of the major papilla, (d) insertion of bipolar RF catheter, (e) postoperatory organ excision and the orientational length of the ablated segment.

The most commonly used organs for hepatic ablation study are porcine and bovine livers since they are comparable to their human equivalent. No ethical approval is required for *ex vivo* study and the models are usually applied in the initial study stages as suitable for comparison of different settings and protocols in similar, homogeneous conditions [40,45,48,49]. *Ex vivo* experimentation is naturally limited due to the absence of perfusion-mediated tissue cooling and physiological response of a living body. Thus, the extent of coagulation necrosis a non-perfused tissue is unrealistic if unaffected by heat sink effect or other systemic responses as inflammatory response [1]. They are also time-limited since thermal lesions can be examined only at the time of ablation with no further evolution over time. Excised tissue is also less hydrated and its body temperature decreases to an ambient state; however these issues can be further controlled by adequate study setting.

In vivo model results are usually variable and less reproducible than *ex vivo* models, as they are affected by the presence of the vascular system. For experimental procedures, a specialized laboratory facility, legal approval and a constant animal care during the study are required. An example of *in vivo* procedure has been shown on Figure 5. Drug administration during surgeries including administering anesthesia and surgery, should be performed by well-trained personnel, and potential side effects of medication on RF

ablation results should be examined. Moreover, possible variability between specimens such as weight, sex or age should be considered to avoid heterogeneity of study sample. Regardless of these limitations this approach provides the opportunity of a follow-up study to examine thermal lesion evolution over time and histological analysis [66]. The results can be directly transferred to clinical practice as they include all the possible physiologic responses that could be observed in humans [47]. Apart from involving blood perfusion component, it also enables the employment of more complex tumor models, which have been proven to differ in thermal-electrical properties from healthy tissues [51].

Finally, as an alternative to *ex vivo* and *in vivo* models, isolated *ex vivo* perfused models were proposed. The excised organ would be perfused using autologous blood to maintain physiological and metabolic functions, preserving natural organ architecture. The method is considered suitable for temporal and histological studies of RF lesions and even for early inflammatory response examination. Despite its physiological complexity it does not require legal approval and is less costly compared to *in vivo* experimentation. They also offer the possibility of studying the effect of perfusion rate modulation in the organ. One of the first models to employ this approach was liver perfusion model, which were also typically used in studies of metabolism and toxicity, and for RF ablation of a tumor-mimic model [52]. Nevertheless, *ex vivo* perfused models require a relatively freshly excised organ from animal under anesthesia and are limited by perfusion lifespan no longer than several hours. Another concern is the lack of the interacting organs that could be involved in patient recovery and final study result when performing the intervention.

The main focus of this work was put on analyzing thermal and electrical effects of RFA in the following applications of interventional medicine: pain relief, liver tumor ablation and pancreatic remnant management after surgical resection. Thus the key objectives could be defined as: (1) development of computer models to study electrical and thermal effects of

RFA for tissue selective destruction applied in tumor focal ablation and surgical resection; and (2) *ex vivo* and *in vivo* experimental validation of computer models for RFA. Different computer models and experimental studies were employed to accomplish these objectives. All computer models were built using Finite Element Method by means of COMSOL Software. Experimental studies involved agar phantoms, excised liver and pancreas specimens for *ex vivo* study, pig models for *in vivo* study and clinical trial in cancer patients. The main findings of this research have contributed to: (1) shedding light on the electrical and thermal effects of different pulsed radiofrequency protocols used for pain relief and a possible related nerve electroporation, (2) the analysis of a new RF catheter design for an improved tissue hydration and a more effective liver tumor radiofrequency ablation, and finally (3) proposing and analyzing a new technique of pancreatic duct sealing for management of pancreatic remnant.

References

[1] Goldberg SN, Gazelle GS, Mueller PR. Thermal ablation therapy for focal malignancy: a unified approach to underlying principles, techniques, and diagnostic imaging guidance. AJR Am J Roentgenol. 2000;174(2):323-31.

[2] Facciorusso A, Serviddio G, Muscatiello N. Local ablative treatments for hepatocellular carcinoma: An updated review. World J Gastrointest Pharmacol Ther. 2016;7(4):477-489.

[3] Kim SW, Rhim H, Park M, et al. Percutaneous radiofrequency ablation of hepatocellular carcinomas adjacent to the gallbladder with internally cooled electrodes: assessment of safety and therapeutic efficacy. Korean J Radiol. 2009;10(4):366-76.

[4] Stättner S, Jones RP, Yip VS, et al. Microwave ablation with or without resection for colorectal liver metastases. Eur J Surg Oncol. 2013;39(8):844-9.

[5] Jeanmonod D, Werner B, Morel A, et al. Transcranial magnetic resonance imaging-guided focused ultrasound: noninvasive central lateral thalamotomy for chronic neuropathic pain. Neurosurg Focus. 2012;32(1):E1.

[6] Ram Z, Cohen ZR, Harnof S, et al. Magnetic resonance imaging-guided, high-intensity focused ultrasound for brain tumor therapy. Neurosurgery. 2006;59(5):949-55.

[7] Rao MS, Hargreaves EL, Khan AJ, et al. Magnetic resonance-guided laser ablation improves local control for postradiosurgery recurrence and/or radiation necrosis. Neurosurgery. 2014;74(6):658-67.

[8] Moreland AJ, Ziemlewicz TJ, Best SL, et al. High-powered microwave ablation of t1a renal cell carcinoma: safety and initial clinical evaluation. J Endourol. 2014;28(9):1046-52.

[9] Merckel LG, Knuttel FM, Deckers R, et al. First clinical experience with a dedicated MRI-guided high-intensity focused ultrasound system for breast cancer ablation. Eur Radiol. 2016;26(11):4037-4046.

[10] Vargas HI, Dooley WC, Gardner RA, et al. Focused microwave phased array thermotherapy for ablation of early-stage breast cancer: results of thermal dose escalation. Ann Surg Oncol. 2004;11(2):139-46.

[11] Yoshinaga Y, Enomoto Y, Fujimitsu R, et al. Image and pathological changes after radiofrequency ablation of invasive breast cancer: a pilot study of nonsurgical therapy of early breast cancer. World J Surg. 2013;37(2):356-63.

[12] van Esser S, Stapper G, van Diest PJ, et al. Ultrasound-guided laser-induced thermal therapy for small palpable invasive breast carcinomas: a feasibility study. Ann Surg Oncol. 2009;16(8):2259-63.

[13] de Baère T, Aupérin A, Deschamps F, et al. Radiofrequency ablation is a valid treatment option for lung metastases: experience in 566 patients with 1037 metastases. Ann Oncol. 2015;26(5):987-91.

[14] Yang X, Ye X, Zheng A, et al. Percutaneous microwave ablation of stage I medically inoperable non-small cell lung cancer: clinical evaluation of 47 cases. J Surg Oncol. 2014;110(6):758-63.

[15] Rehnitz C, Sprengel SD, Lehner B, et al. CT-guided radiofrequency ablation of osteoid osteoma and osteoblastoma: clinical success and long-term follow up in 77 patients. Eur J Radiol. 2012;81(11):3426-34.

[16] Etienne A, Waynberger É, Druon J. Interstitial laser photocoagulation for the treatment of osteoid osteoma: retrospective study on 35 cases. Diagn Interv Imaging. 2013;94(3):300-10.

[17] Cucchetti A, Piscaglia F, Cescon M, et al. Systematic review of surgical resection vs radiofrequency ablation for hepatocellular carcinoma. World J Gastroenterol. 2013 14;19(26):4106-18.

[18] Wells S, Hinshaw JL, Lubner MG, et al. Liver Ablation: Best Practice. Radiol Clin North Am. 2015; 53(5): 933–971.

[19] Habash RW, Bansal R, Krewski D, et al. Thermal Therapy, Part III: Ablation Techniques. Crit Rev Biomed Eng. 2007;35(1-2):37-121.

[20] Dewhirst MW, Viglianti BL, Lora-Michiels M. Basic principles of thermal dosimetry and thermal thresholds for tissue damage from hyperthermia. Int J Hyperthermia. 2003;19(3):267-94.

[21] Goldberg SN. Radiofrequency tumor ablation: principles and techniques. Eur J Ultrasound. 2001;13(2):129-47.

[22] Cushing H, Bovie WT. Electro-surgery as an aid to the removal of intracranial tumors. Surg. Gynec. Obstet. 1928;47, 751-84.

[23] Huang SK, Graham AR, Hoyt RH, Odell RC. Transcatheter desiccation of the canine left ventricle using radiofrequency energy: a pilot study. Am Heart J. 1987;114(1 Pt 1):42–48.

[24] Clark W. Oscillatory desiccation in the treatment of accessible malignant growths and minor surgical conditions. J Adv Ther. 1911;29:169–183.

[25] Taha JM, Tew JM Jr, Buncher CR. A prospective 15-year follow up of 154 consecutive patients with trigeminal neuralgia treated by percutaneous stereotactic radiofrequency thermal rhizotomy. J Neurosurg. 1995;83(6):989-93.

[26] Fitzpatrick R, Geronemus R, Goldberg D, et al. Multicenter study of noninvasive radiofrequency for periorbital tissue tightening. Lasers Surg Med. 2003;33(4):232-42.

[27] Kim ED, Lee YI, Park HJ. Comparison of efficacy of continuous epidural block and pulsed radiofrequency to the dorsal root ganglion for management of pain persisting beyond the acute phase of herpes zoster. PLoS One. 2017;12(8):e0183559.

[28] Friedman M, Mikityansky I, Kam A, et al. Radiofrequency ablation of cancer. Cardiovasc Intervent Radiol. 2004;27(5):427–434.

[29] Goldberg SN, Gazelle GS, Dawson SL, et al. Tissue ablation with radiofrequency: effect of probe size, gauge, duration, and temperature on lesion volume. Acad Radiol. 1995;2(5):399-404.

[30] Livraghi T, Goldberg SN, Lazzaroni S, et al. Hepatocellular carcinoma: radio-frequency ablation of medium and large lesions. Radiology. 2000;214(3):761-8.

[31] Mulier S, Miao Y, Mulier P, et al. Electrodes and multiple electrode systems for radiofrequency ablation: a proposal for updated terminology. Eur Radiol. 2005;15(4):798-808.

[32] Braithwaite, B, Hnatek, L, Zierau, U, et al. Radiofrequency-induced thermal therapy: results of a European multicentre study of resistive ablation of incompetent truncal varicose veins. Phlebology: The Journal of Venous Disease. 2012;28(1), 38–46.

[33] Steel AW, Postgate AJ, Khorsandi S, et al. Endoscopically applied radiofrequency ablation appears to be safe in the treatment of malignant biliary obstruction. Gastrointest Endosc. 2011;73(1):149-53.

[34] Boersma D, Kornmann VN, van Eekeren RR, et al. Treatment Modalities for Small Saphenous Vein Insufficiency: Systematic Review and Meta-analysis. J Endovasc Ther. 2016;23(1):199-211.

[35] Rustagi T, Jamidar PA. Intraductal Radiofrequency Ablation for Management of Malignant Biliary Obstruction. Digestive Diseases and Sciences. 2014;59(11), 2635–2641.

[36] Mensah ET, Martin J, Topazian M. Radiofrequency ablation for biliary malignancies. Curr Opin Gastroenterol. 2016;32(3):238-43.

[37] Van Zundert J, Lame IE, De Louw A, et al. Percutaneous pulsed radiofrequency treatment of the cervical dorsal root ganglion in the treatment of chronic cervical pain syndromes: A clinical audit. Neuromodulation. 2003;6:6–14.

[38] Simopoulos TT, Kraemer J, Nagda JV, et al. Response to pulsed and continuous radiofrequency lesioning of the dorsal root ganglion and segmental nerves in patients with chronic lumbar radicular pain. Pain Physician. 2008;11:137–144.

[39] Tsou HK, Chao SC, Wang CJ, et al. Percutaneous pulsed radiofrequency applied to the L-2 dorsal root ganglion for treatment of chronic low-back pain: 3-year experience. J Neurosurg Spine. 2010;12:190–196.

[40] Cosman ER Jr, Cosman ER Sr. Electric and thermal field effects in tissue around radiofrequency electrodes. Pain Med. 2005;6(6):405-24.

[41] Van Zundert J, de Louw AJ, Joosten EA, et al. Pulsed and continuous radiofrequency current adjacent to the cervical dorsal root ganglion of the rat induces late cellular activity in the dorsal horn. Anesthesiology. 2005;102(1):125-31.

[42] Sluijter ME, Cosman ER, Rittman WB, Van Kleef M. The effects of pulsed radiofrequency fields applied to the dorsal root ganglion - a preliminary report. Pain Clin 1998; 11:109–17.

[43] Byrd D, Mackey S. Pulsed radiofrequency for chronic pain. Curr Pain Headache Rep. 2008;12(1):37–41.

[44] Wittkampf FH, Nakagawa H, Yamanashi WS, et al. Thermal latency in radiofrequency ablation. Circulation. 1996;93(6):1083-6.

[45] Lee JM, Han JK, Kim SH, et al. Saline-enhanced hepatic radiofrequency ablation using a perfused-cooled electrode: comparison of dual probe bipolar mode with monopolar and single probe bipolar modes. Korean J Radiol. 2004;5(2):121-7.

[46] Goldberg SN, Gazelle GS, Solbiati L, et al. Radiofrequency tissue ablation: increased lesion diameter with a perfusion electrode. Acad Radiol. 1996;3(8):636-44.

[47] Livraghi T, Goldberg SN, Monti F, et al. Saline-enhanced radio-frequency tissue ablation in the treatment of liver metastases. Radiology. 1997;202(1):205-10.

[48] Miao Y, Ni Y, Yu J, et al. An ex vivo study on radiofrequency tissue ablation: increased lesion size by using an "expandable-wet" electrode. Eur Radiol. 2001;11(9):1841-7.

[49] Burdío F, Berjano E, Navarro A, et al. RF tumor ablation with internally cooled electrodes and saline infusion: what is the optimal location of the saline infusion? Biomed Eng Online. 2007; 6:30.

[50] Ni Y, Miao Y, Mulier S, et al. A novel "cooled-wet" electrode for radiofrequency ablation. Eur Radiol. 2000;10(5):852-4.

[51] Boehm T, Malich A, Goldberg SN, et al. Radio-frequency tumor ablation: internally cooled electrode versus saline-enhanced technique in an aggressive rabbit tumor model. Radiology. 2002;222(3):805-13.

[52] Hildebrand P, Kleemann M, Roblick U, et al. Development of a perfused ex vivo tumor-mimic model for the training of laparoscopic radiofrequency ablation. Surg Endosc. 2007;21(10):1745-9.

[53] Berjano EJ. Theoretical modeling for radiofrequency ablation: state-of-the-art and challenges for the future. Biomed Eng Online. 2006;5:24.

[54] Ahmed M, Liu Z, Humphries S, et al. Computer modeling of the combined effects of perfusion, electrical conductivity, and thermal conductivity on tissue heating patterns in radiofrequency tumor ablation. Int J Hyperthermia. 2008;24(7):577-88.

[55] Chang IA, Nguyen UD. Thermal modeling of lesion growth with radiofrequency ablation devices. Biomed Eng Online. 2004;3(1):27.

[56] Panescu D, Whayne JG, Fleischman SD, et al. Three-dimensional finite element analysis of current density and temperature distributions during radio-frequency ablation. IEEE Trans Biomed Eng. 1995;42(9):879-90.

[57] Moritz A, Henriques F. Studies of thermal injury II. The relative importance of time and surface temperature in the causation of thermal burns. Am J Pathol 1947; 23: 695–720.

[58] Sapareto SA, Dewey WC. Thermal dose determination in cancer therapy. Int J Radiat Oncol Biol Phys. 1984;10(6):787-800.

[59] Doss JD. Calculation of electric fields in conductive media. Med Phys. 1982;9(4):566-73.

[60] Hall SK, Ooi EH, Payne SJ. Cell death, perfusion and electrical parameters are critical in models of hepatic radiofrequency ablation. Int J Hyperthermia. 2015;31(5):538-50.

[61] Trujillo M, Berjano E. Review of the mathematical functions used to model the temperature dependence of electrical and thermal conductivities of biological tissue in radiofrequency ablation. Int J Hyperthermia. 2013;29(6):590-7

[62] Byeongman J, Aksan A. Prediction of the extent of thermal damage in the cornea during conductive thermokeratoplasty. J Therm Biol 2010;35:167–74. 14.

[63] Haemmerich D, Chachati L, Wright AS, Mahvi DM, Lee FT, Webster JG. Hepatic radiofrequency ablation with internally cooled probes: Effect of coolant temperature on lesion size. IEEE Trans Biomed Eng 2003;50:493–9.

[64] Pätz T, Kröger T, Preusser T. Simulation of radiofrequency ablation including water evaporation. IFMBE Proceedings 2009;25/IV: 1287–90.

[65] Abraham JP, Sparrow EM. A thermal-ablation bioheat model including liquid-to-vapor phase change, pressure- and necrosis-dependent perfusion, and moisture-dependent properties. Int J Heat Mass Transfer 2007;50:2537–44.

[66] Patterson EJ, Scudamore CH, Owen DA, et al. Radiofrequency ablation of porcine liver in vivo: effects of blood flow and treatment time on lesion size. Ann Surg. 1998;227(4):559-65

Chapter 2

Effect of applied voltage, duration and repetition frequency of RF pulses for pain relief on temperature spikes and electrical field: A computer modeling study

2.1. Abstract

The thermal and electrical effects of pulsed radiofrequency (PRF) for pain relief can be controlled by modifying the characteristics of the RF pulses applied. Our goal was to evaluate the influence of such modifications on the thermal and electric performance in tissue. A computational model was developed to compare the temperature and electric field time courses in tissue between a standard clinical protocol (45 V pulses, 20 ms duration, 2 Hz repetition frequency) and a new protocol (55 V pulses, 5 ms duration, 5 Hz repetition frequency) with a higher applied electric field but a smaller impact on temperature alterations in tissue. The effect of including a temperature controller was assessed. Complementarily, an agar-based experimental model was developed to validate the methodology employed in the computer modeling. The new protocol increased the electric field magnitude reached in the tissue by around +20%, without increasing the temperature. The temperature controller was found to be the fundamental factor in avoiding thermal damage to the tissue and reduced the total number of pulses delivered by around 67%. The experimental results matched moderately well with those obtained from a computer model built especially to mimic the experimental conditions. For the same delivered

energy, the new protocol significantly increases the magnitude of the applied electric field, which may be the reason why it is clinically more effective in achieving pain relief.

2.2. Introduction

Radiofrequency (RF) energy is clinically used in pain management. In contrast to the wide area of the thermally coagulated zone manifested after continuous RF (CRF), pulsed RF (PRF) has demonstrated positive effects on pain treatment without provoking any permanent neurological disruptions [1–4]. While CRF causes pain relief by the effect of the tissue thermocoagulation creating irreversible injury to the target nerve, PRF involves lower temperatures (below 42-44ºC), which is considered to be the limit value at which no thermally induced necrosis is observed [5][6]. As a result, the PRF technique can be applied to the neural regions that have both sensory and motor fibers (e.g. peripheral nerves) without any risk of further motor deficits [7][8].

According to recent studies, there is no definitive explanation for the mechanisms involved in PRF. An exhaustive review of experimental observations regarding the potential PRF action mechanisms can be found in [9]. Different effects of exposure to PRF electrical fields have already been reported. Some studies have revealed evidence of morphological changes in the neuronal cells after PRF treatment that affect the inner structures of axons [1,10–12]. These structural changes consist of mitochondria swelling and disruption of the normal organization of the microtubules and microfilaments that preferentially affect C-fibers and to a lesser extent Aδ fibers. In addition, transient ultrastructural changes such as endoneurial edema and collagen deposition have also been found [13]. Besides structural changes, the effects on cellular activity and gene expression have also been observed [14][15] [1] as well as an increase in the expression of inflammatory proteins [12]. All these effects could potentially inhibit the transmission of nerve signals through C-fibers, which would lead to pain relief [9].

It is widely accepted that the PRF action mechanism is most likely related to the induced electric field, rather than to thermal effects. Several explanations of how exposure to an electric field can lead to the observed structural effects have been proposed, including: an alteration of the axonal membranes due to electroporation [16], an effect on the intracellular organelles due to the internal electric field [10] or a long-term depression of the synaptic transmission due to electrical stimulation [17]. However, to the best of our knowledge, no explanation has been postulated on how the electric field can trigger the observed changes in cellular activity and gene expression or the anti-inflammatory responses. A recent clinical study (employing a temperature control with the upper limit set at 42ºC) reinforces the hypothesis that the effects of PRF treatment are probably related to the electric field magnitude [18].

PRF has usually been based on a train of RF bursts (pulses) with a 10-20 ms duration and a 1-2 Hz repetition frequency [16],[19]. The application of each burst provokes a temperature spike in the electrode tip that could have destructive thermal effects. It has been observed from both computer and experimental models that the longer pulse durations cause higher temperature spike magnitudes [16]. With this idea in mind, a new timing pattern consisting of pulses of 5 ms duration and 5 Hz repetition frequency is being clinically employed in an attempt to reduce temperature spike magnitude [20]. In addition, this new timing pattern is associated with the use of higher values of applied voltage (55 V instead of 45 V). Surprisingly, the impact of this new protocol (55 V–5 ms–5 Hz) on temperature spike magnitudes and electric field has not as yet been assessed. Although the clinical outcome of the new protocol should be assessed by clinical studies, the computer modeling technique can be a valuable tool for studying the thermal and electrical performance of RF-based clinical techniques.

With the foregoing considerations in mind, we planned a computer modeling study aimed at assessing the differences between the standard protocol (SP) (45 V pulses with 20 ms duration and 2 Hz repetition frequency [21,22]) and the new protocol (NP) (55 V pulses with 5 ms duration and 5 Hz

repetition frequency [20]). An additional protocol (AP) consisting of 45 V pulses with 8 ms duration and 5 Hz repetition frequency was also considered, since it provides the same energy as the SP (20 ms × 2 Hz = 8 ms × 5 Hz = 40 ms/s) and employs the same repetition frequency as the NP protocol. In this way the influence of the pulse duration on both the AP and NP protocols could be evaluated. The computer models also included a temperature controller, similar to the one implemented in RF generators used in clinical practice, to assess the impact of this controlling technique on the temperature spike magnitudes and electric field. A complementary in vitro study based on an agar phantom was also conducted to validate the methodology used in the computational models.

2.3. Materials and methods

2.3.1. Model geometry

A PRF procedure was modeled with a 22-gauge needle electrode (0.64 mm in diameter) with a 10 mm long exposed tip. Figure 6a shows the two-dimensional model with three domains, consisting of muscle tissue, plastic cover (shaft) and electrode (exposed metallic part). The dispersive electrode (patch) was modeled as a zero voltage boundary condition on the outer boundaries (see Fig. 6). The optimal dimensions of all the outer boundaries were established by means of a sensitivity analysis in which the maximum temperature reached at the electrode tip (T^{MAX}) was used as the control parameter. The dimensions were gradually increased until the difference of T^{MAX} between two subsequent simulations was less than 0.5%, after which the dimensions of the previous model were considered to be adequate.

2.3.2. Material properties

The properties of the materials employed in the model are shown in Table 1. Tissue thermal conductivity (k) was assumed to be constant with temperature, while electrical conductivity (σ) was modeled as a temperature (T) dependent function that grows exponentially +1.5%/°C at temperatures up to 99ºC [23].

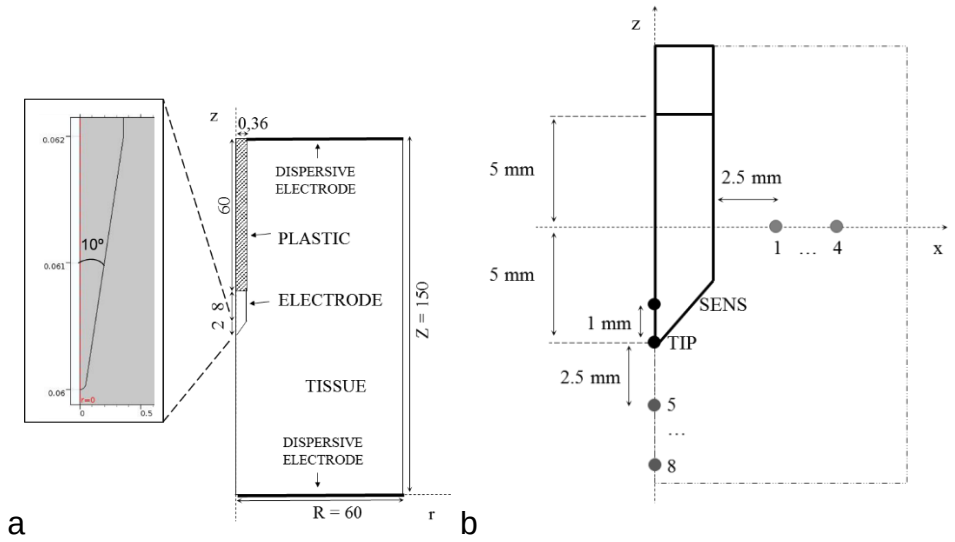

Figure 6. (a) Geometry of the model including tissue, metallic electrode and plastic cover of the RF applicator. Dimensions in mm (out of scale). Note the detail of the electrode tip (scale in mm) consisting of a conical point with a 10º angle and rounded endpoint with an arbitrary 0.05 mm radius, which was assumed to avoid an infinite singularity in the model. (b) Specific locations chosen for evaluation of time course of electric field magnitude and temperature. Eight of these are separated from each other by 2.5 mm (P_1–P_4 in horizontal axis and P_5–P_8 in vertical axis). SENS corresponds to a point inside the conical tip of the electrode at a distance of 1 mm from its tip (TIP).

Assuming that tissue temperature during PRF will stay below 99ºC, no desiccation due to water vaporization was modeled. The electrical conductivity of muscle tissue (at 37ºC) was set to 0.28 S/m. This led to an impedance magnitude of approximately 350 Ω between the needle electrode and the dispersive electrode.

Table 1. Electric and thermal properties of materials and tissue [24,36], [37].

Material	***σ* (S/m)**	***k* (W/m·K)**	***ρ* (kg/m³)**	***c* (J/kg·K)**
Muscle	0.28 [a]	0.49	1090	3421
Plastic	10^{-5}	0.026	70	1045
Electrode	7.4×10^{6}	15	8×10^{3}	480

[a] This value (at 37ºC) was considered in order to match the simulated initial impedance to the clinically observed values (~350 Ω, see Section 2.3.2 *Material properties*).

σ: electrical conductivity; *k*: thermal conductivity; *ρ*: density; *c*: heat capacity.

This same value is typically found during PRF treatment under the same conditions as those used in this study and derives from the dielectric properties of the different tissues encountered along the path of the electric current. This value lies between those reported for muscle (0.45 S/m) and nerve (0.11 S/m) [24], and matches well with the physical situation in PRF, in which the electrode is inserted into muscle adjacent to a target nerve.

2.3.3. Numerical model

The computational model was based on a coupled electric-thermal problem. A quasi-static approach was proposed for the solution. The governing equation for the electrical problem was:

$$\nabla \cdot (\sigma(T)\nabla V) = 0 \tag{1}$$

where V is the voltage, which is related with the electric field ($\boldsymbol{E}$) by

$$\boldsymbol{E} = -\nabla V \tag{2}$$

The thermal problem was solved using the *Bioheat Equation*:

$$\rho c \frac{\partial T}{\partial t} = \nabla \cdot (k\nabla T) + q + Q_m + Q_p \tag{3}$$

where ρ is density of tissue, c specific heat, k thermal conductivity, T temperature, t time, q heat source generated by RF power, Q_m metabolic heat generation (not considered in RF ablation) and Q_p heat loss from blood perfusion described as:

$$Q_p = -\omega_b \rho_b c_b (T_a - T) \tag{4}$$

where ω_b is the blood perfusion coefficient equal to 6.63×10^{-4} s^{-1} (volume blood per unit mass tissue per unit time), ρ_b and c_b are the density and specific heat blood of values 1000 kg/m^3 and 4180 J/(kg·K) respectively and T_a is the temperature of the arterial blood (37ºC) [25]. The heat source q was taken from the electrical problem and evaluated as $q = \boldsymbol{J} \cdot \boldsymbol{E}$, where $\boldsymbol{J}$ is the current density, which is obtained from $\boldsymbol{J} = \sigma \boldsymbol{E}$. No blood perfusion was assumed

when tissue reached a 99% probability of thermal necrosis. The degree of thermal necrosis was estimated by a function based on the Arrhenius model:

$$\Omega(t) = \int_0^t A e^{\frac{-\Delta E}{RT}} d\tau \qquad (5)$$

where R is the universal gas constant, A frequency factor, 3×10^{44} s^{-1} and ΔE activation energy for the irreversible damage reaction, 2.90×10^{5} J/mol [26]. Thermal damage contours were estimated with the isolines $\Omega = 4.6$ and $\Omega = 1$, which correspond to a 99% and 63% probability of cell death, respectively. Regarding the electrical boundary conditions, no current was assumed on the symmetry axis or on the boundary parallel to it (see Fig. 6). Voltage (45 or 55 V) was set at the electrode and applied as a pulse train, while 0 V was set at the boundaries of the tissue perpendicular to the symmetry axis. Thermal boundary conditions involved the temperature on external boundaries fixed at 37°C. No heat flux was considered in the direction transverse to the symmetry axis. The initial temperature of the tissue was set to 37ºC.

Three protocols were considered. While a root-mean-square (RMS) voltage of 45 V is typically used in clinical practice with the SP, the NP usually involves higher magnitudes, values of 55 V [20] and even up to 60 V [27,28] have been proposed. Values of 45 V and of 55 V were simulated here. The value of 55 V combined with 5 ms–5 Hz is used, since it can deliver an energy value comparable to that of 45 V combined with 20 ms–2 Hz. This means that 20 ms–2 Hz with 45 V, 8 ms–5 Hz with 45 V, and 5 ms–5 Hz with 55 V are equivalent protocols in terms of energy supplied to the tissue.

2.3.4. Analysis of thermal and electric performance

To analyze the thermal and electric performance a set of points of interest were defined as shown in Figure 6b. Thermal analysis included the temperature time course at an internal point of the sharp end of the electrode (SENS) and at the electrode point (TIP). For each pulse, the maximum (T^{MAX}) and minimum (T^{MIN}) temperatures reached in the tissue close to the

electrode tip were analyzed, along with the temperature spike magnitude (T^S) obtained as $T^{MAX} - T^{MIN}$. To be more precise, T^{MAX} was the temperature measured at the end of each pulse, while T^{MIN} was the lowest value reached just before starting the pulse. In the electric analysis, the RMS (root-mean-square) value of electric field magnitude ($|\boldsymbol{E}|$) was assessed at point TIP and at eight locations in the tissue, equally distributed across radial (P_1 - P_4) and axial directions (P_5 - P_8) (see Fig. 6b). These two directions were chosen as they are known to have different electric performances [16].

2.3.5. Temperature controller

The PRF procedure is habitually conducted with a temperature controller in order to avoid thermal lesions in the tissue due to excessive heating [19,29,30]. This control is achieved by means of a temperature sensor placed at the exposed sharpened tip of the electrode. To keep sensor temperature below the threshold of 42ºC, the applied voltage is modified accordingly, either by gradually reducing voltage or by transiently switching off the pulse application when tip temperature rises above the permitted maximum [1,7,10,14,21]. The SENS point shown in Figure 6b was defined specifically to mimic the location of the temperature sensor [16]. The temperature control was implemented in the model as an algorithm switching the input voltage between non-zero (*on* state) and zero value (*off* state). The state was determined in time by an implicitly defined event for which 42ºC and 41ºC measured at the SENS point were temperature set points for *off* and *on* states, respectively.

2.3.6. Meshing and model solver

A heterogeneous triangular mesh was used with 5,312 elements and 25,578 degrees of freedom. A refinement in the area surrounding the electrode was applied. Mesh size was determined by a convergence test computed for the maximum tissue temperature (T^{MAX}) and was gradually increased until the

differences in T^{MAX} between simulations were less than 0.5%. The criterion used for time step optimization was the difference in temperatures, which was required to be less than 0.5°C between two consecutive simulations. The model was solved by the Finite Element Method using COMSOL Multiphysics 5.1 software (COMSOL AB, Stockholm, Sweden).

2.3.7. Experimental validation

In order to validate the methodology used in the computational model, an experimental model based on an agar phantom (0.1% NaCl, dimensions 86.5×86.5×38 mm) was employed to obtain thermal and electrical measurements. Figure 7a shows an overview of the experimental setup.

A disposable 18G 10-mm RF electrode (St. Jude Medical, Saint Paul, MN, USA) was inserted halfway into the agar phantom wall. A 0.1 mm-thick transparent polyethylene foil covering the wall of electrode insertion was used as an adiabatic window transparent to infrared light. Two varnished copper wires (0.19 mm in diameter) were employed as probes to pick up the voltage value at 1 mm and 2 mm from the RF electrode surface. The wire tips were perpendicularly inserted 0.5 mm into the agar.

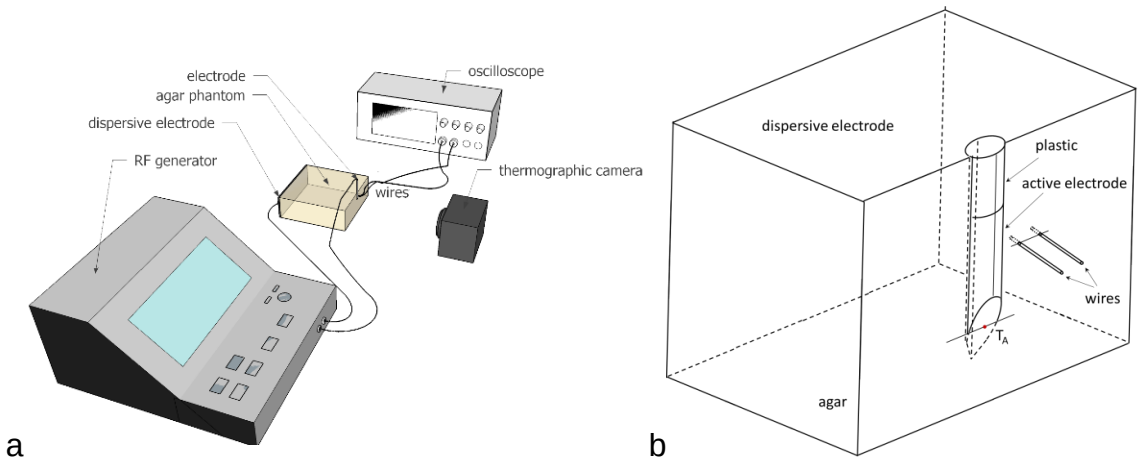

Figure 7. (a) Overview of the in vitro experimental setup based on an agar phantom. (b) Geometry of the computer model built to mimic the experimental setup (not to scale). The dispersive electrode was modeled on the wall parallel to the wall of electrode insertion.

Voltage differences with respect to the dispersive electrode of the RF generator were recorded with an Agilent DSO 1000 digital oscilloscope (Keysight Technologies, Santa Rosa, CA, USA) at a sampling rate of 1 S/s. A PRF protocol of 20 ms × 2 Hz and 45 V pulses was applied during a 2-minute period using an RF Neurotherm lesion generator (St. Jude Medical, Saint Paul, MN, USA). Temperatures were recorded by FLIR Model E60 infrared camera (FLIR Systems, Wilsonville, OR, USA).

The validation was complemented with a computational model specifically designed to mimic the conditions of the experimental setup (see Fig. 7b). Its main distinctive features were: three-dimensional geometry, agar electrical conductivity of 0.31 S/m, no blood perfusion, ambient temperature of 21ºC, and thermal insulation on the walls. The model also considered the presence of the voltage recording wires connected to the oscilloscope both thermally and electrically. These two wires not only acted as small thermal sinks but, since the input impedance of each channel was ~20 kΩ at 500 kHz (input impedance 1 MΩ||15 pF), stray RF current could flow from the electrode through the wires and the oscilloscope to the reference point. The model mimicked this phenomenon by adding an external circuit to the simulated domain consisting of two 20 kΩ resistors, one for each wire. The computer results (temperature distributions and progress of the voltage at 1 mm and 2 mm away from the RF electrode) were compared to those obtained from the experiments.

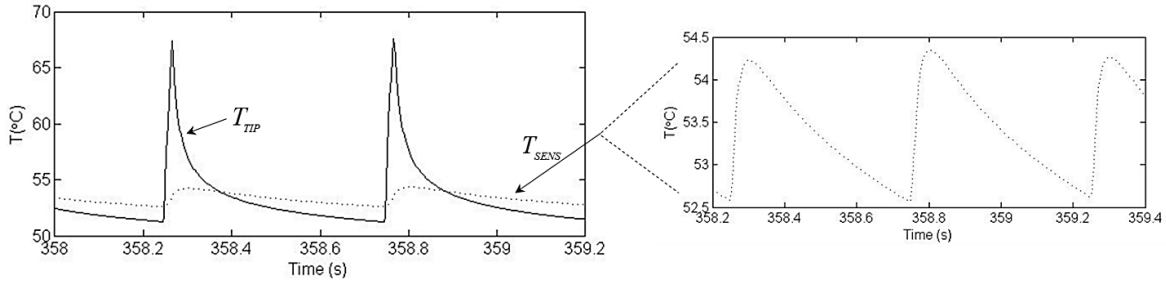

Figure 8. Time course of the two last temperature spikes (in ºC) at the electrode tip (T_{TIP}) and inside the electrode (T_{SENS}) after 6 min for the standard protocol (45 V–20 ms–2 Hz). The time course of T_{SENS} is presented in detail in the additional window. Note that temperature spike magnitude (assessed as: $T^{MAX} - T^{MIN}$) was much smaller at the SENS point.

2.4. Results

2.4.1. Thermal performance

Figure 8 shows the last 2 s of the temperature time courses at points TIP and SENS for the SP (45 V – 20 ms – 2 Hz) for 6 minutes without TC. The courses were qualitatively similar at both points and were characterized by abrupt rises at the start of each RF pulse and decayed exponentially during off-periods between consecutive pulses. Table 2 shows the minimal and maximal temperatures, along with the temperature spike magnitude computed at both points for the three different timing patterns and two voltage values, as well as for the cases with and without TC.

Table 2. Minimal (T^{MIN}) and maximal (T^{MAX}) temperatures, and temperature spikes (T^{S}) assessed at the tip (TIP) and inside (SENS) the electrode after 6 min of PRF for different timing patterns (pulse duration × pulse repetition frequency) and applied voltages.

Timing pattern	**Location**	**Applied voltage**					
		45 V			**55 V**		
		T^{MIN}(ºC)	T^{MAX}(ºC)	T^{S}(ºC)	T^{MIN}(ºC)	T^{MAX}(ºC)	T^{S}(ºC)
20 ms × 2 Hz	SENS	52.6	54.3	1.7	61.2	63.9	2.7
	TIP	51.3	67.4	16.1	59.2	84.2	25.0
8 ms × 5 Hz	SENS	53.8	54.5	0.7	60.9	61.8	0.9
	TIP	52.7	61.6	8.9	60.4	73.9	13.5
5 ms × 5 Hz	SENS	47.4	47.8	0.4	52.9	53.5	0.6
	TIP	46.7	53.2	6.5	51.8	61.7	9.9
20 ms × 2 Hz	SENS	41.0	42.6	1.6			
(TC)	TIP	40.6	56.8	16.2			
5 ms × 5 Hz	SENS				41.0	42.1	1.1
(TC)	TIP				40.6	51.1	10.5

TC: Cases with temperature controller (RF pulses were modulated in order to keep the temperature inside the electrode below 42ºC).

The main difference between the TIP and SENS points is that the T_{SENS} time course was a damped version of T_{TIP}. While T_{TIP}^{S} varied between 6.5 and 25.0ºC for all the cases considered, T_{SENS}^{S} only ranged from 0.4 to 2.7ºC. Interestingly, the temperatures registered at point SENS were generally very close to T_{TIP}^{MIN} values (differences of ~1ºC).

Figures 9a-9c show the temperature distributions in the zone close to the electrode tip for the three protocols (SP, AP and NP) just after the last RF pulse in the absence of a temperature controller. As expected, the temperature at the electrode tip was maximal just at the end of each RF pulse. When the RF pulse ends, heat is evacuated towards the electrode body. Similar T_{TIP}^{MAX} values were found for AP and NP. In contrast, the temperatures obtained with the SP were ~6ºC higher and a larger area surrounding the electrode tip reached high temperature values. The area of thermal lesion (assessed by contour Ω = 1) was similar for the three protocols and measured ~0.5 mm thick in the direction transverse to the electrode axis.

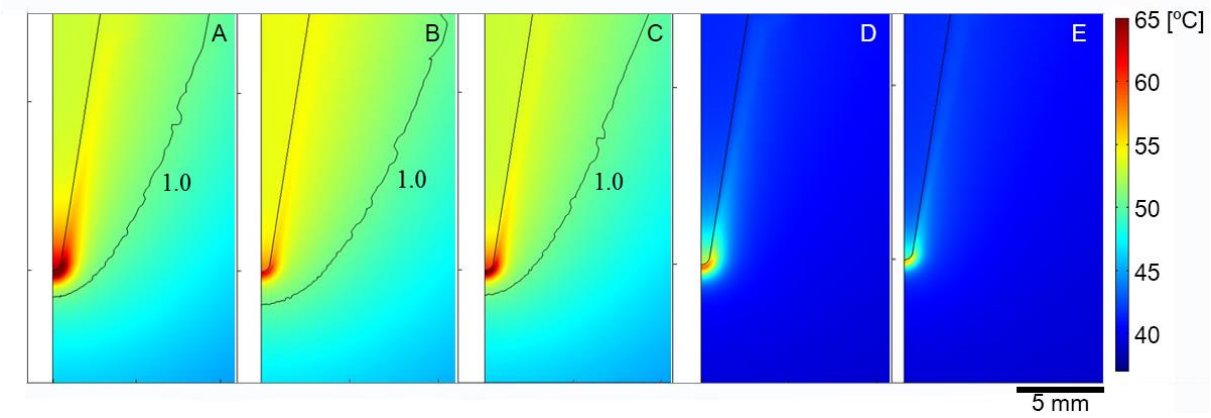

Figure 9. Temperature distributions close to electrode tip just after applying the last RF pulse for different protocols without (a-c) and with (d-e) temperature controller. (a) and (d) standard protocol (45 V–20 ms–2 Hz). (b) additional protocol (45 V–8 ms–5 Hz). (c) and (e) new protocol (55 V–5 ms–5 Hz). Black line is the damage contour Ω = 1 representing 63% of tissue damage. Note that the damage area is similar in (a-c), even though the maximum temperature reached in (a) is ~6ºC higher, while no thermal lesion is observed in the cases with temperature controller (d-e).

Likewise, Figures 9d and 9e show the temperature distributions in the zone close to the electrode tip for the SP and NP when the temperature controller was considered. As expected, the temperatures in the tissue showed the same spatial distribution as in the case with no temperature controller, but the absolute values were considerably lower. In fact, no thermal lesion was observed in any case. As shown in Table 2, the temperature controller kept T_{SENS}^{MAX} at ~42ºC, which meant T_{TIP}^{MIN} in both cases was close to 41ºC. Since T_{TIP}^{MAX} and T_{TIP}^{MIN} were both reduced by ~10ºC less than the cases with no TC, there was a negligible change of ~0.6ºC in the temperature spike magnitude. As a consequence, although the TC considerably reduced both the maximum and minimum temperatures, it seemed to have no effect on the temperature spike magnitude (T_{TIP}^{S} was similar both with and without the TC). Note that both T_{TIP}^{MAX} and T_{TIP}^{MIN} reached a plateau after ~21 s, which was approximately the time when T^{MIN} reached 42ºC and the controller came into action. The time evolution shown in Figure 10 was similar for the other protocols considered.

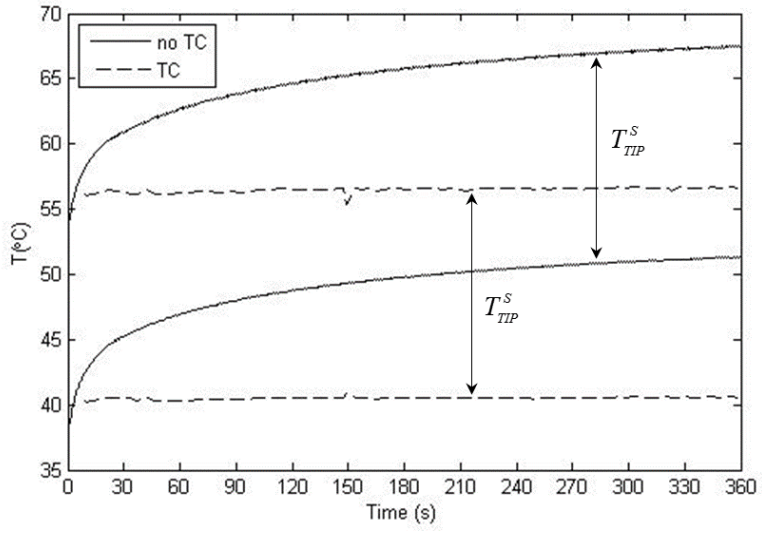

Figure 10. Comparison of time courses of maximal and minimal temperatures between the cases with and without temperature control (TC). Temperatures were assessed at the electrode tip and correspond with those of the standard protocol (45 V–20 ms–2 Hz).

Regarding the thermal performance of the in vitro experimental study, the situation of the temperature evolution at point T_A (see Fig. 7b for its location) was more or less comparable to that obtained from the corresponding computer model, with final temperatures of 26.73 ± 1.63ºC and 29.86ºC, in the experiments and simulations, respectively. The temperature measured at T_A was the maximum value registered by the camera. This value did not correspond to the highest temperature (which is usually expected to occur at the electrode tip point) since in this study the electrode tip was really embedded in the agar phantom. The temperature spikes in the experiments and simulations were similar (0.3 ± 0.1ºC vs. 0.2ºC). Figure 11 shows the temperature distributions of the experimental and computational models at 30 s intervals. The shape of the temperature distributions of the computer and experimental results was generally similar. While the thermal edge effect at the electrode tip was clearly visible in the experimental results (especially at 30 s), it was hardly noticeable in the computer results due to the plane view selected, which does not include the tip (see Fig. 7b). Moreover, the high reflectivity associated with certain metal elements (e.g. electrode and wire zones) disturbed the temperature mapping and unfortunately could not be minimized.

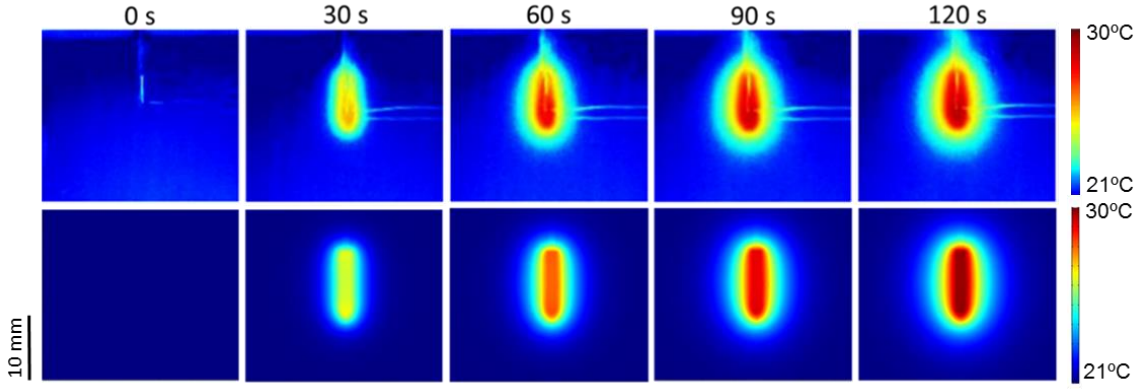

Figure 11. Temperature distributions from the in vitro experiments (upper) and computer modeling (bottom) at different times. Note that the wires designed to pick up voltage in the experiments (except their non-insulated ends) are really outside the agar phantom and are consequently not part of the material surface.

2.4.2. Electrical performance

The values of the electric field magnitude $|\mathbf{E}|$ were quite stable during PRF application with no TC ($|\mathbf{E}|$ variation was negligible during each pulse). As the $|\mathbf{E}|$ value is directly dependent on the voltage applied, it was therefore higher for NP (55 V-5 ms-5 Hz) than for SP (45 V-20 ms-2 Hz). On this account, the $|\mathbf{E}|$ value for the AP protocol (45 V-8 ms-5 Hz) coincided with those obtained for the SP (45 V-20 ms-2 Hz).

When the TC was employed, the total number of applied pulses was considerably lower than the no TC case, with a reduction of 66.95% and 67.39% in SP and NP, respectively, while the $|\mathbf{E}|$ magnitudes remained practically unchanged. This finding suggests that although the tissue temperature could have a major effect on $|\mathbf{E}|$ through the $\sigma(T)$ dependence, the spatial temperature gradients are too low to induce significant changes in the spatial distribution of σ between both models and hence there was no alteration in the magnitudes of the electric field.

Table 3. Electric field magnitudes (V/m) measured at specific locations (see Fig. 6b) and at the end of the last RF pulse in the case of different timing patterns (pulse duration–pulses repetition frequency) and applied voltages (without temperature controller).

Applied voltage	**45 V**			**55 V**		
Timing pattern	**20 ms–2 Hz**	**8 ms–5 Hz**	**5 ms–5 Hz**	**20 ms–2 Hz**	**8 ms–5 Hz**	**5 ms–5 Hz**
1	4,106	4,210	4,165	5,047	5,015	5,047
2	1,892	1,887	1,837	2,348	2,390	2,318
3	1,080	1,063	1,022	1,366	1,395	1,292
4	656	663	633	861	855	805
5	2,329	2,305	2,237	2,946	2,958	2,807
6	1,018	1,022	979	1,325	1,323	1,242
7	612	605	576	789	801	734
8	413	406	385	532	542	492

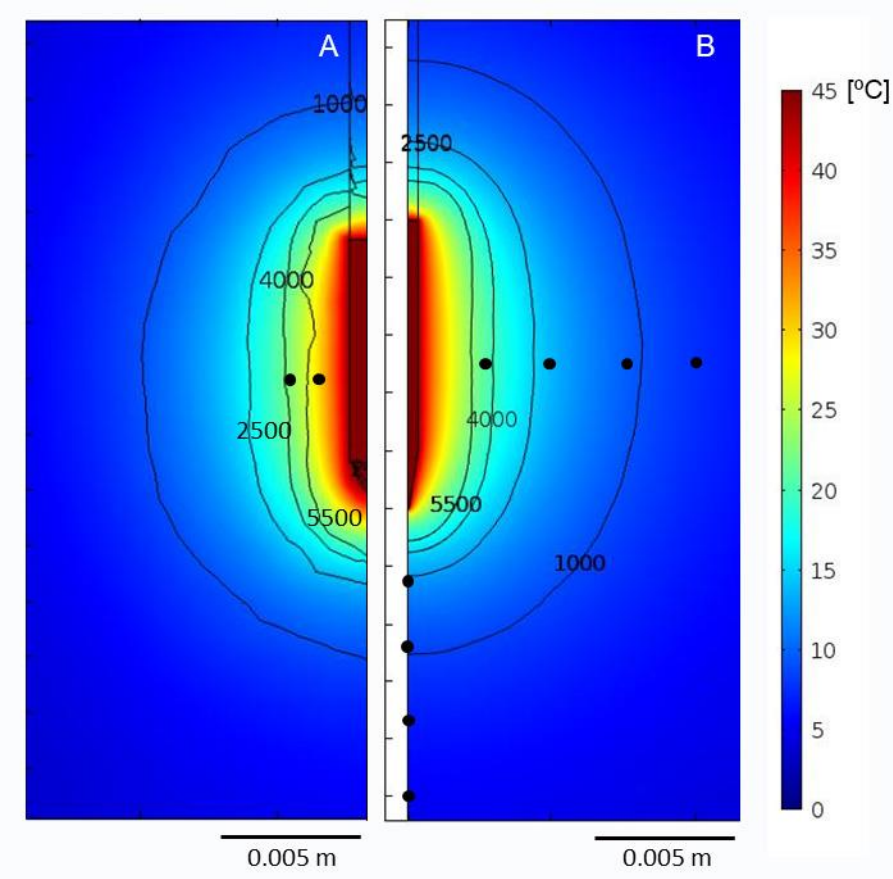

Figure 12. Electrical potential distribution (V) during the last pulse of the 20 ms pulse duration protocol from the computational model based on the in vitro study using an agar phantom (a) and from the modeling study in tissue (45 V-20 ms-2 Hz) (b). Black contour lines represent electric field magnitude (V/m). Black dots are the points of voltage and field measurement from each model.

Regarding the spatial distribution of the electric field, the highest $|\mathbf{E}|$ value for the last pulse was reached at the electrode tip and dropped rapidly with distance from the electrode surface, as was also observed with the temperature distribution. Table 3 shows the maximum values of $|\mathbf{E}|$ at various locations. Neither pulse duration nor repetition frequency had an impact on the $|\mathbf{E}|$ value of the last pulse.

The $|\mathbf{E}|$ value decayed as we moved away from the electrode surface, and this drop was stronger in the direction defined by the electrode axis (as shown in Fig. 12b). For instance, for SP with 45 V, it decayed from 26.4 kV/m (computed at 0.1 mm from the electrode surface) to 4.1 kV/m at P_1, and from 60.9 kV/m (computed at 0.1 mm from the electrode surface) to 2.3 kV/m at P_5.

For distances from the electrode surface (r) of up to 10 mm, the electric field decreased proportionally to 1/r in the direction transverse to the electrode axis and to $1/r^2$ in the direction of the electrode axis.

In the electrical performance in the in vitro experimental study, the voltage values measured at 1 and 2 mm distances at the beginning of the PRF application were very similar to those obtained from the computer model: 29.9 ± 3.2 V vs. 29.5 V, and 24.3 ± 2.4 V vs. 24.3 V, respectively. There was also good agreement between the values at the end of the application: 30.9 ± 3.0 V vs. 30.5 V, and 25.4 ± 2.0 V vs. 25.4 V, respectively. Figure 12b shows the voltage and electric field distributions from the computer model built to validate the experimental results, which are seen to be very similar to those obtained from the model that reproduced the clinical situation (Fig. 12a).

2.5. Discussion

The aim of this study was to compare the performance of two different PRF protocols in terms of the temperature generated and, in particular, the electric field. First of all, we conducted an experimental PRF study on agar phantom in order to guarantee the accuracy of the computer model predictions and validate the modeling methodology. Even though the final temperature value was lower in the experiment than in the simulations, we found both results in reasonable agreement. One of the possible reasons for the measurement interference could have been the effect of the higher than expected heat losses, in addition to the fact that the metal electrode had much lower emissivity than the agar phantom for which the camera had been calibrated.

The thermal impact of PRF on tissue is defined by temperature spike phenomena within a range of independently modified maximum and minimum values that depend on the pulse protocol. As previously demonstrated by Cosman and Cosman [16], shorter pulses entail lower values of the temperature spike magnitude, while higher applied voltage and higher repetition frequency imply the opposite. In practical terms, the results confirmed that the new protocol (55 V–5 ms–5 Hz) has a similar thermal effect

to that obtained with the standard protocol (45 V–20 ms–2 Hz) but with a considerably higher electric field magnitude due to the fact that both protocols provided equivalent total energy during the procedure.

When the temperature controller was included, the total applied pulses were considerably reduced (66.95% and 67.39%). This avoided thermal damage to the tissue (Fig. 9d-9e) even though the maximum temperatures at the electrode tip were close to 50ºC, neither did it have much effect on the electric field magnitude.

In order to optimize PRF protocols it is necessary to maximize what can be defined as the 'electrical dose' while minimizing the thermal effects to avoid thermal injury, although it is no easy task to define this 'electrical dose'. Experimental studies indicate that it cannot be defined as proportional to the delivered electrical energy, because protocols that apply similar heating yield different treatment outcomes [18]. Neither can it be defined as proportional to the product of the electric field magnitude and the active time (pulse duration × frequency) because that would imply that, for protocols of equivalent energy but different fields, the protocol with the highest 'electrical dose' would have the lowest electric field, and experimental results show that this is not the case. As it appears that PRF efficacy strongly depends on the electric field magnitude, the 'electrical dose' should therefore reflect this strong dependence on it. By increasing the applied voltage, the target tissue is exposed to a higher electric field, but this does not necessarily lead to an increase in the delivered energy – or in the thermal effects – if the pulses are shortened and the repetition frequency is reduced.

Since including the temperature controller reduced the total amount of applied pulses by 66.95% and 67.39% for SP and NP, respectively, we could estimate a 'cumulative time' of equivalent continuous electric field application as the sum of the duration of all the pulses actually delivered, which would provide a 'cumulative time' of 4.75 s and 2.93 s for SP and NP, respectively. This difference between the protocols should be taken into account in any future studies that might prove that the 'electrical dose' is somehow related to this 'cumulative time'.

Raising the voltage from 45 V to 55 V caused a proportional rise in the electric field, which at a distance of 2.5 mm increased to over 500 V/m (along the radial axis) and 900 V/m (along the axial axis). As expected, the increase in electric field magnitude was approximately proportional to the increase in the applied voltage (≈ +20%). It can therefore be inferred that this increase in $|\mathbf{E}|$ would have a significant impact on the outcome of the PRF treatment.

Another interesting finding was that the electric field magnitude shows a smaller decrease with distance in the direction transverse to the electrode axis, as compared to the direction parallel to it, which suggests that the 'electrical dose' is also affected by the relative positioning of the electrode with respect to the target nerve. In the regions close to the electrode tip, the electric field magnitude may be large enough to cause cell electroporation. Due to their geometry, when nerve fibers are exposed to an electric field with a direction approximately parallel to their orientation, the induced transmembrane voltage is significantly larger than that experienced by other types of cells [31]. Therefore, the electric field necessary for electroporation to occur in nerve fibers is lower than in other cells. Although monopolar pulses are the most effective in terms of cell electroporation, pulsed AC fields are also known to cause it [32], and bursts of biphasic pulses in the same frequency range as those used in PRF have been shown to ablate tissues by means of irreversible electroporation [33].

Due to the lack of experimental studies in this area, it is not possible to indicate the electric field threshold necessary for the electroporation of nerve fibers to occur when using the typical PRF waveforms, although experiments performed with bursts of bipolar pulses can serve as a reference. The electric field required to cause electroporation through these pulses is about 2.5 times larger than that of conventional monopolar pulses of the same duration [34]. On the other hand, in a study by Abramov et al. [35] electric pulses of 7.5 kV/m caused obvious signs of electroporation and, as a consequence, nerve conduction block, as well as disintegration of the myelin sheath and swelling of the nerve tissue in the rat sciatic nerve. We can therefore hypothesize that severe electroporation will occur in regions exposed to electric fields in the

order of 18 kV/m and above, which, in our study, were only found very close to the electrode tip (distance < 0.5 mm). Nevertheless, it should be noted that this value could have been lower due to the exposure time in PRF treatments being longer than conventional electroporation protocols. Neither can we rule out the occurrence of mild electroporation – which does not damage neurons – for much lower fields.

2.5.1. Limitations of the study

This study has some limitations that should be pointed out. Firstly, the computer model represented a general approach to PRF used in pain treatment, but no specific location (target) for the PRF treatment was considered, i.e. the tissue was considered to be homogeneous. This simplification could introduce inaccuracies in the simulated model since non-homogeneous tissue presents a distorted electric field distribution. Also, instead of modeling different compartments, one material was used in the study whose electrical conductivity value was the result of the conductivities of the adjacent tissues. Secondly, only one specific RF applicator was modeled, regardless of the other sizes habitually employed in PRF clinical practice (diameters ranging from 18 to 22 gauges and lengths from 5 to 10 mm). In spite of these two limitations, we consider the conclusions are still valid since this was a comparative study and the protocols considered were evaluated under identical conditions.

2.6. Conclusions

The recently proposed PRF protocol based on a higher voltage (55 V instead of 45 V), shorter pulses (5 ms instead of 20 ms) and a higher pulse frequency repetition (5 Hz instead of 2 Hz) can increase the electric field magnitude reached in the tissue without raising the temperature as the total time of exposure to RF is considerably reduced. However, what really avoids thermal damage is the use of a temperature controller, which keeps the electric field magnitude at the same level as when this system is absent and reduces the total delivered pulses by around 67%.

References

[1] Protasoni M, Reguzzoni M, Sangiorgi S, et al. Pulsed radiofrequency effects on the lumbar ganglion of the rat dorsal root: A morphological light and transmission electron microscopy study at acute stage. Eur Spine J 2009; 18:473–8.

[2] Vas L, Pai R, Khandagale N, et al. Pulsed radiofrequency of the composite nerve supply to the knee joint as a new technique for relieving osteoarthritic pain: a preliminary report. Pain Physician 2014; 17:493–506.

[3] Vallejo R, Benyamin RM, Kramer J, et al. Pulsed radiofrequency denervation for the treatment of sacroiliac joint syndrome. Pain Med 2006; 7:429–34.

[4] Cohen SP, Van Zundert J. Pulsed Radiofrequency: Rebel Without Case. Reg Anesth Pain Med 2010; 35:8–10.

[5] Brodkey JS, Miyazaki Y, Ervin FR, et al. Reversible Heat Lesions with Radiofrequency Current. A Method of Stereotactic Localization. J Neurosurg 1964; 21:49–53.

[6] Viglianti BL, Dewhirst MW. Thresholds for thermal damage to normal tissues : An update. Int J Hyperth 2011; 27:320–43.

[7] Vatansever D, Tekin I, Tuglu I, et al. A comparison of the neuroablative effects of conventional and pulsed radiofrequency techniques. Clin J Pain 2008; 24:717–24.

[8] Heavner JE, Boswell MV, Racz GB. A comparison of pulsed radiofrequency and continuous radiofrequency on thermocoagulation of egg white in vitro. Pain Physician 2006; 9:135–7.

[9] Hata J, Perret-Karimi D, DeSilva C, et al. Pulsed radiofrequency current in the treatment of pain. Crit Rev Phys Rehabil Med 2011; 23:213–40.

[10] Erdine S, Bilir A, Cosman ER, et al. Ultrastructural changes in axons following exposure to pulsed radiofrequency fields. Pain Pract 2009; 9:407–17.

[11] Choi S, Choi HJ, Cheong Y, et al. Internal-Specific Morphological Analysis of Sciatic Nerve Fibers in a Radiofrequency-Induced Animal Neuropathic Pain Model. PLoS One 2013; 8.

[12] Choi S, Choi HJ, Cheong Y, et al. Inflammatory responses and morphological changes of radiofrequency-induced rat sciatic nerve fibres. Eur J Pain (United Kingdom) 2014; 18:192–203.

[13] Podhajsky RJ, Sekiguchi Y, Kikuchi S, et al. The histologic effects of pulsed and continuous radiofrequency lesions at 42°C to rat dorsal root ganglion and sciatic nerve. Spine (Phila Pa 1976) 2005; 30:1008–13.

[14] Lee J, Byun J, Choi I. The Effect of Pulsed Radiofrequency Applied to the Peripheral Nerve in Chronic Constriction Injury Rat Model. Ann Rehabil Med 2015; 39:667–75.

[15] Van Zundert J, de Louw AJ, Joosten EJ, et al. Pulsed and continuous radiofrequency current adjacent to the cervical dorsal root ganglion of the rat induces late cellular activity in the dorsal horn. Anesthesiology 2005; 102:125–31.

[16] Cosman ER, Cosman ER. Electric and Thermal Field Effects in Tissue Around Radiofrequency Electrodes. Pain Med 2005; 6:405–24.

[17] Sandkühler J, Chen JG, Cheng G, et al. Low-frequency stimulation of afferent Adelta-fibers induces long-term depression at primary afferent synapses with substantia gelatinosa neurons in the rat. J Neurosci 1997; 17:6483–91.

[18] Fang L, Tao W, Jingjing L, et al. Comparison of High-voltage- with Standard-voltage Pulsed Radiofrequency of Gasserian Ganglion in the Treatment of Idiopathic Trigeminal Neuralgia. Pain Pract 2015; 15:595–603.

[19] Rohof OJ. Radiofrequency treatment of peripheral nerves. Pain Pract 2002; 2:257–60.

[20] Rohof OJ. Caudal Epidural of Pulsed Radiofrequency in Post Herpetic Neuralgia (PHN); Report of Three Cases. Anesth Pain Med 2014; 4:10–3.

[21] Vallejo R, Tilley DM, Williams J, et al. Pulsed radiofrequency modulates pain regulatory gene expression along the nociceptive pathway. Pain Physician 2013; 16:E601–13.

[22] Tun K, Cemil B, Gurcay AG, et al. Ultrastructural evaluation of pulsed radiofrequency and conventional radiofrequency lesions in rat sciatic nerve. Surg Neurol 2009; 72:496–500.

[23] Pearce J, Panescu D, Thomsen S. Simulation of diopter changes in radio frequency conductive keratoplasty in the cornea. Model Med Biol 2005; 8:469–77.

[24] Kuster N, Capstick M. IT'IS Foundation for Research on Information Technologies in Society 1999. http://www.itis.ethz.ch/virtual-population/tissue-properties/overview/.

[25] Trujillo M, Castellví Q, Burdío F, et al. Can electroporation previous to radiofrequency hepatic ablation enlarge thermal lesion size? A feasibility study based on theoretical modelling and in vivo experiments. Int J Hyperthermia 2013; 29:211–8.

[26] Birngruber R, Hillenkamp F, Gabel VP. Theoretical investigations of laser thermal retinal injury. Health Phys 1984; 48:781–96.

[27] Fukui S, Rohof OJ. Results of pulsed radiofrequency technique with two laterally placed electrodes in the annulus in patients with chronic lumbar discogenic pain. J Anesth 2012; 26:606–9.

[28] Fukui S, Nitta K, Iwashita N, et al. Intradiscal pulsed radiofrequency for chronic lumbar discogenic low back pain: a one year prospective outcome study using discoblock for diagnosis. Pain Physician 2013; 16:E435–42.

[29] Sluijter ME, Cosman ER, Rittman WB, et al. The effects of pulsed radiofrequency fields applied to the dorsal root ganglion - a preliminary report. Pain Clin 1998; 11:109–17.

[30] Cahana A, Vutskits L, Muller D. Acute differential modulation of synaptic transmission and cell survival during exposure to pulsed and continuous radiofrequency energy. J Pain 2003; 4:197–202.

[31] Lee RC, Dougherty W. Electrical injury: mechanisms, manifestations, and therapy. IEEE Trans Dielectr Electr Insul 2003; 10:810–9.

[32] Chen C, Evans J, Robinson MP, et al. Measurement of the efficiency of cell membrane electroporation using pulsed ac fields. Phys Med Biol 2008; 53:4747–57.

[33] Sano MB, Arena CB, DeWitt MR, et al. In-vitro bipolar nano- and microsecond electro-pulse bursts for irreversible electroporation therapies. Bioelectrochemistry 2014; 100:69–79.

[34] Sweeney DC, Reberšek M, Dermol J, et al. Quantification of cell membrane permeability induced by monopolar and high-frequency bipolar bursts of electrical pulses. Biochim Biophys Acta - Biomembr 2016; 1858:2689–98.

[35] Abramov GS, Bier M, Capelli-Schellpfeffer M, et al. Alteration in sensory nerve function following electrical shock. Burns 1996; 22:602–6.

[36] Tungjitkusolmun S, Staelin ST, Haemmerich D, et al. Three-Dimensional Finite-Element Analyses for Radio-Frequency Hepatic Tumor Ablation. IEEE Trans Biomed Eng 2002; 49:3–9.

[37] Trujillo M, Bon J, Jose Rivera M, et al. Computer modelling of an impedance-controlled pulsing protocol for RF tumour ablation with a cooled electrode. Int J Hyperth 2016; 6736:1–9

Chapter 3

A clinically oriented computer model for radiofrequency ablation of hepatic tissue with internally cooled wet electrode

3.1. Abstract

To improve the computer modelling of radiofrequency ablation (RFA) by internally cooled wet (ICW) electrodes with added clinically oriented features. An improved RFA computer model by ICW electrode included: (1) a realistic spatial distribution of the infused saline, and (2) different domains to distinguish between healthy tissue, saline-infused tumor, and non-infused tumor, under the assumption that infused saline is retained within the tumor boundary. A realistic saline spatial distribution was obtained from an *in vivo* pig liver study. The computer results were analyzed in terms of impedance evolution and coagulation zone (CZ) size, and were compared to the results of clinical trials conducted on 17 patients with the same ICW electrode. The new features added to the model provided computer results that matched well with the clinical results. No roll-offs occurred during the 4-min ablation. CZ transversal diameter (4.10 ± 0.19 cm) was similar to the computed diameter (4.16 cm). Including the tumor and saline infusion in the model involved (1) a reduction of the initial impedance by 10 - 20 Ω, (2) a delay in roll-off of 20 s and 70 - 100 s, respectively, and (3) 18 - 31% and 22 - 36% larger CZ size, respectively. The saline spatial distribution geometry was also seen to affect roll-off delay and CZ size. Using

a three-compartment model and a realistic saline spatial distribution notably improves the match with the outcome of the clinical trials.

3.2. Introduction

Radiofrequency ablation (RFA) is a minimally invasive procedure that destroys tumors by selective heating with radiofrequency (RF) electrical current [1,2]. RF current produces ionic agitation in the tissue next to the electrode, which is trans- formed into heat and propagated in the tissue by thermal conduction [3]. A few seconds after the tissue reaches a temperature over 50ºC, the cell proteins are denatured and the cell dies by coagulative necrosis [4,5]. To guarantee the destruction of tumor cells, RFA must produce a successful coagulation zone (CZ) around the tumor with a 5–10 mm surgical margin recommended for inhibition of local recurrence caused by residual untreated single tumor cells [6]. Although tissue impedance is reduced when heating starts, the dehydration around the electrode due to the liquid-to-vapor phase change causes a sudden rise in electrical impedance (roll-off). This phenomenon seriously limits energy deposition in the tissue and reduces CZ size. Changes in the power delivery protocol and electrode design have been the primary ways of overcoming this limitation.

Internally cooled wet (ICW) electrodes, with combined saline infusion and internal electrode cooling, have arisen as an alternative method of increasing the CZ size obtained separately by cooled electrodes and wet electrodes [7]. The combination of tissue hydration and higher tissue electrical conductivity by infused hypertonic saline, together with the effect of internal cooling, keeps impedance low for longer and may even eliminate roll-off [8–10]. This increases CZ size, and hence the ability to treat larger tumors. Previous experimental and computational results have shown that larger CZs can be obtained by ICW electrodes than by cooled electrodes and wet electrodes separately [11–13], while even larger CZs can be obtained if saline is infused 2 mm from the mid-point of the electrode tip [14]. This “remote” infusion is physically implemented by expandable infusion needles. Unfortunately, saline infusion may involve potential risks, such as uncontrolled saline

migration in tissue (although this is less likely in the case of encapsulated tumors) or irregular CZs [15]. Accidental perforation of the tumor wall by expandable infusion needles could also damage nearby organs by saline leakage or undesirable tumor cell seeding.

Computational modelling can provide a comprehensive and detailed biophysical description of the electrical and thermal performance of ICW electrodes during RFA, and thus can be used to improve their use in clinical practice. However, as far as we know, there is still a gap between the modelling studies in this field and their transfer to clinical practice [8,13,16–18]. Demazumder et al. [16] and Antunes et al. [18] built computational models of wet electrodes for cardiac and hepatic RFA, respectively, while Romero-Méndez et al. [8] compared the electrical and thermal behavior of wet electrodes with ICW electrodes. However, all the phenomena associated with saline infusion have not yet been thoroughly studied. Although Qadri et al. [17] proposed a computational model of ICW electrodes that included saline transport through the tissue, neither the ICW electrode model nor the ablation protocol (10 min-RFA at constant 90ºC by varying input voltage) matched the real conditions of clinical practice.

As an alternative to the formulation proposed by Qadri et al. [17], we recently conducted a study of the influence on CZ size of all the phenomena involved in RFA by ICW electrodes and how they could be included in a computational model [13]. The results showed that the higher electrical conductivity due to saline infusion was mainly responsible for the better performance of ICW electrodes over internally cooled (IC) electrodes, especially as regards CZ size and delaying roll-off. However, this model had two limitations which prevented the computational results being extrapolated to clinical practice: (1) the spatial distribution of infused saline was assumed to be spherical, which does not always actually occur; and (2) the electrical, thermal and perfusion characteristics of healthy and tumor tissue were assumed to be identical, even though electrical conductivity is known to be much higher in tumors than in healthy tissue, and blood perfusion in tumors varies as they grow.

Our aim was thus to improve the previous computational model [13] and set up a clinically oriented model which would include: (1) a more realistic pattern of infused saline distribution at the center of the tumor based on the results of an ad hoc *in vivo* experiment, and (2) three compartments for the different zones of saline-infused tumor, non-infused tumor and healthy tissue. The computer results (CZ size and evolution of impedance) were compared to those obtained from a clinical trial with an ICW electrode with identical characteristics to those of the modelled electrode.

3.3. Materials and methods

3.3.1. *Clinical trial*

A randomized clinical trial comparing RF ablation (with ICW electrode) vs. microwave ablation (European Registry ISRCTN73194360) is currently under way in the *Hospital del Mar* (Barcelona, Spain). In the context of our modelling study, we selected and analyzed only those nodules treated with a single RF ablation from May 2014 to April 2017, which involved 17 patients and a total of 19 nodules measuring 17.9 ± 0.8 mm in major diameter and 14.8 ± 0.8 mm and 12.8 ± 0.7 mm in minor diameters. RFA was performed using an ICW electrode comprised of a single 2.8 mm diameter and 30-mm long internally cooled electrode with two electrically isolated expandable needles (0.65 mm outer diameter) to infuse hypertonic (20% NaCl) saline at 2 mm from the electrode surface [19] (see Figure 13a and 13b). The electrode temperature was kept under 10ºC by cooled saline circulating through the electrode at 100 mL min^{-1}. RF energy was delivered for 4 min by a CC-1 generator (Radionics, Burlington, MA). The impedance control mode used consisted of a 1-min ramp-up phase followed by 3 min at maximum power (~140 W). Power was supplied from the ICW electrode to four dispersive electrodes.

As saline is normally infused during RFA with ICW electrodes, this demands that the optimal volume of injected saline must be used, as an excess can lead to leaks, irregular morphology of the ablated zones (due to hot saline) or seeding of tumor cells carried by the saline [20]. Alternatively, pre-

treatment with a hypertonic saline bolus (instead of continuous infusion) could provide a controlled dose of fluid and hence would reduce the risk of complications. The clinical trial thus employed two boluses of 0.5 mL of saline each infused simultaneously through both expandable needles just before RFA. Two additional boluses were administered for <15 s after 90 s of RFA for additional rehydration of the overheated tissue to prevent any potential rise in tissue impedance. Both impedance and power evolution were recorded throughout the ablation. After the procedure computer tomography scans were used to measure the diameters of the coagulation zones, which were "corrected" by taking the shrinkage phenomenon into account prior to comparing the measurements with the computer results (see 2.3. *Computational model*).

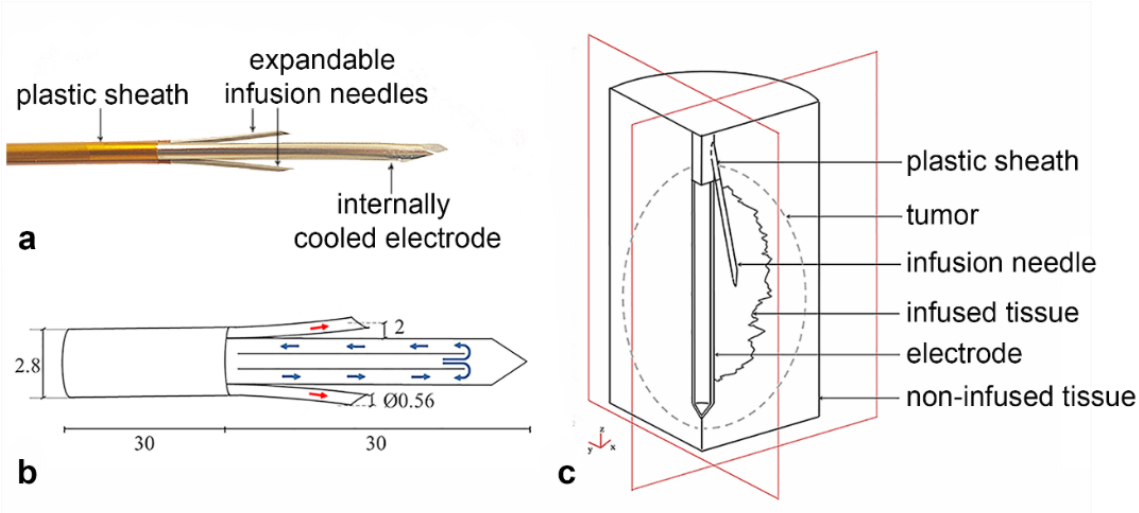

Figure 13. (a) Internally cooled-wet (ICW) electrode used in the clinical trial. (b) Electrode scheme and dimensions (in mm, out of scale). Blue arrows indicate the internal flow of cooling liquid while red arrows show the outflow of hypertonic saline through expandable needles. (c) Geometry of the three-compartment model used in the computational study. Note that the geometry of infused tissue is for illustrative purposes only, i.e. it does not coincide with the contour geometry of saline-infused tissue computed from the "generic pattern" (shown in Figure 14b and 14c, respectively).

3.3.2. *Spatial distribution of infused saline measured by in vivo study*

The spatial distribution of the saline infused into the tissue by the boluses was analyzed by means of an *in vivo* experimental study on two female pigs. The study was approved by the Animal and Human Experimentation Ethics Committee of the *Universitat Autónoma de Barcelona* (protocol numbers CEEAH 3336 and DMAH 8904). Both animals underwent a laparotomy to expose the liver for direct infusion. Iopamidol, a non-ionic contrast agent (G.E.S., Madrid, Spain), was added to the infused saline. The boluses were introduced into different sections of each lobe through the two expandable needles of an ICW electrode identical to that used in the clinical study. Six sets of infusions were made, each consisting of two 0.5 mL boluses injected at 0 s and 90 s, which gives 2 mL total volume injected per set. Each infusion took ~15 s. The spatial distribution of infused saline was mapped by a GE OEC Fluorostar fixed X-ray image intensifier system (GE OEC Medical Systems, Salt Lake City, USA) without applying RF, since the aim was to determine the spatial distribution of the saline bolus just before RFA. The images were first preprocessed with Image J Software (open source available at https://imagej.net), adjusting brightness and contrast in order to reduce noise and enhance image quality. As the images from the first and second infusion of the same set were seen to have an almost identically shaped and sized distribution (see Section 3.4 *Results* for further details), they were overlapped to create a "generic distribution" for each set. The margins of the infused areas were then segmented by thresholding each 8-bit greyscale image [21], preceded by the background subtraction operation for increased effectiveness. The segmented margins were then merged with the original images, converted into binary format and mounted together to create one greyscale image in which each image made up 16.6% of the total greyscale intensity, so that 67% greyscale was considered as the "generic pattern" of saline infusion and hence was used to build the computer model.

3.3.3. *Computational model*

3.3.3.1. *Geometry*

The computational model mimicked an RF hepatic ablation by ICW electrode, as shown in Figure 13a and 13b. The dispersive electrode was modelled as an electrical condition on the boundaries parallel to the active electrode axis. The area of these boundaries coincided with those of four dispersive electrodes (~132 cm^2 each). Figure 13c shows the model geometry, which consisted of five domains with different characteristics: healthy tissue, non-infused tumor, saline-infused tumor, metallic components (electrode, expandable infusion needles) and plastic component (sheath). The outer boundaries of the healthy tissue domain formed a 60-mm radius and 150-mm long cylinder. These dimensions, obtained from a sensitivity analysis, guaranteed an adequate distance between the ICW electrode and the boundary condition (mimicking the dispersive electrodes) to avoid any effects on the simulation results. The reference parameter for the sensitivity analysis was the maximum temperature (T_{max}) reached after 240 s at five points at <1 mm from the ICW electrode. The former dimensions were used in the model for differences in electrode T_{max} of <0.5% between two subsequent simulations. As the three-dimensional geometry presented two symmetry planes (see Figure 13c), the computer model only considered one-quarter of the complete geometry. The tumor dimensions were based on the nodule size reported in the clinical study (see Section 3.3.1 *Clinical trial*). The tumor was assumed to be an ellipse with major axis (axial diameter) of 18.7 mm and with minor axis (transversal diameter) of 15.6 mm. The geometry of the spatial distribution of infused saline matched with the "generic pattern" obtained from the experimental *in vivo* study (see Section 3.3.2. *Saline spatial distribution*) and was centered and enclosed inside the tumor. This correlated with the assumption that saline accumulates inside a tumor with a limited volume due to the surrounding fibrous capsule. Any excess saline injected into a tumor could result in saline reflux and leakage around the infusion needle [20,22,23].

3.3.3.2. *Governing equations and conditions*

The model was based on a coupled electric-thermal problem, which was solved numerically on COMSOL Multiphysics software (COMSOL, Burlington, MA). The governing equation for the thermal problem was the Bioheat equation [24] modified by the enthalpy method to include water vaporization [25]:

$$\frac{\partial(\rho h)}{\partial t} = \nabla \cdot (k\nabla T) + q + Q_p + Q_m \qquad (1)$$

where q is tissue density, h enthalpy, T temperature, t time, k thermal conductivity, q heat source produced by RF power, Q_p heat loss by blood perfusion and Q_m the metabolic heat generation. Q_m was not considered since it is negligible in RFA. No convection term associated with saline motion was considered since its effect is negligible [13].

The heat source produced by RF power (Joule losses) was given by $q=\sigma|\boldsymbol{E}|^2$, where $\boldsymbol{E}$ is the electric field. $\boldsymbol{E} = -\nabla V$ was obtained from the governing equation of the electrical problem $\nabla\cdot(\sigma(T)\nabla V)=0$, σ being the electrical conductivity and V the voltage. The electrical conductivity of the tissues was assumed to be a temperature-dependent piecewise function: an exponential increase by +1.5%/ºC up to 99ºC, the value was kept constant between 99 and 100ºC, then reduced two orders for five degrees, and remained constant for temperatures above 105ºC. The value of σ was specified for all the tissue subdomains considered at a reference temperature (see *Tissue characteristics* subsection). We used a quasi-static approach as it is known that the resistive current at RF (≈500 kHz) is much lower than the displacement current [26].

The blood perfusion term Q_p was obtained from:

$$Q_p = \beta\rho_b c_b \omega_b (T_b - T) \qquad (2)$$

where ω_b is the blood perfusion coefficient, ρ_b and c_b are the blood density and specific heat, respectively, T_b is the temperature of the arterial blood (37ºC) and β is a coefficient that modifies blood perfusion with tissue damage. The thermal damage was assessed by the Arrhenius damage model [27], which

associates temperature with exposure time by a first-order kinetics relationship:

$$\Omega(t) = \int_0^t A e^{-\frac{\Delta E}{RT}} ds \tag{3}$$

where Ω is the damage function, R is the universal gas constant, A is a frequency factor and ΔE is the activation energy for the irreversible damage reaction. The value of $\Omega = 4.6$ corresponding to a 99% probability of cell death [28] was used to define the coagulation zone. Accordingly, blood perfusion rate was defined as follows: $\beta = 0$ for $\Omega \geq 4.6$, and $\beta = 1$ for $\Omega < 4.6$.

Considering tissue hydration due to saline infusion and vaporization at temperatures above 100ºC, the first term in Equation (1) can be expressed in biological tissues as [13,25]:

$$\frac{\partial(\rho h)}{\partial t} = \frac{\partial T}{\partial t} \cdot \begin{cases} \rho_l c_l & 0 < T \leq 99^{\circ}C \\ F h_{fg} C & 99 < T \leq 100^{\circ}C \\ \rho_g c_g & T > 100^{\circ}C \end{cases} \tag{4}$$

where q and c are tissue density and specific heat respectively at temperatures of 100ºC (i=l refers to water in liquid phase) and above (i=g refers to water in gas phase), and h_{fg} is the product of water latent heat and water density at 100ºC, C is tissue water content, and F is a factor previously proposed by the authors which expresses the requirement for more energy at the phase change when considering saline infusion, in addition to the water already contained in the tissue [13].

The thermal boundary conditions were: initial tissue temperature and temperature at all the outer boundaries of 37ºC, and null heat flux on the two symmetry planes. The cooling effect of the liquid circulating inside the electrode was modelled using a thermal convection coefficient h with a value of 2,800 W K^{-1} m^{-2} and a coolant temperature of 10ºC. The value of h was calculated for a flow rate of 100 mL min^{-1} through an area estimated as half of the internal area of the active electrode (see Figure 13b). Electrical boundary conditions were: no current flow in the symmetry planes and on the top and bottom liver boundaries, and voltage set to zero on the remaining

boundary to model the dispersive electrode. Power application mimicked the clinical protocol as far as possible: the voltage of the ICW electrode was linearly increased from 0 to 74 V during the first 60 s and was then kept constant for the remaining 3 min, which corresponded with ~140 W power.

3.3.3.3. *Solver*

The model mesh size was predefined by COMSOL at 9.38 mm, although additional refinement with 0.6 mm element size was used next to the ICW electrode, where the maximal electric and thermal gradients occur. The sensitivity study (as previously described for model dimensions) was performed on mesh size to find an adequate spatial discretization and minimize its effect on the numerical solution. An adaptively changing time step was used. Again, we assessed the time-step suitability by an analogous sensitivity analysis.

3.3.3.4. *Tissue characteristics*

Table 4 shows the parameter values used in the model [29–41]. Healthy liver electrical conductivity (σ) was set to 0.2 S m^{-1} at a reference temperature of 37°C, within the range of values reported in the literature: 0.132 S m^{-1} [29], 0.143 S m^{-1} [30] and 0.260 S m^{-1} [42]. Although a tumor electrical conductivity value of 0.5 S m^{-1} had been used previously [20,30,31,42,43], 0.45 S m^{-1} was chosen so that the computed initial impedance evolution matched the values found in the clinical trials (Section 3.4.1 *Clinical trial*).

Saline-infused tumor was characterized by higher electrical conductivity due to the increased concentration of ions in the saline, which carry the electric charge. According to Goldberg et al. [23], tissue "doped" with 18% hypertonic saline showed almost half the impedance measured before the injection (~110 Ω before and ~64 Ω after). This can only be due to higher electrical conductivity, and so the electrical conductivity was twice that of non-infused tissue: 0.4 S m^{-1} for saline-infused healthy liver and 0.9 S m^{-1} for saline-infused tumor. This assumption led to lower initial tissue impedance and matched the clinical values (see Section 3.4.1 *Clinical trial*).

Table 4. Characteristics of the materials used in the computational model (ref. in brackets).

		Plastic	Metal	Healthy liver	Non-infused tumor	Saline-infused tumor
Electrical conductivity (S/m)		10^{-5} [34]	$7.4 \cdot 10^{6}$ [35]	0.2	0.45	0.9
Thermal conductivity (W/m·K)		0.026 [35]	15 [35]	0.502 [36]	0.5 [32]	0.5 [32]
Density (kg/m^3)	LP	70 [35]	$8 \cdot 10^{3}$ [35]	1080 [29]	1045[31]	1045 [31]
	GP			370 [29]	370 [29]	370 [29]
Specific heat (J/kg·K)	LP	1045 [35]	480 [35]	3455 [29]	3760 [31]	3760 [31]
	GP			2156 [29]	2156 [29]	2156 [29]
Water content (%)				68 [37]	84 [38, 39]	84 [38, 39]
Frequency factor (s^{-1})				$7.39 \cdot 10^{39}$ [40]	$5.316 \cdot 10^{50}$ [41]	$5.316 \cdot 10^{50}$ [41]
Activation energy (J/mol)				$2.577 \cdot 10^{5}$ [40]	$3.238 \cdot 10^{5}$ [41]	$3.238 \cdot 10^{5}$ [41]
Blood perfusion (s^{-1})				0.016 [30]	0.009 [30, 33]	0.009 [30, 33]

Electrical conductivity of tissue was measured at 37°C; LP: water in liquid phase; GP: water in gas phase.

Values of tumor density (ρ) and specific heat (c) when its water content is in the liquid phase (T < 100°C) were taken from [29] and [31]. However, as to our knowledge there are no references for the value of tumor density and specific heat when its water content is in the gas phase in Equation (4), we assumed the same values as liver, due to their similarity in this state and their slight influence on the results [44].

As tumor blood perfusion coefficient (ω_b) has been reported within a wide range of values: 0.0027 s^{-1} [32], 0.0053 s^{-1} [43], 0.0069 s^{-1} [45], 0.0096 s^{-1} [33], 0.011 s^{-1} (63.8 mL/100g min^{-1}, [46]) and 0.009 s^{-1} (510 mL kg^{-1} min^{-1}, [30]), we chose a value of 0.009 s^{-1} as it was the reference we used for healthy tissue

and agreed with Aramburu et al. [45], who suggested that perfusion in healthy tissue is different from that of tumor tissue. While healthy tissue is supplied through the portal vein and hepatic artery, a tumor is exclusively supplied from the hepatic artery, which could mean the blood perfusion rate is higher in healthy tissue than in the tumor. We therefore used a value of 0.016 s^{-1} for healthy tissue, which has also been also reported in the literature [30]. According to Hall et al. [44] the perfusion coefficient has a strong impact on the model results, so we decided to conduct a sensitivity analysis of ω_b values for tumor (Case F) ranging from 0.0027 s^{-1} to 0.011 s^{-1}.

Factor F in Equation (4) was set to 1 for both non-infused liver and tumor. For the saline-infused tumor we used a value of $F = 3$ obtained by a sensitivity analysis, as suggested in [13], which related the given value with the process of tissue hydration. F was an adjusting parameter for energy at the phase change during water evaporation when considering saline infusion, as it is assumed that additional tissue hydration increases the tissue's heat capacity. As the only references for characterizing saline-infused tumor, deal with its electrical conductivity, we used the same material characteristics as for non-infused tumor.

3.3.3.5. *Cases analyzed*

The aim of this study was to improve a previously proposed computational model [13] by including two clinically oriented characteristics: (1) a more realistic spatial distribution of infused saline, and (2) new geometry with three separate compartments for healthy liver, non-infused tumor and saline-infused tumor. To assess the influence of these two characteristics on the results, the following five cases were solved and their results compared:

- Case A: One-compartment model considering only non-infused healthy tissue (for an IC electrode).
- Case B: Two-compartment model consisting of non-infused and infused zones of healthy tissue, assuming spatial distribution to be spherical [13].
- Case C: Two-compartment model as in B but using the "generic pattern" of saline distribution obtained from the *in vivo* experiments.

- Case D: Two-compartment model consisting of non-infused healthy liver and tumor tissue.
- Case E: Three-compartment model consisting of healthy tissue, non-infused and infused tumor with the spherical saline distribution as in Case B.
- Case F: Three-compartment (full) model consisting of healthy tissue, non-infused tumor and infused tumor with the "generic pattern" of saline infusion obtained from the *in vivo* experiments.

3.3.3.6. *Outcomes*

Impedance evolution throughout ablation was analyzed for each case, as was transverse CZ diameter at roll-off or otherwise at 240 s. The CZ computed by the Arrhenius damage model at 4 min produced a "very noisy" contour. According to Schutt et al. [28], when computing the lesion dimension contour, the 48–50ºC isotherm correlates with the D99 thermal damage contour, which corresponds to $\Omega = 4.6$ (99% probability of cell death) after a 12 min protocol. In the present study we verified that after 4 min of ablation the 50ºC isotherm matched with $\Omega = 4.6$ (with variations <2 mm) but the isotherm traced a more regular line, so that the 50ºC isotherm was used to measure CZ diameter. Obviously, the use of the isotherm impedes computing the thermal damage accumulated during the cooling phase (just after RF power is switched off), although it is known that the difference in CZ size before and after the cooling phase is negligible in long ablations [47]. Because of the shrinkage associated with RFA, CZ size as measured in clinical practice could be up to 12–20% smaller [48,49]. According to Schutt et al. [28] and Rossmann et al. [48], it is preferable to compare computational results with those obtained in the clinical trials before shrinkage. We therefore established a 20% bigger CZ size margin than the clinical trial when comparing the computer model results.

3.4. Results

3.4.1. *Clinical trial*

A maximum output power (140 W) was applied to the tissue after a 1 min ramp-up, which implied ~30 kJ of total energy deposited. The initial impedance value was ~55 Ω, and dropped to a value of 46 ± 6 Ω just after saline infusion and kept more or less constant throughout the ablation (plateau phase). No roll-off was registered in the whole period. The measured CZ diameters were 3.42 ± 0.16 cm and 2.81 ± 0.16 cm (maximum and minimum transverse diameters, respectively) and 4.71 ± 0.19 cm (axial diameter). After discarding the shrinkage effect and considering 20% larger diameters, these values were: 4.10 ± 0.19 cm and 3.37 ± 0.19 cm (maximum and minimum transverse diameters, respectively) and 5.65 ± 0.23 cm (axial diameter).

3.4.2. *Saline spatial distribution*

The six sets of infusions gave a total of 12 saline distributions (one per each infusion needle). In most cases (10/12), during the injection of the first bolus, X-ray images showed the saline gradually occupying the space around the needle outlet, until a volume of infused tissue was formed. After the injection, the intensity of the contrast agent associated with the saline presence was seen to drop steadily for 90 s, but did not completely disappear. The shape of the infused volume remained unchanged during this period. During the administration of the second bolus, the intensity was gradually restored and the shape contour expanded slightly, after which the intensity and shape evolution were similar to those of the first injection.

In a few cases (2/12) the X-ray images showed that the infused saline escaped through preferential paths and could not accumulate around the infusion needle. These paths corresponded with nearby vessels, whose presence significantly weakened the intensity associated with the contrast agent. As the same procedure occurred after the second bolus both cases were discarded in the analysis.

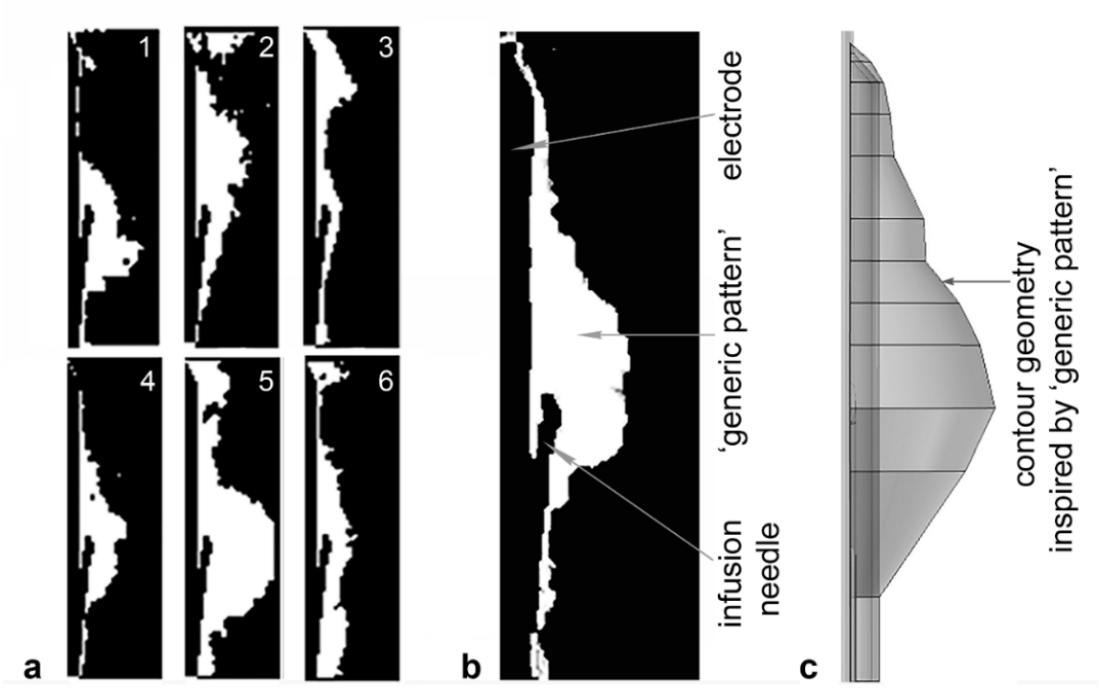

Figure 14. (a) Images of saline spatial distribution from the six saline injection trials (1 – 6) conducted on the *in vivo* model. Saline presence is shown in white, while electrode, infusion needles and non-infused tissue are in black. (b) "Generic pattern" of saline spatial distribution derived from the six images from (a) by thresholding and merging them into one greyscale image. (c) Contour geometry of saline-infused tissue derived from the "generic pattern" in (d) and used in the computer model.

In the remainder (10/12) the saline distribution was irregular and mostly accumulated close to the expandable needle outlet. Figure 14a shows the overlapped images of saline distribution obtained from the six sets of saline injections used to obtain the "generic pattern" shown in Figure 14b.

The contour geometry used in the computer model was derived from this "generic pattern" and revolved symmetrically to the rotation axis (Figure 14c). The total volume of saline estimated from the computer model was close to the total volume injected during each *in vivo* experiment (1.62 and 2 mL, respectively). This volume was used to estimate the radius of the saline spherical distribution considered in Cases B and E.

3.4.3. *Computational results*

3.4.3.1. *Impedance evolution*

Figure 15 shows the impedance evolution for each analyzed case. Roll-off was earlier in cases without saline infusion (A and D), while the addition of saline involved a delay of around 70-100 s (B and C). Roll-off occurred earlier in Case B, with spherical distribution, even though both cases considered the same saline volume. Although including the tumor involved a delay in roll-off (see case A vs. D), its effect was not as marked as saline infusion. In contrast, no roll-offs occurred when both saline infusion and tumor were included (E and F).

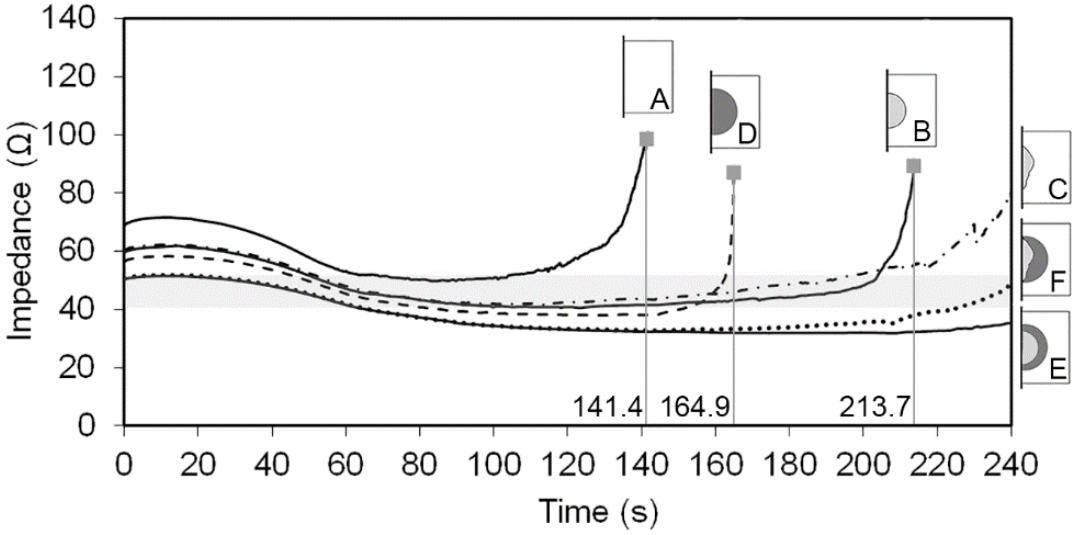

Figure 15. Impedance evolution in the six analyzed cases: A (one-compartment model, only liver), B (two-compartment model, with liver and saline-infused liver using the saline distribution with spherical geometry as proposed in [13]), C (two-compartment model, with healthy liver and saline-infused healthy liver using the saline spatial distribution obtained from the *in vivo* experiment), D (two-compartment model, with non-infused healthy liver and tumor), E (three- compartment model, with healthy liver, tumor with non-infused and saline-infused zones, and spherical geometry infusion) and F (three-compartment model, with healthy liver, tumor with non-infused and saline-infused zones, and saline spatial distribution obtained from the *in vivo* experiment). The horizontal grey band represents the range of impedance values observed in the clinical trial. Roll-off time is shown for cases A, B and D.

Comparing the cases with and without saline infusion (B, C, E and F vs. A and D), infusion was seen to reduce the initial impedance from 69 Ω to 60 Ω in the cases considering only healthy tissue (A vs. B and C) and from 56 Ω to 50 Ω in the cases including the tumor (D vs. E and F). In other words, saline infusion reduced the initial impedance by ~10-13%. Comparing the cases with and without the tumor (A, B and C vs. D, E and F), when the tumor was included the initial impedance was reduced from 69 to 56 Ω for non-infused tissue (A vs. D) and from 60 to 51 Ω for saline-infused tissue (C vs. E and F), showing that the presence of the tumor reduced initial impedance by 15–18%.

Because of the delay in roll-off, the cases that considered both saline infusion and tumor (E and F) had the longest plateau phase, with impedance values more or less constant and within 32 - 50 Ω, and even up to the end of ablation in Case E. Interestingly, the case with the saline distribution based in the "generic pattern" (F) showed values closer to those observed in the clinical trials.

3.4.3.2. *Joule heat source distribution*

Figure 16 shows the comparison of the Joule heat source distributions in cases A–F at the beginning of ablation, at 1 s.

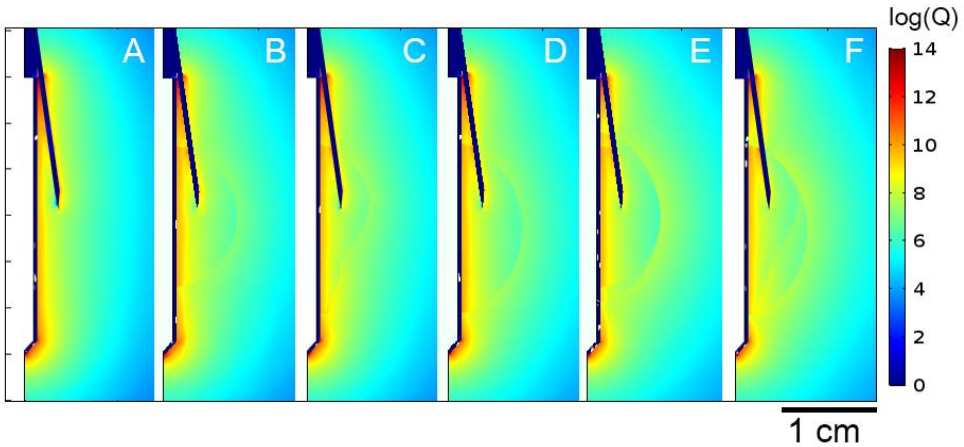

Figure 16. Joule heat distribution in the tissue for cases A–F at 1 s of ablation, (logarithmic scale in W/m^3). Note that maximum values are reached only on the electrode surface and the infusion needles.

As expected, the highest Joule heating concentration was seen in close proximity to the electrode and reached its maximum at both ends of its active part. Although the metal infusion needles were not part of the active electrode (since they are not electrically connected to it), there was a noticeable accumulation of power distribution along their length. Higher power intensity (values ~10^9 W m^{-3}) was also observed in Cases B–F along the boundaries of the tumor and saline domains, although it was slightly lower within these domains (~10^7 W m^{-3}).

3.4.3.3. *Coagulation zone size*

Figure 17a shows the temperature distributions, CZ contour (assessed by the 50ºC isotherm), 100ºC isotherm, and the values of transversal CZ diameter for the six analyzed cases.

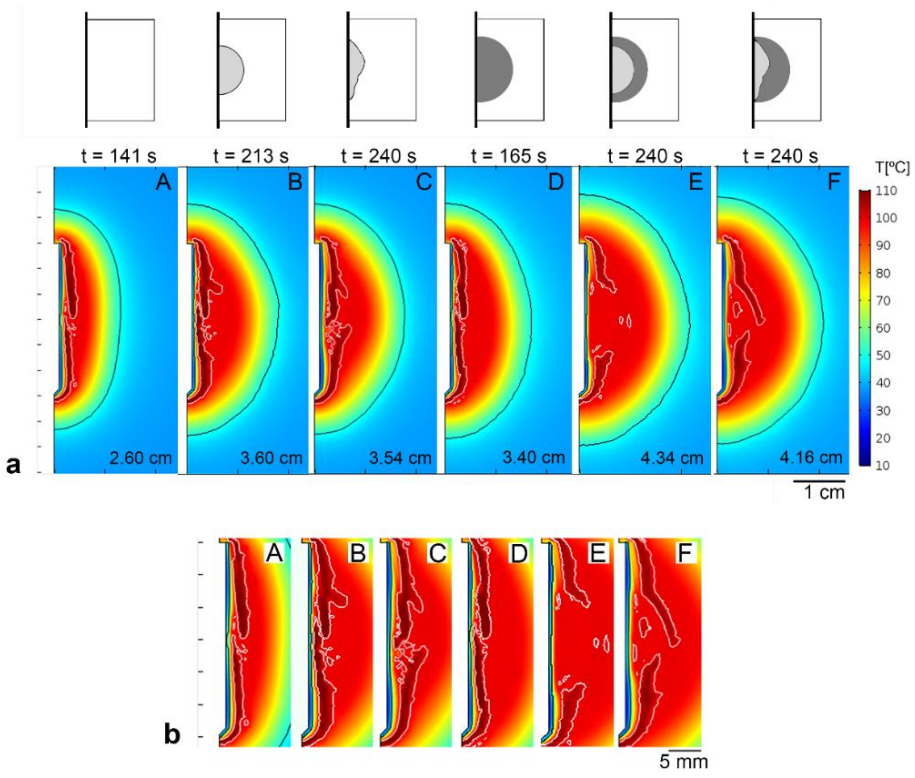

Figure 17. (a) Temperature profiles of cases A–E. Black and white contours are 50ºC and 100ºC isotherms, respectively. The transversal diameter value and time of acquisition are shown in all cases at roll-off times before 240 s or at 240 s in the absence of roll-off. (b) Detail of electrode zone in (a) with 100ºC white isotherm shown.

The largest transversal CZ diameters were observed when saline infusion was considered. The diameter increased from 2.60 cm to 3.54 - 3.60 cm in healthy tissue (A vs. C and B, respectively) and from 3.40 cm to 4.16 - 4.34 cm in the tumor (D vs. F and E, respectively). Although all the cases showed a similar CZ shape, saline infusion increased the transversal CZ diameter by 37% in healthy tissue and 25% in tumor tissue.

Including the tumor as a single factor also increased the transversal CZ diameter by 31% in non-infused tissue (A vs. D) and 18 - 20% in saline-infused tissue (B vs. E and C vs. F). Interestingly, the results showed that including either saline infusion (B and C) or tumor (Case D) produced a similar increase in the transversal CZ diameter. As a logical consequence, the largest transversal CZ diameter was obtained when both characteristics (saline infusion and tumor) were considered together (E and F).

3.4.3.4. *Effect of tumor blood perfusion*

The analysis of the effect of different tumor blood perfusion values (ω_b) on the three-compartment model (Case F) showed that in 240 s of ablation roll-off appeared only when the ω_b value was the lowest of the chosen range (0.0027 s^{-1}). For higher blood perfusion values used it was assumed that roll-off would occur after 240 s and would depend on the ω_b value. CZ growth during the 240 s ablation in all the models was practically unchanged for different ω_b values (differences <1%), showing that increasing the ω_b value did not directly increase CZ size but could delay roll-off.

3.4.4. *Comparison of clinical and computer results*

Figure 18 shows the transversal CZ diameters obtained from the computer results and clinical trials. The colored band represents a range between a minimum value which considers the tissue shrinkage effect and a minimum value that does not, or the probable range in which the results of the computer model (which did not consider the shrinkage effect during ablation) could be compared to the results of the clinical trials.

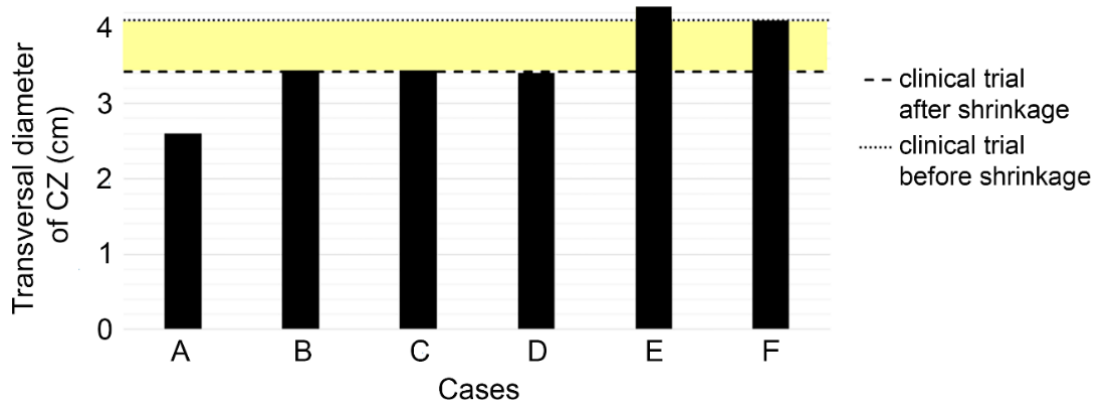

Figure 18. Transversal diameters of the coagulation zones computed for the considered cases A–F. Horizontal lines are the mean transversal diameter found in the clinical trials (dashed line) and the "corrected value" by taking the shrinkage effect into account (dotted line). The colored band thus represents the range in which the clinical and computed results would match.

It can be seen that only the cases that included both saline infusion and the tumor (E and F) predicted a higher transversal diameter than the minimum value. Only Case F was strictly within the diameter range and therefore the only case with similar results to those of the clinical trials.

3.5. Discussion

This study was designed to go a step further in RFA computer modelling by ICW electrode. The desired improvement was to be obtained by including two clinically oriented characteristics: a more realistic geometry of the infused saline spatial distribution and assigning specific characteristics to infused and non-infused tumor zones.

First of all, an *in vivo* study was performed on healthy porcine liver to determine saline spatial distribution after a bolus injection. Two results were obtained, possibly depending on the tissue morphology around the infusion point. First, when the infusion point was at a certain distance from a vessel, the parenchyma retained a certain amount of saline around that point, at least at the infusion rate employed here (1 mL for 15 s). The space occupied probably depended on the bolus volume. The gradual decrease in image intensity indicates that there is a slow loss of accumulated volume, which

suggests that the tissue morphology allows the saline to migrate away, possibly through central veins. This suggests that some saline is still present prior to the second bolus and it is hence reasonable to assume that just after the second injection there will be between 1 and 2 mL of saline around the needle. For this reason, the estimated 1.62 mL of total volume of infused saline in the computer model can be said to be consistent.

Second, when the infusion point was near a vessel the results suggested that the vessel acted as a preferential saline drainage path. Under these conditions, no saline would be retained around the infusion point and the tissue would not be rehydrated during RFA.

The "generic pattern" used to build the computer model geometry was based in the most probable scenario, i.e. that allowing saline to accumulate around the infusion point. In fact, although the saline distributions indicated dispersion between the injections, the "generic pattern" matched 67% of the observed cases, showing irregular borders around the electrode and infusion needles, possibly due to heterogeneous permeability caused by the presence of branching networks of blood and lymphatic vessels [50].

The thin laceration gap during electrode insertion between the tissue and metal components (infusion needles and electrode) could also form an additional preferential saline drainage path. However, this behavior was not found during the study, nor did we find any previous publications reporting this issue. This phenomenon was therefore discarded in the model. The *in vivo* study thus suggests that saline mainly accumulates around the needle outlets in an oval-like geometry with the largest diameter in the direction of the electrode axis. Because it is reasonable to assume that saline distribution during RFA would be different in the presence of a tumor (see *Limitations*), the "generic pattern" employed to build the geometry of the computer model should be considered an approximation.

The computer results showed that modifying the simplest model (Case A) to include a second compartment (tumor or infused zone) reduced the initial impedance. This can be explained by the electrical conductivity of both saline and tumor being higher than non-infused healthy tissue. This also meant that

for the same RFA protocol the initially applied power in Cases B, C and D was ~20 W higher than A, which could have been responsible for the larger CZ in those cases. However, the authors consider that the most important factor in CZ growth is the delay in roll-off: ~23.5 s when the tumor is included (D vs. A) and up to 72.3 and 98.6 s when an infused tissue zone is considered (B and C vs. A). The larger CZ size due to only including the tumor in the model has already been reported by Ahmed et al. [32], although in the present study the greatest effect was related to saline infusion, and hence to tissue hydration, by including factor F in the mathematical framework. This factor is simply an adjusting parameter which allows an energy increase to be considered at the phase change in response to additional tissue hydration by saline infusion, which increases the tissue's heat capacity. This, in addition to the increase of electrical conductivity, explains the long roll-off delays. Two-compartment models thus predict larger CZs than models based exclusively on healthy tissue.

One of the innovations of this study was to include a specific geometry for the infused saline zone based on the results of an *in vivo* study. Despite the limitations involved, we considered this to be the most plausible representation of the spatial distribution of saline in the tissue. As compared to a spherical distribution [13], the geometry derived from the "generic pattern" (Case C) extended roll-off time by 26 s. Because both geometries involved the same total saline volume, the delay could be explained by the particular geometry of case C, which tends to completely surround the electrode, extending toward the ends in an elongated shape, in contrast to the spherical geometry in Case B. The electrode ends (tip and proximal edge) are associated with the hot points around the electrode and if covered by saline affect the temperature distribution around the electrode, including the 100ºC isotherm ring closure that precedes roll-off. This geometry is also probably responsible for the CZ diameter being 0.06 cm smaller than the spherical geometry, as its radial distance was slightly smaller than the spherical radius. This difference was higher (0.18 cm) when both geometries were compared in the models that included a tumor (E and F).

Additional observation of the Joule heat source distribution showed that the metal infusion needle could act as a passive electrode by focusing the electrical current and hence "build" a radius of a greater power deposition than would be the case with only the active electrode working. This could therefore affect the current distribution in tissue and the volume of the power deposition by the Joule effect. The temperature profile and the CZ size could therefore be increased by this factor. Also, a higher power intensity seen at the borders of the tumor and saline domains would suggest that the power deposition occurs faster at the borders than within the domain but since this difference does not correlate with the corresponding temperature distribution this hypothesis is discarded. Thus, the most likely reason would be the boundary effect produced between two neighboring domains with different electrical properties (see cases A vs. B–D and B–D vs. E–F).

Apart from the small differences between cases E and F, the general conclusion is that the three-compartment models offered the most similar results to those of the clinical trial in terms of impedance evolution (see Figure 15) and CZ diameters (see Figure 18).

3.5.1. *Limitations of the study*

Because the *in vivo* study did not consider application of RF power nor tumor tissue we cannot be certain of the saline distribution in these circumstances. However, it is generally accepted that a tumor has an unorganized, disfigured and leaky vessel network with insufficient blood supply, so that its vessel system seems unlikely to be a preferential path of saline drainage [51]. The authors consider that saline would tend to accumulate in the tumor, or at least there would be no significant mechanisms to drain saline away from the tumor, which would justify the assumption of static saline distribution in the model. This is in line with the observations during the clinical trials on actual cases of hepatic tumors, in which no roll-offs occurred after the bolus injections, unlike RFA with saline infusion on healthy tissue.

We recognize that RF-induced heating could affect tissue properties and modify saline distribution. First of all, protein denaturation is known to

increase tissue permeability in the ablated region, but this may not be the case further away from the electrode. This would imply saline migration to more permeable regions. However, the denatured tissue surrounding the electrode would shrink, allowing saline retained at the more permeable zone to move closer to the electrode. There is also a possibility that the nearby blood vessels would narrow or close completely due to the high temperature and eliminate this preferential saline path. In other words, during RFA the saline distribution could change due to vaporization but would remain in the area of infusion as there would be no paths for the saline to drain.

The computer model did not consider the possible additional thermal damage associated with vapor migration after the boiling of interstitial liquids, which can affect CZ size [52]. The increased vapor volume means that in order to stay in thermodynamic equilibrium it needs to expand to maintain the same interstitial pressure, as otherwise, if the volume is constrained, the pressure would increase and the saline could move away from this region. In any case, hot saline transport or vapor migration could engender substantial damage in the surrounding tissue [52] and consequently would modify the CZ size. This phenomenon has been reported to be important in cases with high energy delivery (>100 kJ) for a long period (>30 min) [52]. Because in our case the delivered energy was ~30 kJ, we consider that the pressure level was not high enough to cause significant saline or vapor migration.

It is also important to point out that the factor F used in this study did not really model the specific phenomena triggered by tissue hydration, such as the higher tissue heat capacity, the latent heat throughout ablation and therefore the longer energy release during the phase change. In this light, its use has no physical explanation. Instead, it was included simply as an adjusting parameter whose value was obtained in a previous study by means of sensitivity analysis, in response to the greater energy requirement when considering saline infusion [13]. The phase change due to water vaporization could also be modelled using the apparent heat capacity method, which defines the increased heat capacity over a transition phase as a function of temperature. This would describe the evaporation mechanism more precisely

and would be more suitable for modelling vaporization with this type of electrode. On the other hand, neither the enthalpy method nor the apparent heat capacity method includes the effect of vapor heat migration, since they assume it to be small. Our approach simplifies the model by simply adjusting the value of the energy at the phase change at 99ºC instead of defining the transitory state. Neither does it increase the computational requirements, as in the apparent heat capacity method that uses smaller time step and greater mesh refinement.

With regard to the model, the axial symmetry could be a limitation as it involved using the same value for both transversal diameters of the modelled tumor. Although real tumor nodules present three different axis diameters, the results are still valid since we used the same diameter for both modelling the tumor and assessing the CZ diameter.

3.6. Conclusions

Our experimental findings suggest that the saline spatial distribution in healthy tissue is not necessarily spherical. In fact, saline tends to cumulate around the outlets of the infusion needles, forming an oval-like geometry with the largest diameter in the direction of the electrode axis. The computer modelling study suggests that the inclusion of a second compartment (tumor or infused saline) involves a reduction of the initial impedance and larger coagulation zone size than a one-compartment model based on healthy tissue. The only results similar to the clinical trials were obtained from the three-compartment models (including healthy liver, tumor with non-infused and saline-infused zones) in terms of impedance evolution and CZ diameters. Adding these two features could thus help to develop a more precise and clinically oriented computer model.

References

[1] Savoie P, Lopez L, Simonin O, et al. Two-years follow-up of radio- frequency thermotherapy for urination disorders due to benign prostatic hyperplasia. Prog Urol. 2009; 19:501–506.

[2] Benoist S, Nordlinger B. Radiofrequency ablation in liver tumors. Ann Oncol. 2004; 15:313–317.

[3] Berjano E, Romero-Méndez R, Franco W. Radiofrequency based hyperthermia therapy: a centennial technique serving modern surgery. Rev Mex Ing Biom'ed. 2010; 31:142–153.

[4] Viglianti BL, Dewhirst MW, Abraham JP, et al. Rationalization of thermal injury quantification methods: application to skin burns. Burns. 2014; 40:896–902.

[5] Dewhirst MW, Abraham JP, Viglianti BL. Evolution of thermal dosimetry for application of hyperthermia treatment to cancer. Adv Heat Transfer. 2015; 47:397–421.

[6] Shafirstein G, Novak P, Moros E, et al. Conductive interstitial thermal therapy device for surgical margin ablation: in vivo verification of a theoretical model. Int J Hyperth. 2007; 23:477–492.

[7] Mulier S, Miao YI, Mulier P, et al. Electrodes and multiple electrode systems for radio frequency ablation: a proposal for updated terminology. Adv Exp Med Biol. 2006; 574:57–73.

[8] Romero-Méndez R, Tobajas P, Burdío F, et al. Electrical-thermal performance of a cooled RF applicator for hepatic ablation with additional distant infusion of hypertonic saline: in vivo study and preliminary computer modeling. Int J Hyperth. 2012; 28:653–662.

[9] Lee JM, Han JK, Kim SH, et al. Wet radio-frequency ablation using multiple electrodes: comparative study of bipolar versus monopolar modes in the bovine liver. Eur J Radiol. 2005; 54:408–417.

[10] Jun M, K. inventor. Electrode for radiofrequency tissue ablation. United States patent US 20060122593, 2006.

[11] Cha J, Choi D, Woo M, et al. Radiofrequency ablation zones in ex vivo bovine and in vivo porcine livers: comparison of the use of internally cooled electrodes and internally cooled wet electrodes. Cardiovasc Intervent Radiol. 2009; 32:1235–1240.

[12] Kim JW, Kim JH, Shin YM, et al. Percutaneous radiofrequency ablation with internally cooled wet electrodes versus cluster electrodes for the treatment of single medium-sized hepatocellular carcinoma. Gastrointest Interv. 2014; 3:98–103.

[13] Trujillo M, Bon J, Berjano E. Computational modeling of internally cooled wet (ICW) electrodes for radiofrequency ablation: impact of rehydration, thermal convection and electrical conductivity. Int J Hyperth. 2017; 33:624–634.

[14] Burdío F, Berjano E, Navarro A, et al. RF tumor ablation with internally cooled electrodes and saline infusion: what is the optimal location of the saline infusion? Biomed Eng Online. 2007; 6:30.

[15] Gillams AR, Lees WR. CT mapping of the distribution of saline during radiofrequency ablation with perfusion electrodes. Cardiovasc Intervent Radiol. 2005; 28:476–480.

[16] Demazumder D, Mirotznik MS, Schwartzman D. Biophysics of radiofrequency ablation using an irrigated electrode. J Interv Card Electrophysiol. 2001; 5:377–389.

[17] Qadri AM, Chia NJ, Ooi EH. Effects of saline volume on lesion formation during saline-infused radiofrequency ablation. Appl Math Model. 2017; 43:360–371.

[18] Antunes CL, Richard T, Nélia OA, et al. Saline-enhanced RF ablation on a cholangiocarcinoma: a numerical simulation. Int J Comput Math Electr Electron Eng. 2012; 31:1055–1066.

[19] Burdío F, Tobajas P, Quesada R, et al. Distant infusion of saline may enlarge coagulation volume during radiofrequency ablation of liver tissue using cool-tip electrodes without impairing predictability. Am J Roentgenol. 2011; 196:837–843.

[20] Ahmed M, Lobo SM, Weinstein J, et al. Improved coagulation with saline solution pretreatment during radiofrequency tumor ablation in a canine model. J Vasc Interv Radiol. 2002; 13:717–724.

[21] Iwata A, Mitamura Y, Niki M, et al. Binarization of enhanced depth imaging optical coherence tomographic images of an eye with Wyburn-Mason syndrome: a case report. BMC Ophthalmol. 2015; 15:2–6.

[22] Ishigami K, Yoshimitsu K, Nishihara Y, et al. Hepatocellular carcinoma with a pseudocapsule on gadolinium-enhanced MR images: correlation with histopathologic findings. Radiology. 2009; 250:435–443.

[23] Goldberg SN, Ahmed M, Gazelle GS, et al. Radio-frequency thermal ablation with NaCl solution injection: effect of electrical conductivity on tissue heating and coagulation-phantom and porcine liver study. Radiology. 2001; 219:157–165.

[24] Pennes H. Analysis of tissue and arterial blood temperatures in the resting human forearm. J Appl Physiol. 1948; 1:5–34.

[25] Abraham J, Sparrow E. A thermal-ablation bioheat model including liquid-to-vapor phase change, pressure- and necrosis-dependent perfusion, and moisture-dependent properties. Int J Heat Mass Transf. 2007; 50:2537–2544.

[26] Doss JD. Calculation of electric fields in conductive media. Med Phys. 1982; 9:566–573.

[27] Chang IA. Considerations for thermal injury analysis for RF ablation devices. Open Biomed Eng J. 2010; 4:3–12.

[28] Schutt DJ, Haemmerich D. Effects of variation in perfusion rates and of perfusion models in computational models of radio frequency tumor ablation. Med Phys. 2008; 35:3462–3470.

[29] Trujillo M, Romero R, Berjano E. Modelos teóricos basados en métodos numéricos de un aplicador cool-tip para ablación RF de tumores: relación entre la temperatura y la impedancia. IFMBE Proc. 2013; 33:17–20.

[30] Zorbas G, Samaras T. Simulation of radiofrequency ablation in real human anatomy. Int J Hyperthermia. 2014; 30:570–578.

[31] Zhang B, Moser MAJ, Zhang EM, et al. Numerical analysis of the relationship between the area of target tissue necrosis and the size of target tissue in liver tumors with pulsed radiofrequency ablation. Int J Hyperth. 2015; 31:715–725.

[32] Ahmed M, Liu Z, Humphries S, et al. Computer modeling of the combined effects of perfusion, electrical conductivity, and thermal conductivity on tissue heating patterns in radiofrequency tumor ablation. Int J Hyperth. 2008; 24:577–588.

[33] Syha R, Gatidis S, Grözinger G, et al. C-arm computed tomography and volume perfusion computed tomography (VPCT)-based assessment of blood volume changes in hepatocellular carcinoma in prediction of midterm tumor

response to transarterial chemo- embolization: a single center retrospective trial. Cancer Imaging. 2016; 16:1–8.

[34] Berjano E, Hornero F. Thermal-electrical modeling for epicardial atrial radiofrequency ablation. IEEE Trans Biomed Eng. 2004; 51:1348–1357.

[35] Tungjitkusolmun S, Haemmerich D, Cao H, et al. Modeling bipolar phase-shifted multielectrode catheter ablation. IEEE Trans Biomed Eng. 2002; 49:10–17.

[36] Berjano E, Burdío F, Navarro A, et al. Improved perfusion system for bipolar radiofrequency ablation of liver: preliminary findings from a computer modeling study. Physiol Meas. 2006; 27:55–66.

[37] Pätz T, Kröger T, Preusser T. Simulation of radiofrequency ablation including water evaporation. IFMBE Proc. 2009; 25:1287–1290.

[38] Kiricuta I, C, Simplaceanu V. Tissue water content and nuclear magnetic resonance in normal and tumor tissues. Cancer Res. 1975; 35:1164–1167.

[39] Schepps JL, Foster KR. The UHF and microwave dielectric proper- ties of normal and tumor tissues: variation in dielectric proper- ties with tissue water content. Phys Med Biol. 1980; 25:1149–1159.

[40] Kim BM, Jacques SL, Rastegar S, et al. Nonlinear finite-element analysis of the role of dynamic changes in blood perfusion and optical properties in laser coagulation of tissue. IEEE J Sel Top Quantum Electron. 1996; 2:922–933.

[41] Qin Z, Balasubramanian SK, Wolkers WF, et al. Correlated parameter fit of Arrhenius model for thermal denaturation of proteins and cells. Ann Biomed Eng. 2016; 42:612–625.

[42] Haemmerich H, Schutt DJ, Wright AW, et al. Electrical conductivity measurement of excised human metastatic liver tumors before and after thermal ablation. Physiol Meas. 2009; 30:459–466.

[43] Singh S, Repaka R. Temperature-controlled radiofrequency ablation of different tissues using two-compartment models. Int J Hyperth. 2017; 33:122–134.

[44] Hall SK, Ooi EH, Payne SJ. Cell death, perfusion and electrical parameters are critical in models of hepatic radiofrequency ablation. Int J Hyperthermia. 2015; 31:538–550.

[45] Aramburu J, Anto'n R, Rivas A, et al. Liver cancer arterial perfusion modelling and CFD boundary conditions methodology: a case study of the haemodynamics of a patient-specific hepatic artery in literature-based

healthy and tumor-bearing liver scenarios. Int J Numer Meth Biomed Eng. 2016; e02764:1–20.

[46] Sahani DV, Holalkere NS, Mueller PR, et al. Advanced hepatocellular carcinoma: CT perfusion of liver and tumor tissue-initial experience. Radiology. 2007; 243:736–743.

[47] Irastorza R, Trujillo M, Berjano E. How coagulation zone size is underestimated in computer modeling of RF ablation by ignoring the cooling phase just after RF power is switched off. Int J Numer Meth Biomed Eng. 2017; 33:e2869.

[48] Rossmann C, Garrett-Mayer E, Rattay F, et al. Dynamics of tissue shrinkage during ablative temperature exposures. Physiol Meas. 2014; 35:55–67.

[49] Brace CL, Diaz TA, Hinshaw JL, et al. Tissue contraction caused by radiofrequency and microwave ablation: a laboratory study in liver and lung. Tissue contraction caused by thermal ablation. J Vasc Interv Radiol. 2010; 21:1280–1286.

[50] Ooi EH, Ooi ET. Mass transport in biological tissues: comparisons between single- and dual-porosity models in the context of saline-infused radiofrequency ablation. Appl Math Modell. 2017; 41:271–284.

[51] Forster JC, Harriss-Philips W, Douglass MJJ, et al. A review of the development of tumor vasculature and its effects on the tumor microenvironment. Hypoxia. 2017; 5:21–32.

[52] Abraham JP, Sparrow EM, Ramadhyani S. Numerical simulation of a BPH thermal therapy – a case study involving TUMT. J Biomech Eng. 2007; 129:548.

Chapter 4

Development of a catheter-based technique for endoluminal radiofrequency sealing of pancreatic duct

4.1. Abstract

Endoluminal sealing of the pancreatic duct by glue or sutures facilitates the management of the pancreatic stump. Our objective was to develop a catheter-based alternative for endoluminal radiofrequency (RF) sealing of the pancreatic duct. We devised a novel RF ablation technique based on impedance-guided catheter pullback. First, bench tests were performed on *ex vivo* models to tune up the technique before the *in vivo* study, after which endoluminal RF sealing of a ~10 cm non-transected pancreatic duct was conducted on porcine models using a 3Fr catheter. After 30 days, sealing effectiveness was assessed by a permeability test and a histological analysis. The RF technique was feasible in all cases and delivered ~5 W of power on an initial impedance of 308 ± 60 Ω. Electrical impedance evolution was similar in all cases and provided guidance for modulating the pullback speed to avoid tissue sticking and achieve a continuous lesion. During the follow-up the animals rate of weight gain was significantly reduced ($p<0.05$). Apart from signs of exocrine atrophy, no other postoperative complications were found. At necropsy, the permeability test failed and the catheter could not be reintroduced endoluminally, confirming that sealing had been successful. The histological analysis revealed a homogeneous exocrine atrophy along the ablated segment in all the animals. Catheter-based RF ablation could be used effectively and safely for endoluminal sealing of the pancreatic duct. The findings suggest that a fully continuous lesion may not be required to obtain complete exocrine atrophy.

4.2. Introduction

Sealing of the pancreatic duct is used to manage two main pancreatic malignancies: pancreatitis and pancreatic ductal adenocarcinoma [1]. Sealing is usually achieved either by ligation of the affected pancreatic duct to eliminate pancreatic secretions or tumor resection followed by anastomosis of the remaining pancreatic stump [2,3]. However, the common problem of leakage of the pancreatic contents into the abdomen, also known as pancreatic fistula, can affect patient morbidity and mortality during the postoperative period. Many studies have explored feasible techniques for sealing the pancreatic stump in order to replace anastomosis and minimize the risk of leakage [4]. Sutures, staplers, clips or endoluminal glue injections are some of the most frequently used tools currently used in clinical practice. However, none of these techniques has been proven to effectively reduce the high risk of failure in these cases.

Radiofrequency ablation (RFA) is one of the recently explored sealing techniques. In this case the action mechanism does not rely on introducing a sealing agent, but on inducing epithelial necrosis to trigger fibrosis (cicatrization) and collagen shrinkage and cause ductal atrophy. Our research group had already examined the effect of pancreatic stump closure by RF-assisted transection in terms of fistula formation on rat and pig models [5–7]. The results showed that RFA not only induced exocrine atrophy for ductal occlusion but also reduced the occurrence of fistula. These findings encouraged us to go beyond the transection plane and consider extending RFA endoluminally along a segment of the pancreatic duct itself.

The concept of endoluminal thermal ablation is not really new since it has already been used in clinical applications for vascular occlusion such as e.g. hepatic tumor arteries, varicose veins [8,9] and biliary tumors [10]. However, to our knowledge, there is no evidence that this technique has been previously employed for pancreatic remnant sealing, as proposed here. As in the case of glue, the main purpose of thermal coagulation of the duct walls is to prevent leakage by sealing the secretory ducts along its walls and inducing ductal atrophy and also ensure the loss of ductal permeability. In order to efficiently

perform endoluminal ablation of the pancreas, a thermal coagulation zone should meet the following characteristics: 1) it should be long enough to suit the remnant pancreas after a resection; 2) be as contiguous as possible, i.e. with the minimum number and length of gaps; 3) there should be sufficient margin across the duct wall, i.e. ablate the entire epithelium and ensure loss of permeability, which requires a depth of 1–2 mm; and 4) it must be safe, i.e. no steam pops or tissue disruption, which means keeping tissue temperature below 80–90ºC and avoiding tissue sticking to the electrode.

Additional technical requirements for a device aimed at endoluminal surgery of the pancreatic duct should also include: 1) a suitable diameter to fit the duct along the entire route; 2) flexible enough to pass easily through the duct, which is not usually straight; and 3) be long enough to cover the entire target segment. The electrodes used to create the thermal lesion should be on the catheter itself. In this context our objective was thus to develop a new catheter-based technique for endoluminal RF sealing of the pancreatic duct and to assess its safety and performance on an *in vivo* porcine model.

4.3. Materials and methods

The first phase, based on an *ex vivo* model, was used to tune up the experimental setup, which consisted of an RF catheter combined with impedance-guided pullback. The aim was to determine the suitability of the catheter in terms of diameter, size, flexibility, and ablation protocol. The second phase was based on an *in vivo* porcine model and assessed the safety and feasibility of the novel technique with a 30-day follow-up. In both phases the electrodes were powered by a Radionics Cosman Coagulator CC-1 (Radionics, Burlington, MA, USA), a versatile generator previously used with endovascular RF catheters for arterial occlusion in liver cancer [8]. Impedance evolution was recorded during the ablations by a USB data acquisition module connected to the RF generator.

4.3.1. *Tissue samples for ex vivo and in vivo models*

The *in vivo* study was conducted on 8 Landrace-Large White pigs (27.3 kg mean weight), according to the protocol approved by Ethical Commission of the Universitat Autònoma de Barcelona (Authorization Number CEEAH 3487 and DMAH 9583) and the Government of Catalonia's Animal Care Committee. The *ex vivo* study was conducted on two types of sample: bovine liver acquired from a local slaughterhouse, and porcine pancreas obtained from 3 pigs, which underwent necropsy under the same authorized protocol as that used in the *in vivo* study.

4.3.2. *Considerations on the catheter design*

In general, successful endoluminal ablation should ensure: 1) catheter flexibility to operate inside the duct, 2) shallow thermal lesions circumscribed exclusively to the tissue around the pancreatic duct (sufficient to completely seal the secondary ducts draining into the main duct), and 3) the ability to estimate a suitable level of applied voltage from the initial impedance measurement. Potential catheter designs for endoluminal ablation should also take the following issues into account: number of electrodes (single or multiple), function mode (mono-, bi-, multi-polar), electrode type (dry or wet), and application procedure (point-to-point or continuous pullback).

The first tentative test was on a single long RF electrode based on a 3 Fr metallic guide whose length was tailored to the lesion length in order to create one long lesion by 'segmental' ablation. This first idea was discarded since the edge effect prevented the formation of a long uniform thermal lesion around one RF electrode. Regardless of the ablation time (10–20 s), the lesion surrounding the electrode was nonhomogeneous and much deeper at the edges, which was associated with overheating, audible steam pops (registered at 2–4 s) and tissue sticking. Also, the long metal wire was not sufficiently flexible to operate inside soft delicate tissue.

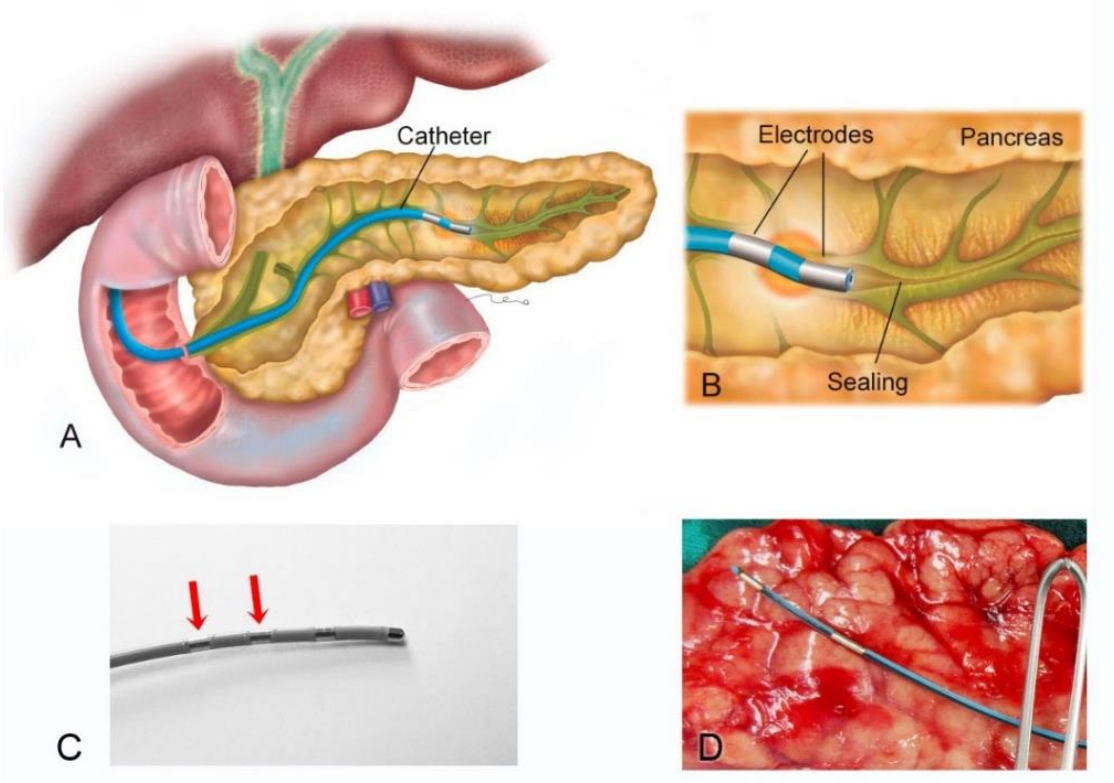

Figure 19. (a) Overview of the catheter-based technique for endoluminal radiofrequency sealing of pancreatic duct. The catheter is introduced into the pancreatic duct through the papilla. (b) Detail of catheter tip in which RF power is applied between two electrodes. The thermal lesion causes the duct to seal (the illustration is that of a human pancreas). (c) 5 Fr bipolar RF catheter used for *ex vivo* ablations on bovine liver (the most proximal electrodes were used for ablations). (d) 3 Fr bipolar RF catheter used for *ex vivo* and *in vivo* ablations on porcine pancreas.

Another consideration was that a single long RF electrode must be operated in monopolar mode, making it difficult to predict the thermal lesion geometry, since the exact power delivered to the target site depends on the unpredictable electrical characteristics of all the tissues involved in the electrical circuit.

The bipolar mode employs at least two closely spaced electrodes to create shallow thermal lesions confined to the inter-electrode space. The applied power depends almost exclusively on the characteristics of the tissue between the electrodes. Less power is required in bipolar mode to ablate the same lesion volume, which is appropriate in terms of safety, especially when working on small or fragile organs, such as the pancreas, which is surrounded

by other delicate organs.

A final issue to be considered is the possible internal cooling of the electrodes. Although cooled electrodes have an advantage over dry electrodes and avoid tissue sticking (e.g. CelonProSurge Applicator, Olympus, Germany), they are also known to create deeper thermal lesions than the dry type. As the goal in endoluminal ablation is to create relatively shallow thermal lesions around the pancreatic duct (1–2 mm depth) and avoid damage to the pancreatic parenchyma or adjacent organs, dry electrodes seem to be the better choice.

For all the procedures we employed commercially available flexible catheters, which include a pair of metal electrodes separated by plastic insulation. The catheter would be introduced into the pancreatic duct through the papilla and would create thermal lesions around the electrodes, as illustrated in Figure 19. The lesions could be created either point-to-point (i.e. positioning the catheter at one point and then repositioning it to a contiguous point after having created a lesion) or continuously by the pullback technique.

4.3.3. *Protocol for ex vivo experiments*

Three sets of *ex vivo* ablations were conducted, two on bovine liver and one on pancreatic tissue. Bovine liver was selected for its accessibility, homogeneity, and the ease of identifying the shape of the thermal lesions.

The first set of *ex vivo* ablations on liver was performed without pullback in order to tentatively establishing the relationship between the applied power, duration and created thermal lesion. This also allowed us to determine the approximate potential starting point for pullback, i.e. when the catheter pullback should start to avoid overheating and roll-off (abrupt rise in impedance). The applied voltage was 50 V and the ablation durations varied according to the roll-off time.

The second set of liver ablations was conducted with catheter pullback and provided information on the relation between pullback speed and lesion continuity. Both the first and second sets were conducted with the catheter between two fragments of liver (sandwich structure). The pullback sequence

was guided by the impedance progress as follows: catheter pullback only started when impedance reached a plateau (ensuring sufficient heating of the tissue in contact with the electrodes) and with early signs of an imminent cutout, i.e. when the impedance attempted to rise (implying overheating). In other words, the goal was to keep the impedance as steady as possible, since it is reasonable to assume that this implies that the same amount of power is being applied along the entire duct, hence ensuring the continuity of the thermal lesion without the need for overlapping. Pullback was carried out manually by the operator, who moved the catheter according to impedance progress as reflected in an audible signal provided by the RF generator. In this second set of *ex vivo* ablations the applied voltage was slightly lower (43 V instead of 50 V), since preliminary trials had shown that better pullback control could be obtained at this value. The liver ablations were conducted with a 5 Fr catheter as used in cardiac electrophysiology (see Fig. 19c). Their durations varied with the length of the liver fragment.

Once the impedance-guided procedure was seen to be feasible, a third set of ablations was conducted on porcine pancreas. Sample size in this set was small (n=3) due to a limited supply of *ex vivo* pancreatic specimens. Since it was not possible to introduce a 5 Fr catheter into the porcine duct, this set was finally conducted by a 3 Fr catheter (Minitrode, Bioampere Research, Conselve, Italy) with two 3 and 4 mm long 10 mm interspaced electrodes (Figure 19d). In this case the applied voltage was also 43 V, which implied a power of ~5 W.

4.3.4. *Protocol for in vivo experiments*

The ablation protocol established in the *ex vivo* trials was then tested on 8 Landrace-Large White pigs. This sample size was used in a previous study with a similar objective [7]. Prior to surgery, all the animals underwent a 12 hour-fast. All were premedicated with azaperone (4 mg/kg intramuscularly (IM)) (Stresnil ®, Ecuphar veterinaria, Spain), ketamine (10 mg/kg IM) (Ketamidor ®, Richter Pharma, Austria) and morphine (0.2 mg/kg IM) (Morfina B.Braun®, B.Braun Medical, Spain). Induction was performed with

propofol 2–4 mg kg^{-1} intravenously (IV) (Propofol lipuro®, B.Braun Vetcare, Spain. After induction, all the animals were intubated with an orotracheal tube, and anaesthesia was continued during the surgical procedure with isoflurane 2% (Isovet®, Piramal Critical Care Limited, UK) in 100% oxygen through a rebreathing circuit. Lactated Ringer's solution was infused at a rate of 10 mL/kg/h during the peri-operative period. Antibiotic therapy was administered with cephazoline 20 mg/kg IV (cefazolina normon®, Laboratorios Normon, Spain) via the cephalic vein. Heart rate, respiratory rate, pulse oximetry, electrocardiography, non-invasive blood pressure and capnography were monitored during anaesthesia using a multi-parameter monitor (VetCare®; B Braun Vetcare, Spain).

Thermal ablations were performed with the same 3 Fr catheter as used on the *ex vivo* pancreas introduced into the duct through the pancreatic papilla by means of laparotomy and enterotomy. Once the catheter was placed in the end duct (~10 cm insertion depth), RF power (37 V) was applied. As in the *ex vivo* experiments, the catheter was pulled back along the entire duct until one of the electrodes was no longer inside it (RF generator automatically shut down). To control the pullback speed, the operator continuously monitored impedance visually on a laptop and by following the audible signal emitted by the RF generator.

After this process, enterotomy and laparotomy were closed in the conventional manner. The animals were kept alive for a 30-day follow-up, after which all were again anesthetized, intubated and ventilated for laparotomy and dissection of the entire pancreas, which was then immediately placed in 10% buffered neutral formalin. The animals were then euthanized using a commercial euthanasia solution. The principal duct of the dissected pancreas was identified and cannulated and the following tests were conducted: a feasibility test, consisting of reintroducing the catheter into the pancreatic duct through the duodenal papilla, and a permeability loss test consisting of injecting saline into the ablated duct. The pancreas was divided into 3 mm–thick sections for further histological analysis and 2 or 3 5 μm samples from each section were stained with hematoxylin and eosin and then

evaluated by light microscopy. Pathologists unaware of the experimental design assigned the degree of exocrine pancreas atrophy from 0 to 5.

All the surgical procedures were performed by the same surgical team (AA and XM[1]). To analyze sealing effectiveness, alterations of the animals' weight increments at 30 days after surgery, feasibility of reintroducing the catheter into the pancreatic duct, and duct permeability were considered. The degree of atrophy was determined by histological analysis.

4.4. Results

4.4.1. *Ex vivo experiments*

In the first set of *ex vivo* ablations on bovine liver (without pullback) initial impedance was 606 ± 14 Ω, and the mean applied power was ~5 W (50 V applied voltage). In all the ablations we observed a similar impedance pattern, which went through the following consecutive phases: 1) gradual initial impedance drop toward a steady minimum value, 2) plateau phase with a fairly steady minimum value, and 3) abrupt impedance rise. The beginning of the plateau phase occurred at 12±3 s and coincided with the start of visible and audible signs of tissue overheating, such as steam pops, and also with a visible thermal lesion (tissue whitening). Impedance during the plateau was 384±20 Ω. The abrupt impedance rise occurred at 21±6 s and was preceded by audible pops 5 s before ablation ended.

The second set of *ex viv*o ablations employed the pullback technique and an attempt to keep a constant impedance value as long as possible, which meant keeping the plateau for as long as possible. The applied voltage was reduced to 43 V, since 50 V led to rapid tissue overheating, electrode sticking and a non-uniform lesion. As in the first set, the initial impedance and plateau impedance were 568±48 Ω and 334±37 Ω, respectively. In this case, due to the voltage reduction, applied power was ~5 W. In this second set we identified two main factors associated with pullback that affected lesion geometry and size: speed (slow vs. fast) and continuity (intermittent vs. uninterrupted –

[1] (AA) PhD Anna Andaluz, (XM) PhD Xavier Moll, Departament de Medicina i Cirurgia Animals, Facultat de Veterinària, Universitat Autònoma de Barcelona, Barcelona, Spain.

continuous–). A fast and continuous pullback caused an initial minor impedance drop and led to greater number of abrupt impedance rises, although without visible lesions. When pullback was slow, two different types of behavior were seen that depended on pullback continuity:

1) When pullback was slow and intermittent, impedance followed a sawtooth waveform with small abrupt rises (see black arrow in Fig 20a) each time the catheter was moved, so that the evolution matched well with the lesion pattern. The intermittency involved tissue charring and sticking just before the end of pullback, or at extremely low speed, while gaps appeared (absence of thermal lesion) with a fast pullback.

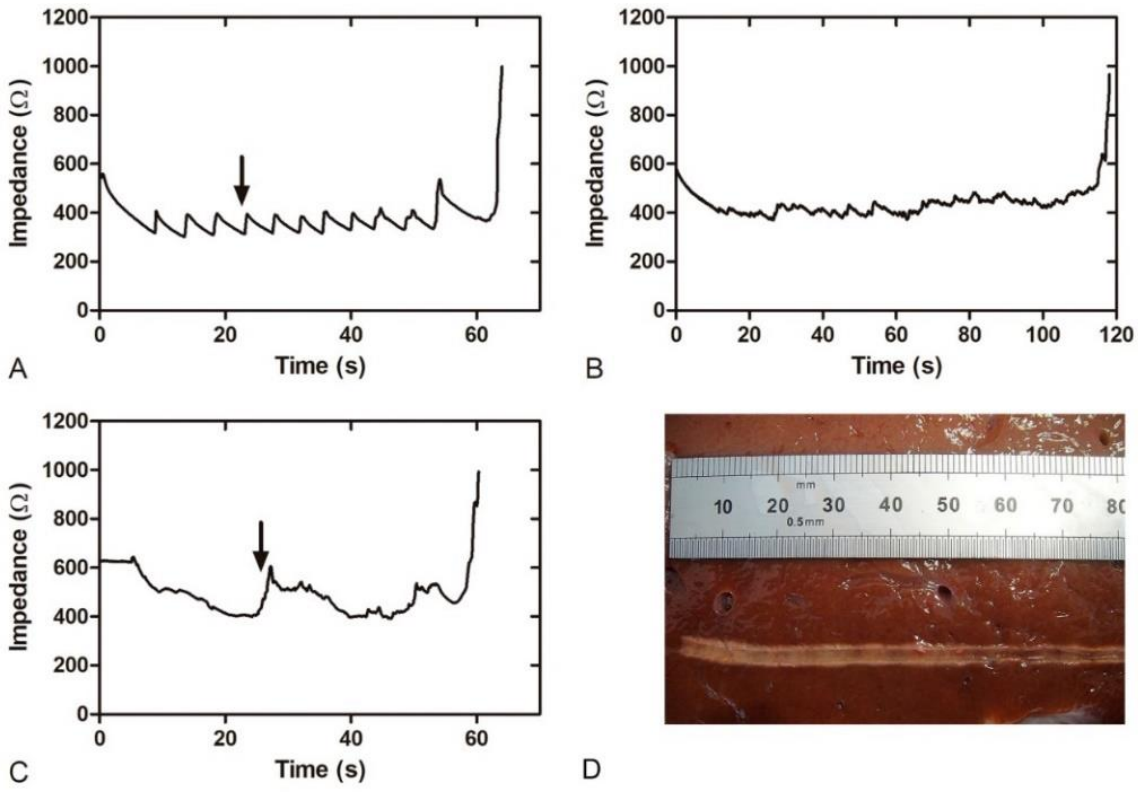

Figure 20. Results of the second set of *ex vivo* experiments. (a)-(c) Examples of impedance evolution. (a) Small-amplitude sawtooth associated with slow and intermittent catheter pullback. (b) and (c) Smooth patterns associated with slow and continuous catheter pullback. (d) Thermal lesion created on bovine liver by slow and continuous pullback (impedance shown in (b).

2) When pullback was slow and continuous, the impedance waveform smoothed out (see Fig. 20b) and avoided tissue sticking. The lesions thus produced were also uniform in depth, with a whitish zone extending continuously ~1 mm around the electrode along the entire ablation line (see Fig. 20d). In these cases the plateau was reached in ~23 s, after which pullback was applied at a mean speed of ~0.07 cm/s. When the speed became too slow, impedance gradually rose (black arrow in Fig. 20c), which was interpreted as an early sign of an imminent impedance jump (implying overheating) and therefore pullback was speeded up.

The third set of *ex vivo* ablations was conducted on pancreatic tissue with a 3 Fr instead of a 5 Fr catheter, since the pancreatic lumen was narrower than expected. The initial impedance was 523±29 Ω, a value slightly lower than that obtained by a 5 Fr catheter on bovine liver. The applied voltage was kept at the same level as in the previous set (~43 V). Impedance followed the three-phase pattern observed in the first two sets of *ex vivo* ablations. The time to reach plateau was more than 100 s, which was three times longer than in the two previous sets. The impedance value at the plateau was 302±40 Ω (see Fig. 21a). Abrupt impedance increases were associated with tissue sticking and carbonization points (see black arrow in Fig. 21b), just after which the catheter was relocated. Unfortunately, this movement caused visible gaps (see white arrow in Fig. 21b), since they were associated exactly with the zones where the electrodes did not apply power as the catheter was moved. As in the previous sets, we also observed that pulling back too fast impeded the creation of visible thermal lesions. Overall, the lesions created in this third set showed larger margins (2–3 mm) than the two previous sets on liver with a 5 Fr catheter. During the ablations, more abrupt impedance changes and more roll-offs occurred, which contributed to a more intermittent pullback and to irregular lesions in terms of depth and continuity (i.e. with gaps).

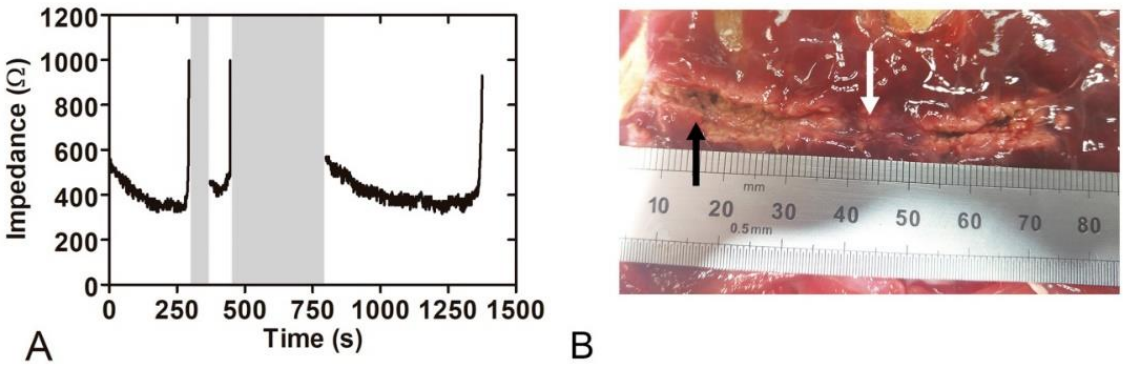

Figure 21. Results of the third set of *ex vivo* experiments. (a) Typical impedance during ablation. (b) Lesion created along the pancreatic duct in a pancreas treated with 43 V and pullback as continuous as possible. Gray bands show power cut off instants after abrupt impedance increases associated with tissue sticking and carbonization (black arrow in (b)). After this event pullback was always speeded up in order to relocate the catheter, which in turn led to some visible gaps (white arrow in (b)).

4.4.2. *In vivo experiments*

Since the tissue lesions of the *in vivo* group could not be seen until 30 days after the procedure, the evolution of the electrical variables was the only indicator for creating uniform and continuous thermal lesions. The mean initial impedance was 308±60 Ω, considerably lower than in the *ex vivo* specimens. The applied voltage was reduced to 37 V, which implied a power of ~5 W (comparable to the value measured in *ex vivo* ablations). A time of ~30 s was required to reach the impedance plateau (220±35 Ω), at which time pullback started. Impedance followed the same three-phase pattern as in the *ex vivo* ablations. However, the *in vivo* ablations showed a higher incidence of roll-offs, estimated as one every 40 s of ablation, and the impedance rises usually involved tissue sticking, which forced us to relocate the catheter rapidly in order to complete the ablation, which often required vigorous action. This meant the impedance evolution was more irregular than in the *ex vivo* experiments. Total ablation duration varied slightly in the trials in relation to specific duct length and roll-off occurrence. An average of 11 cm of pancreatic duct was ablated at a mean pullback speed of ~0.1 cm/s.

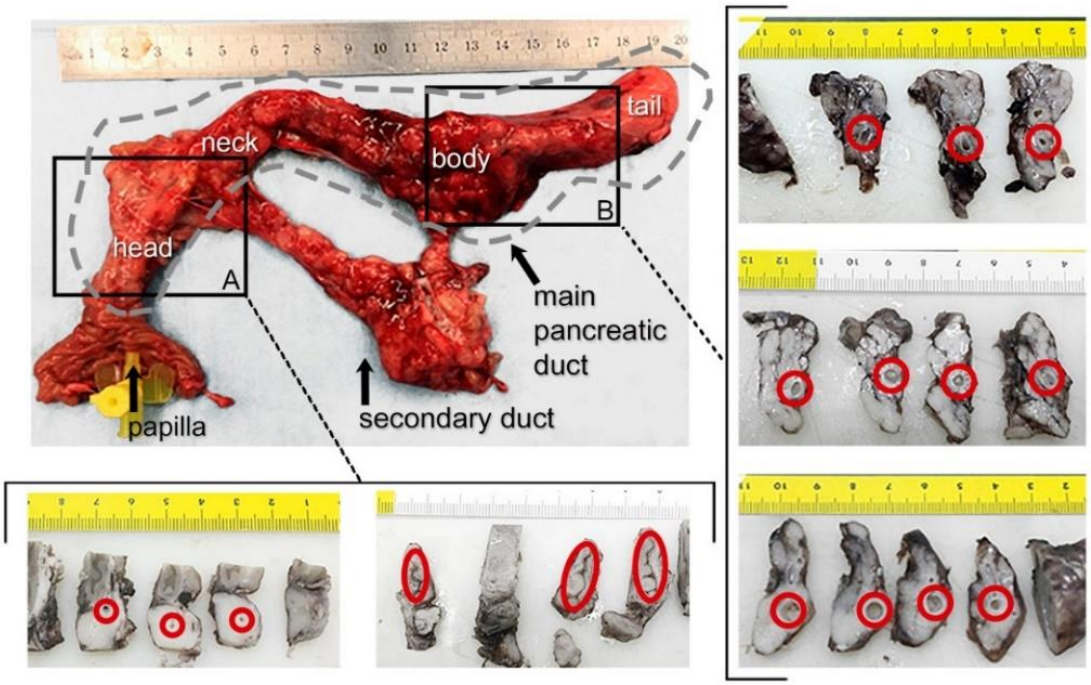

Figure 22. Results of the *in vivo* experiments. Macroscopic images of one of the treated pancreas and cross sections at the level of the head (a) and body (b). Red dotted circles indicate the position of the main duct. Lumen was not completely closed in all cases and ductal dilation was observed, particularly in the body (units in cm). Grey dashed line indicates the main duct position in pancreas.

During the 30-day follow-up the animals experienced alterations of stool consistency. After this period, their mean weight was 31 kg, which meant a slower than normal rate of weight gain (4 kg per 30 days). At necropsy, the feasibility test to verify the presence of ductal occlusion failed, since it was impossible to re-insert more than a few centimeters of the catheter into the duct, due to the lumen being too narrow. This also meant we could not perform the permeability test, as the liquid could not be injected as planned through the distal end of the duct. All this suggested that sealing was completely effective after 30 days at the level of the duodenal papilla. Beyond the papilla, a macroscopic view of cross-sections of pancreatic duct revealed different degrees of ductal dilation (diameter ranging widely from <1 mm to >10 mm), although at the level of the head the lumen seemed completely sealed in all cases (Section A in Fig. 22).

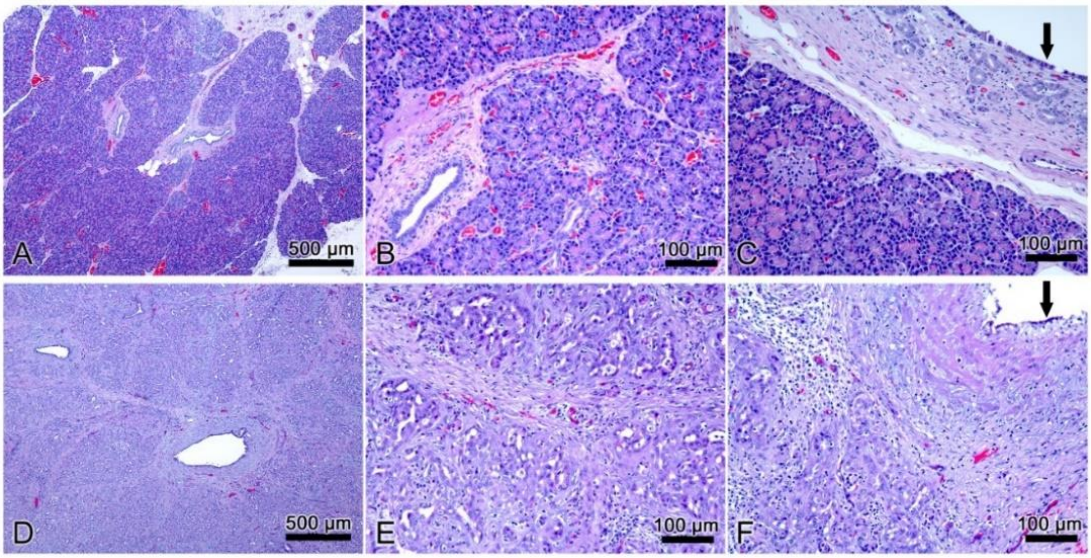

Figure 23. Results of *in vivo* experiment. Histological images of normal pancreas (a)-(c) and samples with sealing-induced pancreatic atrophy (d)-(f). Compared to normal pancreatic tissue, the treated samples show evident atrophy of the acinar component (purple dye) with only intralobular ducts remaining (d,e); the epithelium of the interlobular ducts is flattened or has been lost ((f), black arrow); marked interlobular fibrosis (d)-(f); scattered inflammatory infiltrate (e,f). H&E ×5 (a,d) and ×20 (b,c,e,f).

Figure 23 shows histological images of normal pancreatic tissue and pancreas after treatment. The histological study of the treated samples revealed complete acinar atrophy and that only the intralobular ducts remained after ductal ablation (Fig. 23d and 23e). The epithelium of the interlobular and some of the intralobular ducts showed a metaplasia from columnar or cuboidal to squamous and was lost in other areas (Fig. 23f). All the samples showed marked periductal and interlobular fibrosis (Fig. 23d-23f) and scattered inflammatory infiltrate (Fig. 23f).

4.5. Discussion

Sealing the pancreatic duct has always been challenging due to the risk of pancreatic juice leaking into the peritoneal cavity, which continues to be the main complication contributing to the high mortality rate [7]. The endoluminal RFA with pullback proposed here could potentially reduce this risk. Moreover, being a minimally invasive technique, it offers the advantages of a likely faster recovery and fewer side effects than injecting a sealing agent

or tissue suturing. To our knowledge, this is the first study to examine the feasibility of the catheter-based RF sealing technique for the pancreatic duct. As this was a development study, it had several phases to progressively fine-tune the proposed technique (catheter and ablation protocol) and finally obtain relevant information on its safety and performance on an *in vivo* porcine model.

4.5.1. *Initial steps fine-tuning technique*

The first phases conducted on liver *ex vivo* fragments showed how the different variables involved interact with each other during ablation with pullback. What we learned was that: 1) a few watts (~5 W) are enough to create 1–2 mm deep lesions; 2) pullback must begin when the impedance plateau is reached, which may coincide with audible pops; 3) it is possible to modulate the rate of pullback to keep the impedance as steady as possible, i.e. to try to maintain the plateau phase during the entire procedure; 4) this can be done by monitoring impedance and/or by an audible signal associated with impedance progress; and 5) if all these conditions are observed, the thermal lesion can be continuous (without gaps) along the entire path.

When we tried to transfer these conditions to the case of the pancreatic duct (pancreas *ex vivo* ablations), we learned that: 1) a narrower catheter diameter is required (3 Fr instead of 5 Fr); 2) catheter pullback through the pancreatic duct is less straightforward than the simple movement between two slices of liver tissue; 3) this means that the impedance-guided lesion is not so effective in the pancreas, with sticking, a need for overlap, and possible gaps; 4) sudden impedance rises are possibly related to tissue sticking and require moving the catheter, with the possibility of gaps; 5) gaps can be also produced by excessive pullback speed; and 6) when present, thermal lesions are 2–3 mm deep. This information was used to carry out a 30-day survival *in vivo* study.

4.5.2. *Clinical assessment of the technique*

On planning the *in vivo* study we expected thermal ablation inside the pancreatic main duct to produce the following phenomena: 1) occlusion of the small exocrine ducts branching from the main duct and subsequent acinar atrophy, causing the suppression of exocrine secretions; and 2) shrinkage of the collagen fibers around the main duct and subsequent reduction of its lumen, making it less permeable. Initially we thought that in order for these phenomena to occur efficiently, a continuous thermal lesion had to be created along a segment of the main duct. This was probably over-optimistic, since although thermal ablation produces immediate tissue shrinkage (due to protein denaturation and collagen contraction) this could only create a partial occlusion, as opposed to other mechanical methods (such as suture or stapler).

What the *in vivo* study revealed is that it is very difficult to create continuous lesions along the pancreatic duct, possibly due to the irregular anatomy of the main duct, but also due to the technical limitations of the impedance-guided protocol. In fact, gaps were observed in the *ex vivo* pancreas just after ablation. In the same way, the sudden impedance rises during *in vivo* ablations suggest the possible presence of gaps in the lesion and the possibility of the diameter not being reduced along the whole ablation length. This was later confirmed in the macroscopic analysis, where the main duct was not completely occluded in all zones. Complete duct occlusion at the pancreas head was also evident from the impossibility of reinserting the catheter through the duodenal papilla. We still do not have a convincing explanation of why the proximal duct (head zone) was more occluded than the distal duct. The images in Fig. 22 also show that the ablated duct was usually circular in shape, regardless of the dilation diameter or location, which suggests that the energy deposition occurred symmetrically around the electrodes and was limited in depth.

Interestingly, despite the existence of lesion gaps and presence of non-occluded segments, clinical observations during follow-up and histological findings were compatible with complete exocrine atrophy. The atrophic pancreas was deprived of acini to secrete digestive enzymes, which caused the

failure of the digestive functions. All the animals experienced digestive alterations and a notably reduced rate of weight gain after the 30-day follow-up.

In view of all the results, the complete occlusion of the entire main duct may not be required to generate complete exocrine atrophy. In fact, it is possible that the partially occluded duct segments also contributed to the exocrine atrophy. Since RF ablation also severs duct walls and produces thermal necrosis and apoptosis of the ablated zone, it is likely that atrophy and acinar cell loss are also a result of thermally-induced apoptosis. It is thus reasonable to assume that a fully continuous lesion along the main duct might not be necessary to achieve exocrine atrophy, which would be triggered not only by an immediate RF-induced effect, but also by biological processes within 30 days after ablation.

4.5.3. *Safety issues*

Regarding the safety issues involved in the ablative technique, we must keep in mind that bipolar RFA has already been clinically used for endoluminal ablation of vessels and biliary duct, so the concept of endoluminal ablation itself is well-known and assumed to be safe. The risks of using RFA instead of another mechanical method, such as staplers, sutures or clips, could include overheating of the target tissue and unintentional ablation of the neighboring tissue (e.g. intestine). In our study these risks were minimized by establishing a 'safe ablation environment' by trying to keep the pancreas as far as possible from other viscera during ablation by simple mechanical deviation. In addition, all the procedures were accomplished by personnel experienced in using RF-based devices. Finally, the absence of postoperative complications associated with RF power suggests that the proposed ablation method keeps risks at a reasonably low level.

4.5.4. *Technical feasibility*

The ablation control proposed in this study is entirely based on impedance progress. We discarded temperature monitoring due to it being technically

complex to include temperature sensors in such a small catheter. Moreover, while a temperature sensor would only provide information on the temperature in the tissue in contact with it (not necessarily the maximum tissue temperature), impedance gives a more complete picture of the characteristics of tissue affected by ablation through the direct relationship between electrical conductivity and temperature. In fact, this technique has been used previously in the management of biliary tumors and venous obstruction or other venous insufficiencies [10–13]. While we designed our own endoluminal RFA protocol, other studies used commercial devices designed for treating varicose veins (e.g. Celon ProCurve, Olympus, Germany). In both cases the method is based on impedance feedback for catheter guidance by visualizing impedance and power evolution and attending to audible signals. It also allows working in a specific impedance range that cuts out when exceeded. We had to adapt this technique to the present study, since endoluminal RFA had never been used before to seal the pancreatic duct. The delicate pancreatic tissue structure required a flexible applicator and the right catheter to fit a ~1 mm duct diameter, which ruled out the use of the commercial product of 5 Fr.

In addition, impedance monitoring has already been proposed to estimate the temperature and lesion size during RF ablation due to the inverse relationship of both parameters [14]. Tissue heating enhances ion mobility and current flow and thus produces a characteristic impedance drop in the early stages of ablation. Although thermal lesions in high-temperature ablative techniques require temperatures in the range 50–100ºC, it is also known that lesion evolution is closely connected to the temperature-time relationship, which depends on the amount of power applied. In particular, it is known that a few minutes of exposure at 50ºC triggers progressive tissue shrinkage and irreversible tissue damage [15], while only a few seconds at 60ºC produce tissue coagulative necrosis seen as a whitish area in the ablation zone [16,17]. Once thermal equilibrium has been reached, the impedance value stabilizes at the minimum and lesion size remains static. Further ablation leads to tissue overheating and vaporization at temperatures

between 100 and 105ºC and is characterized by audible steam pops, an abrupt impedance rise, tissue carbonization and sticking [17]. Once focused on impedance monitoring, our findings identified three different phases in its progress during ablation: 1) a drop associated with initial heating, 2) a plateau phase, and 3) occasional abrupt increases associated with overheating. All the phases could easily be distinguished in our *ex vivo* findings, in which whitish and carbonization zones appeared, suggesting that the tissue was in fact exposed to the 60–100ºC range. Overheating incidents also occurred in the *in vivo* study and suggest that the tissue was exposed to temperatures of up to 100ºC. The longer the plateau phase, the longer the ablation with sufficient power delivery and without carbonization. It has also been suggested that keeping the plateau impedance at a target value for a specific time should lead to the desired lesion depth [9]. The value of the plateau phase depends on tissue type and other conditions that affect its electrical properties, such as hydration or blood irrigation [18,19]. For instance, in our study the differences between the *ex vivo* and *in vivo* models were possibly related to additional heat loss by convective blood perfusion cooling (also known as heat sink effect), which is only present under *in vivo* conditions. Other factors could also have affected these differences, such as a smaller impedance drop and a higher threshold temperature for coagulative necrosis, finally producing smaller lesion depths in the *in vivo* case. Accordingly, we observed that *in vivo* samples had nearly half as low initial impedance values (308±60 Ω vs 523±29 Ω) and a smaller impedance drop (220±35 Ω vs 302±40 Ω at plateau) than *ex vivo* specimens. We were not able to assess the differences in lesion depth between *ex vivo* and *in vivo* cases since in the latter case the lesion dimensions were assessed after a 30-day follow-up period. However, our findings can be discussed in the light of previous liver studies (with a similar pancreas blood perfusion rate, 860±170 mL/min/kg vs. 767±357 mL/min/kg [20]). These studies showed that *in vivo* lesions have a 36–44% smaller diameter than *ex vivo* lesions [21-23], which suggests that the *in vivo* pancreatic lesions created in our study could be around 1 mm deep (since lesion depth was 2–3 mm in the *ex vivo* case and

similar power levels were used in both cases).

Additionally, different studies have reported that tissue shrinkage (which starts at 50ºC) produces up to 20–30% of tissue constriction of the initial margin and therefore the real ablation zone is actually greater than that measured [15,24,25], while a limited degree of tissue shrinkage could also reduce the chances of complete mechanical occlusion of the duct, although, as seen in our study, it was sufficient to reduce the duct diameter to less than the catheter diameter and ruled out catheter reintroduction.

Due to variations in the electrical properties of ex and *in vivo* tissue, a lower voltage value was used in the *in vivo* study (43 V vs. 38 V). This change also affected the pullback speed (~0.03 cm/s vs. 0.1 cm/s), but in all cases a power of ~5 W could be delivered, suggesting that the delivered power, as determined by applied voltage and pullback speed, is the vital parameter in achieving successful RFA. The power and pullback speed values used in our study were noticeably lower than those usually reported for venous ablation (18-25 W and 0.5-1 cm/s, respectively) [9,12,13,26,27]. Numerous studies have reported that the recommended clinical power and pullback speed values can increase the incidence of tissue carbonization and sticking [12]. An additional issue in obtaining permanent sealing is the need to reapply the treatment (overlapping) to provide sufficient energy for effective sealing [28]. Interestingly, Badham et al. [12] suggested that values of 6 W and 0.08 cm/s are the most optimal to obtain a successful vein lesion by single RF ablation and avoid tissue overheating and sticking. These values are very similar to these employed by us (5 W, 0.03-0.1 cm/s). It is important to note that while we aimed for a slow continuous pullback, Badham et al. used a discontinuous pullback, so that 0.08 cm/s was really an approximate value. This similarity could be owing to the electrical properties of both tissues. In the *in vivo* study we found that a large number of abrupt impedance increases and tissue sticking events were inevitable. This problem could pose a serious risk of soft tissue rupture during the treatment. The relationship between the applied power and pullback speed determines the required energy level and the rate at which it is delivered to the tissue, and thus the final thermal dose to cause

tissue damage. The optimization of these parameters is still pending.

The outcomes obtained from this technique are undoubtedly affected by the additional factor of the operator's skill in controlling catheter pullback [26]. As already mentioned, an excessively slow pullback implies greater power deposited in the target area together with carbonization and sticking, while an exceedingly fast pullback produces gaps or even no lesion at all. Although the manufacturers usually recommend the appropriate powers and speeds to obtain continuous lesions and avoid overheating, the inherent tissue heterogeneity impedes creating a uniform lesion along the entire path. The operator's skill thus plays a vital role in varying pullback speed according to the impedance variations encountered. The amount of delivered power and pullback speed will also vary according to the desired outcome and may differ from the manufacturer's recommendations [27,28]. For all these reasons it is important to first estimate the relationship between impedance, delivered power and the required thermal lesion before applying endoluminal RFA with pullback.

4.5.5. *Limitations of the study*

Although our final clinical objective is the management of the pancreatic stump, the *in vivo* study was conducted on a non-transected pancreatic duct. A transected pancreas model would be more complex and would entail a higher risk of pancreatic leakage. Further research on this matter should therefore be conducted involving endoluminal RF sealing of the transected pancreatic duct in order to confirm the feasibility of the technique on a more realistic model.

As regards the clinical implications, it is important to note that the porcine model used in this study is anatomically different to the human pancreas in certain respects, as it has a secondary duct branching out from the main pancreatic duct (see Fig. 1 from [7]). In our study this duct was not ablated and therefore maintained its enzymatic secretory function, which could have reduced the effectiveness of the proposed technique. For this very reason the technique could be even more effective in the human pancreas.

4.6. Conclusions

The impedance-guided endoluminal RFA technique designed to seal the pancreatic duct seems to be a promising, feasible and safe alternative for management of the pancreatic stump and reducing the risk of leakage. Although power and pullback speed still need to be optimized, the findings obtained suggest that a fully continuous RFA lesion along the entire duct may not in fact be required to achieve pancreatic atrophy.

References

[1] Schneider MU, Meister R, Domschke S, et al. Whipple's Procedure Plus Intraoperative Pancreatic Duct Occlusion for Severe Chronic Pancreatitis: Clinical, Exocrine, and Endocrine Consequences During a 3-Year Follow-Up. Pancreas. 1987; 2(6):715-726.

[2] Alfieri S, Quero G, Rosa F, et al. Indications and results of pancreatic stump duct occlusion after duodenopancreatectomy. Updates Surg. 2016; 68(3):287-293.

[3] Tran K, Van Eijck C, Di Carlo V, et al. Occlusion of the pancreatic duct versus pancreaticojejunostomy: a prospective randomized trial. Ann Surg. 2002; 236(4):422-8

[4] Schoellhammer HF, Fong Y, Gagandeep S. Techniques for prevention of pancreatic leak after pancreatectomy. Hepatobiliary Surg Nutr. 2014; 3(5):276-87.

[5] Quesada R, Burdío F, Iglesias M., et al. Radiofrequency Pancreatic Ablation and Section of the Main Pancreatic Duct Does Not Lead to Necrotizing Pancreatitis. Pancreas. 2014; 43:931-937.

[6] Quesada R, Andaluz A, Cáceres M, et al. Long-term evolution of acinar-to-ductal metaplasia and b-cell mass after radiofrequency-assisted transection of the pancreas in a controlled large animal model. Pancreatology. 2016; 16(1):38-43

[7] Burdío F, Dorcaratto D, Hernandez L, et al. Radiofrequency-induced heating

versus mechanical stapler for pancreatic stump closure: in vivo comparative study. Int. J. Hyperthermia. 2016; 32(3):272-80.

[8] Khorsandi SE, Kysela P, Valek V, et al. Initial data on a novel endovascular radiofrequency catheter when used for arterial occlusion in liver cancer. Eur Surg. 2009; 41:104-108.

[9] Reich-Schupke S, Mumme A, Stücker M. Histopathological findings in varicose veins following bipolar radiofrequency-induced thermotherapy-results of an ex vivo experiment. Phlebology. 2011; 26(2):69-74.

[10] Atar M, Kadayifci A, Daglilar E, et al. Ex vivo human bile duct radiofrequency ablation with a bipolar catheter. Surg Endosc. 2018; 32(6):2808-2813.

[11] Duben J, Hnatek L, Dudesek B, et al. Bipolar radiofrequency-induced thermotherapy of haemorrhoids: a new minimally invasive method for haemorrhoidal disease treatment. Early results of a pilot study. Wideochir Inne Tech Maloinwazyjne. 2013; 8(1):43-8.

[12] Badham GE, Dos Santos SJ, Whiteley MS. Radiofrequency-induced thermotherapy (RFiTT) in a porcine liver model and ex vivo great saphenous vein. Minim Invasive Ther Allied Technol. 2017; 26(4):200-206.

[13] Tesmann JP, Thierbach H, Dietrich A, et al. Radiofrequency induced thermotherapy (RFITT) of varicose veins compared to endovenous laser treatment (EVLT): a non-randomized prospective study concentrating on occlusion rates, side-effects and clinical outcome. Eur J Dermatol. 2011; 21(6): 945-51.

[14] Hartung WM, Burton ME, et al. Estimation of temperature during radiofrequency catheter ablation using impedance measurements. Pacing Clin Electrophysiol. 1995; 18(11):2017-21

[15] Rossmann C, Garrett-Maye E. Dynamics of tissue shrinkage during ablative temperature exposures. Physiol Meas. 2014; 35(1): 55–67

[16] Goldberg SN, Gazelle GS, Mueller PR. Thermal ablation therapy for focal malignancy: a unified approach to underlying principles, techniques, and diagnostic imaging guidance. AJR Am J Roentgenol. 2000; 174(2):323-31

[17] Thomsen S. Pathologic analysis of photothermal and photomechanical effects of laser-tissue interactions. Photochem Photobiol. 1991; 53(6):825-35.

[18] Haemmerich D, Ozkan OR, Tsai JZ, et al. Changes in electrical resistivity of swine liver after occlusion and postmortem. Med. Biol. Eng. Comput. 2002; 40, 29-33.

[19] Shahzad A, Khan S, Jones M, et al. Investigation of the effect of dehydration on tissue dielectric properties in ex vivo measurements. Biomed. Phys. Eng. Express. 2017; 3: 045001.

[20] Hasgall PA, Di Gennaro F, Baumgartner C, et al. 2016. IT'IS Database for thermal and electromagnetic parameters of biological tissues, Version 3.0, September 1st, 2015, www.itis.ethz.ch/database. (accessed May 19, 2019)

[21] Patterson EJ, Scudamore CH, Owen DA, et al. Radiofrequency ablation of porcine liver in vivo: effects of blood flow and treatment time on lesion size. Ann Surg. 1998; 227(4):559-65.

[22] Song KD, Lee MW, Park HJ, et al. Hepatic radiofrequency ablation: in vivo and ex vivo comparisons of 15-gauge (G) and 17-G internally cooled electrodes. Br J Radiol. 2015; 88(1050): 20140497.

[23] Goldberg SN, Hahn PF, Halpern EF, et al. Radio-frequency tissue ablation: effect of pharmacologic modulation of blood flow on coagulation diameter. Radiology. 1998; 209(3), 761–767.

[24] Brace CL, Diaz TA, Hinshaw JL, et al. Tissue contraction caused by radiofrequency and microwave ablation: A laboratory study in liver and lung: Tissue contraction caused by thermal ablation. J Vasc Interv Radiol. 2010. 21(8): 1280–1286.

[25] Yu MH, Kim YJ, Park HS, et al. Shrinkage of hepatocellular carcinoma after radiofrequency ablation following transcatheter arterial chemoembolization: Analysis of contributing factors. PLoS ONE. 2019. 14(2):e0210667.

[26] Braithwaite B, Hnatek L, Zierau U, et al. Radiofrequency-induced thermal therapy: results of a European multicentre study of resistive ablation of incompetent truncal varicose veins. Phlebology. 2013; 28:38-46.

[27] Badham GE, Dos Santos SJ, Lloyd LBA, et al. One-year results of the use of endovenous radiofrequency ablation utilising an optimized radiofrequency-induced thermotherapy protocol for the treatment of truncal superficial venous reflux. Phlebology. 2018; 33(5):298-302.

[28] Newman JE, Meecham L, Walker RJ, et al. Optimising Treatment Parameters for Radiofrequency Induced Thermal Therapy (RFiTT): A Comparison of the Manufacturer's Treatment Guidance with a Locally Developed Treatment Protocol. Eur J Vasc Endovasc Surg. 2014; 47(6):664-9.

Chapter 5
General discussion

The main goal of the PhD Thesis was to develop computer models and experimental studies to examine deeply the phenomena related with RF ablation as minimally invasive therapy. In particular, three separate studies have been conducted: pulsed RF for pain relief, RF ablation of hepatic tumor using a new cooled wet electrode, and endoluminal sealing of pancreatic duct by bipolar RF ablation.

Regarding the use of RF ablation for pain treatment, there has been an unceasing interest for understanding the mechanisms behind the positive results of pulsed RF. This is due to the lack of the ultimate explanation and empirical evidence that would support possible hypotheses that have been posed so far. In line with this statement, *Chapter 2* describes a computer study on PRF performance to evaluate the electrical and thermal effects of different pulse protocols and PRF implications in a possible nerve electroporation. The concepts discussed in our study covered two main assumptions of PRF technique, such as to avoid tissue thermal damage and to provide a sufficient "electrical dose" for an effective pain release. In terms of electric field dosage, it is known that higher dose increases the electrical effect. However, the number of currently used protocols suggests that these have not yet been standardized. Though, some protocols might be chosen preferentially over others. The results from a number of studies have also showed that the effectiveness of PRF varied in different pain location. Thus, optimization and standardization of location-specific PRF treatments should be the objective of future research studies.

The study in *Chapter 3* focused on examining tissue hydration technique for RF ablation by a novel ICW electrode with two expandable perfusion needles. The main contributions involved building a computer model with realistic spatial distribution of the infused saline, which was based on an *in vivo* study on pig model. Also, mathematical description of saline-infused and non-infused zones of tumor tissue was provided and the modeled results were compared with those of the clinical trial. Increased tissue hydration has been proven to improve ablation lesion size by many studies, which employed different approaches for tissue irrigation. One of them was a design used in this study of ICW electrode with expandable perfusion needles, which ensured distant from the electrode saline infusion. Nevertheless, the common issue regarding saline injection is associated with the risk of uncontrolled thermal damage. This is due to the unpredictability of the perfusate distribution in tissue, and the fact that the resulting distribution would define the ultimate ablation zone. The study has raised the respective issues by proposing an experimental-based geometry for realistic saline spatial distribution. This approach has also shown how the proximity to blood vessels, acting as preferential drainage paths, importantly affected the final result. The findings also suggested that the establishment of clinically oriented computer models is highly recommended to improve prediction and optimization of RFA treatments with ICW electrodes. Additionally, a comparative computer modeling study could be conducted, in which RFA with ICW electrode and microwave ablation would be analyzed based on a currently running clinical trial.

Finally, a new endoluminal sealing technique for management of the pancreatic stump has been proposed in *Chapter 4*. This study can be considered as the first step forward in offering a promising alternative to patients with a high risk of morbidity after being submitted to the currently available treatments. The study describes a process of protocol fine-tuning for the impedance-guided RF ablation with pullback. To employ the *ex vivo* and *in vivo* models has shown to efficiently ensure the safety of the ablative technique. Despite the encouraging preliminary results and the method

considered as feasible, the proposed experimental model was relatively simple, regarding to what the real clinical case would look like. Therefore, a further experimental study is currently being conducted on more complex scenarios with surgically resected pancreas. This ongoing work addresses the pancreatic leakage issue, which is one of the most important complications nowadays that carries a substantial risk of fatal outcome.

Different methodologies have been used to accomplish this PhD Thesis. Regarding phantom and *ex vivo* models, although more simple than *in vivo* studies or clinical trials, their use can provide a valuable insight when adapted to specific study requirements. The chosen model should be as simple and efficient as possible but not simplistic, which also means that in some cases *ex vivo* model might be preferable over studies on living research subjects. The example of it could be the fine-tuning study in *Chapter 4*. However as shown in *Chapters 3* and *4*, some studies necessarily require a complex living system that would feature physiological phenomena affecting treatment effectiveness. Furthermore, computer models make a large contribution to the optimizing of performance, time and cost of the therapeutic techniques. Consequently, also in the scope of this work computer models have been proved to be complementary and essential to provide an adequate research quality and validation.

Chapter 6
Conclusions

The studies developed in the context of this PhD Thesis have provided more insight into the electrical and thermal performance of RF-based minimally invasive therapies applied to pain management and surgical oncology. In particular, the findings indicated possible risks and proposals of enhancement for the analyzed therapies. New techniques for a more effective treatment of tumors have also been suggested, and showed favorable results. The following conclusions address the separate studies listed in the *Preface* chapter.

Different PRF protocols analyzed by computer modeling in the *Chapter 2* aimed at improving their electrical performance and ensuring safe tissue temperature. The study has proven that higher voltage and pulse frequency repetition but shorter pulse duration increased the electrical effect of PRF and reduced slightly the thermal impact on tissue. The study has suggested that the risk of thermal damage could be avoided when the temperature controller was used. Consequently, this computer modeling study has also considered that PRF might provide a sufficient electric field magnitude to cause electroporation. Finally, agar phantom experimental study was found suitable to validate computer model accuracy. These findings could be used to establish new and more efficient PRF protocols.

The study in the *Chapter 3* examined various saline spatial distributions in order to develop an enhanced tumor model for RFA with new ICW electrode, and based on a realistic trial-based geometry for the infused tissue. The findings showed that a realistic saline spatial distribution differed noticeably from ideal spherical geometry, which is typically proposed in

computer modeling studies. The effect of different saline spatial distribution was also observed on the duration of simulated ablation. However, the main impact on computer model accuracy has been the complexity of saline-infused tumor model, in which infused and non-infused zones of tumor were defined. Therefore, the study indicates importance of building clinically-oriented computer models in achieving better approach of numerical studies.

A new catheter-based technique for endoluminal sealing has been proposed in the study in *Chapter 4* as an alternative for management of the pancreatic stump. The findings showed the feasibility of using impedance as a guidance parameter for continuous RFA. On the other hand, they also suggested that an effective sealing could be obtained regardless of the lesion continuity along the duct. This technique could be a promising and safe method for reducing the risk of leakage and patient morbidity during intervention, and thus, it lays fundaments for future studies on more realistic and complex experimental models.

Contributions

Publications in peer-reviewed journals

- **E. Ewertowska**, B. Mercadal, V. Muñoz, A. Ivorra, E. Berjano. Effect of applied voltage duration and repetition frequency of RF pulses for pain relief on temperature spikes and electrical field. A computer modeling study. *Int J Hyperthermia*. 2018; 34(1):112-121. doi: 10.1080/02656736.2017.1323122

- **E. Ewertowska**, R. Quesada, A. Radosevic, A. Andaluz, X. Moll, F. García Arnas, E. Berjano, F. Burdío, M. Trujillo. A clinically-oriented computer model for radiofrequency ablation of hepatic tissue with internally cooled wet electrode. *Int J Hyperthermia*. 2019; 35(1):194-204. doi: 10.1080/02656736.2018.1489071

- **E. Ewertowska**, A. Andaluz, X. Moll, A. Aguilar, F. Garcia, D. Fondevila, R. Quesada, M. Trujillo, F. Burdío, E. Berjano. Development of a Catheter-Based Technique for Endoluminal Radiofrequency Sealing of Pancreatic Duct. *Int J Hyperthermia*. 2019; 36(1):677-686. doi: 10.1080/02656736.2019.1627585

Conference proceedings

- **E. Ewertowska**, A. Andaluz, X. Moll, A. Aguilar, F. Garcia, D. Fondevila, R. Quesada, M. Trujillo, F. Burdío, E. Berjano. Preliminary study on the catheter-based endoluminal radiofrequency sealing of pancreatic duct. *Annual Meeting and Postgraduate Course of the Cardiovascular and Interventional Radiological Society of Europe*. Barcelona (2019); Cardiovasc Intervent

Radiol. 2019; 42 (Suppl 3):65-549. doi: 10.1007/s00270-019-02282-x. **Communication and oral presentation**

- Andaluz A, **Ewertowska E**, Moll X, et al. Endoluminal ablation of the main pancreatic duct as an exocrine pancreatic atrophy-inducing procedure: a pioneer method for an old need. *36th Annual Society for Thermal Medicine Meeting*. St. Pete Beach (2019). **Oral presentation**

- **E. Ewertowska**, A. Andaluz, X. Moll, A. Aguilar, F. Garcia, D. Fondevila, R. Quesada, M. Trujillo, F. Burdío, E. Berjano. Development of a novel catheter-based technique for endoluminal radiofrequency sealing of pancreatic duct. *Lasers in Surgery and Medicine (American Society for Laser Medicine and Surgery Abstracts).* Denver (2019); 51(S30), p12. https://doi.org/10.1002/lsm.23059. **Communication and oral presentation**

- **E. Ewertowska**, R. Quesada-Diez, A. Radosevic, A. Andaluz, X. Moll, E. Berjano, F. Burdio, M. Trujillo. A clinically-oriented computer model for radiofrequency hepatic ablation with internally cooled wet electrode. *Proceedings from 32nd Annnual meeting of the European Society for Hyperthermic Oncology*. Berlin (2018); Strahlenther Onkol. 2018; 194: 471. https://doi.org/10.1007/s00066-018-1295-1. **Communication and oral presentation**

- **E. Ewertowska**, R. Quesada-Diez, A. Radosevic, A. Andaluz, X. Moll, E. Berjano, F. Burdio, M. Trujillo. A clinically-oriented computational modelling: A radiofrequency ablation of liver with internally cooled wet electrode. *35th Annual Meeting of the Society for Thermal Medicine*. Tucson (2018). **Oral presentation**

- **E. Ewertowska**, R. Quesada-Diez, A. Radosevic, A. Andaluz, X. Moll, E. Berjano, F. Burdio, M. Trujillo. Computational modeling of radiofrequency ablation with an internally cooled wet electrode. *Eskola H., Väisänen O., Viik J., Hyttinen J. (eds) EMBEC & NBC 2017. EMBEC 2017, NBC 2017. IFMBE*

Proceedings. Tampere (2017); vol 65. Springer, Singapore. ISBN:978-981-10-5121-0. **Communication and oral presentation**

- **E. Ewertowska**, B. Mercadal, V. Muñoz, A. Ivorra, E. Berjano. Electrothermal model of pulsed radiofrequency ablation for pain relief: computer study and in vitro validation. *34th Annual Society for Thermal Medicine, Systemic treatment with local therapy*. Cancun (2017). **Oral presentation**